8-2000

Trajectory optimization and performance sensitivity studies of NASA Langley's proposed small satellite launch system

Brett Randall Starr

To the Graduate Council:

I am submitting herewith a thesis written by Brett Randall Starr entitled "Trajectory optimization and performance sensitivity studies of NASA Langley's proposed small satellite launch system." I have examined the final electronic copy of this thesis for form and content and recommend that it be accepted in partial fulfillment of the requirements for the degree of Master of Science, with a major in Aerospace Engineering.

Remi Engels, Major Professor

We have read this thesis and recommend its acceptance:

Roy J. Schultz, U. Peter Solies

Accepted for the Council:
Carolyn R. Hodges

Vice Provost and Dean of the Graduate School

(Original signatures are on file with official student records.)

To the Graduate Council:

I am submitting herewith a thesis written by Brett Randall Starr entitled "Trajectory Optimization and Performance Sensitivity Studies of NASA Langley's Proposed Small Satellite Launch System." I have examined the final copy of this thesis for form and content and recommend that it be accepted in partial fulfillment of the requirements for the degree of Master of Science, with a major in Aerospace Engineering.

R. Engels

Remi Engels, Major Professor

We have read this thesis and recommend its acceptance:

Roy J. Schulz

U Peter Solies

Accepted for the Council:

Associate Vice Chancellor and Dean of The Graduate School

Trajectory Optimization and Performance Sensitivity Studies of NASA Langley's Proposed Small Satellite Launch System

A Thesis
Presented for the
Master of Science
Degree
The University of Tennessee, Knoxville

Brett Randall Starr
August 2000

ABSTRACT

Optimal ascent and booster glide back trajectories were determined for NASA Langley's proposed small satellite launcher, SSL-1, for a given polar mission, vehicle configuration, propulsion system, aerodynamic characteristics, structural characteristics and trajectory constraints The optimal ascent and glide back trajectories were determined for a launch from Vandenberg Air Force Base launch pad SLC-2W and booster glide back to Vandenberg Air Force Base runway 30 The SSL-1 ascent and glide back trajectories were simulated and optimized in POST, Program to Optimize Simulated Trajectories. Inertial pitch angles relative to an inertial launch frame were specified as independent variables in the ascent trajectory and optimized to yield maximum weight to orbit Aerodynamic angles were specified as independent variables in the booster glide back trajectory and optimized to yield maximum altitude at a heading alignment cylinder six nautical miles south of runway 30

The SSL-1 could not perform an ascent trajectory that satisfies the constraint of gliding the booster back to a heading alignment cylinder for runway 30 The optimal SSL-1 ascent trajectory results in 1022 lb of total weight and 384 lb of payload being

inserted into a 150 nautical mile polar orbit However, a booster glide back that achieves a desired altitude goal of 18800 ft at a heading alignment cylinder for runway 30 could not be performed from the separation point of the optimal ascent for the given aerodynamic and structural limits. The separation Mach number could not be reduced to a point where the booster could attain a desired glide back altitude using reductions in booster size alone since the booster size could not be reduced more than 3% and meet the dynamic pressure at separation constraint of 300 lb/ft^2 The glide back altitude goal can be obtained if the structural normal force limit is increased to 3g loads or the aerodynamic constraint on dynamic pressure at separation is increased to 400 lb/ft^2 The altitude goal will likely be obtained if a high angle of attack drag maneuver is performed between Mach numbers 3 2 and 1 2 The maximum allowable angle of attack for stable flight in this speed range and the corresponding lift/drag characteristics are needed to quantify the obtainable altitude To achieve the desired altitude goal, modifications in the aerodynamic and/or structural limitations are needed

Weight to orbit performance is influenced by the dynamic pressure at separation constraint but is not sensitive to it The weight to orbit ranges from 384 lb to 400 lb for dynamic pressure limits of 300 lb/ft2 to 500 lb/ft^2 The glide back altitude is sensitive to the dynamic pressure at separation constraint Glide back altitude at the HAC ranges from 11995 ft to 24600 ft for dynamic pressure limits of 300 lb/ft^2 to 500 lb/ft^2 Both ascent and glide back performance is insensitive to atmospheric winds Mean winds reduce payload by 2 lb and increase altitude at the heading alignment cylinder 515 ft   The SSL-1 weight to orbit performance is insensitive to movements in the vehicle's C G. Movements up to 7% of the reference length result in a 2 lb change in payload   The glide back is sensitive to structural normal force limits Increasing the limit from 2.5g to 5 0g increases altitude at the heading alignment cylinder from 11995 ft to 23410 ft.

Table of Contents

List of Tables

List of Figures

List of Symbols

α	angle of attack (degrees)
γ_r	flıght path angle relatıve to local ground (degrees)
Θ_i	gımbal dırectıonal cosınes
Φ	gımbal angle ın pıtch plane (degrees)
θ_I	ınertıal pıtch angle (degrees)
κ_{arc}	factor to account for varıatıon ın arc length traveled on heading alignment cylinder
κ_g	factor to account for varıatıon ın glıde slope whıle returning to headıng alıgnment cylınder
κ_{HAC}	factor to account for varıatıon in glıde slope whıle on headıng alıgnment cylınder
κ_R	factor to account for varıation in glıde range
μ	planet gravıtatıonal constant (ft^3/s^2)
v_I	ınertıal velocıty (ft/s)
v_r	relatıve velocıty (ft/s)
ρ	atmospherıc densıty ($slug/ft^3$)

σ	aerodynamic bank angle (degrees)
a	semi major axis of orbit (ft)
A_{exit}	exit area (ft^2)
C_A	aerodynamic axial force coefficient
$C_{a\alpha}$	change in aerodynamic axial force coefficient with respect to angle of attack
$C_{A\delta S}$	change in aerodynamic axial force coefficient due to control surface deflection
C_{A0}	aerodynamic axial force coefficient at zero angle of attack
$C_{A\ base}$	aerodynamic axial force coefficient due to base drag
C_D	aerodynamic coefficient of drag
C_L	aerodynamic coefficient of lift
$C_{L\alpha}$	change in aerodynamic lift coefficient with respect to angle of attack
C_m	aerodynamic pitch moment coefficient
$C_{m\alpha}$	change in aerodynamic pitch moment coefficient with respect to angle of attack
$C_{m\delta S}$	change in aerodynamic pitch moment coefficient due to control surface deflection
C_{m0}	aerodynamic pitch moment coefficient at zero degrees angle of attack
C_n	aerodynamic yaw moment coefficient

C_N aerodynamic normal force coefficient

$C_{n\alpha}$ change in aerodynamic yaw moment coefficient with respect to angle of attack

$C_{N\alpha}$ change in aerodynamic normal force coefficient with respect to angle of attack

$C_{n\delta S}$ change in aerodynamic yaw moment coefficient due to control surface deflection

$C_{N\delta S}$ change in aerodynamic normal force coefficient due to control surface deflection

C_{n0} aerodynamic yaw moment coefficient at zero angle of attack

C_{N0} aerodynamic normal force coefficient at zero angle of attack

C_Y aerodynamic side force coefficient

$C_{Y\alpha}$ change in aerodynamic side force coefficient with respect to angle of attack

$C_{Y\delta S}$ change in aerodynamic side force coefficient due to control surface deflection

C_{Y0} aerodynamic side force coefficient at zero angle of attack

$\mathbb{C}^m$ m dimensional subspace of $\Re^n$

F_{AB} aerodynamic force in body coordinate system (lb)

G gravity potential function

$g(x)$	gradient vector
$G(x)$	Hessian vector
g_I	gravity in inertial coordinate system (ft/s^2)
J	gravitational harmonic coefficient
h	altitude (ft)
m	mass (slug)
M_{AB}	aerodynamic moment in body coordinate system (lb-ft)
m_{jett}	jettison mass (slug)
m_o	initial mass (slug)
q	dynamic pressure (lb/ft^2)
$\Re^n$	n dimensional vector space
r_e	equatorial radius (ft)
r_I	position vector in inertial coordinate system (ft)
r_p	polar radius (ft)
T_B	thrust in body coordinate system (lb)
Z_{ij}	basis vectors of $\mathbb{C}^m$ subspace

List of Abbreviations

AB	aerodynamic coordinate system to body coordinate system transformation matrix
alpha	angle of attack (degrees)
APAS	Aerodynamic Preliminary Analysis Software
azwr	the runway heading azimuth
azvelr	azimuth of relative velocity vector (degrees)
bankang	aerodynamic bank angle (degrees)
C G	center of gravity
dens	atmospheric density (slug/ft^3)
DoD	Department of Defense
dynp	dynamic pressure (lb/ft^2)
EOM	equation of motion
fazb	aerodynamic normal force (lb)
GA	ground coordinate system to aerodynamic coordinate system transformation matrix
gammar	flight path angle relative to the local ground (degrees)
gdalt	geodetic altitude (ft)
gdlat	geodetic latitude (ft)
GLOW	gross lift off weight (lb)

HAC	heading alignment cylinder
IB	inertial coordinate system to body coordinate system transformation matrix
IG	inertial coordinate system to ground coordinate system transformation matrix
IL	inertial coordinate system to launch coordinate system transformation matrix
ISS	International Space Station
LB	launch coordinate system to body coordinate system transformation matrix
LEO	low Earth orbit
LOX/RP	liquid oxygen/refined petroleum
MECO	main engine cutoff
NASA	National Aeronautics and Space Administration
NEP	nominal entry point
POST	Program to Optimize Simulated Trajectories
SLC-2W	launch pad at Vandenberg Air Force Base
SSL-1	Small Satellite Launcher
WTO	weight to orbit

INTRODUCTION

Background

U S commercial launch systems currently have an average cost of approximately $10,000 for each pound of payload inserted into low Earth orbit (LEO). These launch systems are becoming less cost competitive with more recently developed foreign launch systems As a result, U.S launch vehicle manufacturers are losing market share of commercial space launches In response to the high cost of accessing space, NASA Administrator Dan Golden initiated a research and development program for low cost launch systems The initiative included identification of a launch system capable of inserting small payloads ranging from 200 lb to 500 lb into LEO for approximately $1 0 million per launch Such a system could provide the lowest cost for a launch dedicated to small science, Department of Defense (DoD) and commercial payloads

NASA Langley's Vehicle Analysis Branch has proposed a low cost small launch system to be considered in the initiative and is conducting design studies to predict the ability of the small launch system to meet mission criteria for the $1 million launch cost goal The launch system, designated SSL-1, is composed of a reusable glide back booster coupled with two expendable upper stages The booster utilizes a winged body concept that allows the booster to return to its launch site after separation and be reused in subsequent launches Booster reusability is a major factor in reducing launch cost Other cost reduction approaches include utilization of commercially available upper stages, use of commercially available pressure fed propulsion systems and return of the booster to its launch site using a glide back maneuver rather than using cruise back propulsion Use of commercially available stages and propulsion systems significantly reduces vehicle development cost Development is focused on the booster and its integration with the upper stages Pressure fed propulsion systems reduce vehicle cost since their purchase cost and operational cost are significantly lower than the more complex pump fed systems Glide back booster return eliminates the cost of a cruise back propulsion system and the performance penalty due to its weight It also reduces the cost of thermal structures since booster separation must occur near Mach 3 before too much down range distance is attained With a maximum speed around Mach 3, the booster can use heat sink type thermal structures as opposed to more costly thermal structures The proposed SSL-1 vehicle is shown in figures I 1 through I.3 Note that all figures are included in appendix B and all tables are located in appendix A

Langley's Vehicle Analysis Branch design studies of the SSL-1 require trajectory analyses to size the vehicle and identify vehicle configuration changes or design changes that further improve its objective function, in this case minimum cost for placing the payload into LEO A flow chart of the iterative method for developing a conceptual design is shown in Figure 4 In this method, the vehicle geometry and propulsion system are chosen and the vehicle sized to meet mission requirements using estimates of the vehicle's propulsion, structural, aerodynamic and aeroheating characteristics. Component weights, vehicle dry weight and gross lift-off weight are determined for the estimated size Trajectory analysis begins with the estimated weight and vehicle characteristics to determine the extent to which mission criteria are met Trajectory results are used to determine vehicle scaling needed to meet mission criteria The vehicle is scaled using NASA's weights and sizing program CONSIZ [1] Trajectory analysis is repeated until a converged configuration is obtained Refer to reference 13 for a detailed description of the process

The vehicle design and configuration are improved during this iterative process by conducting performance sensitivity studies Performance sensitivity studies help identify design modifications and configuration changes that significantly impact weight to orbit performance The cost of configuration changes or design modifications that improve weight to orbit performance can then be used in trade studies to determine the cost effectiveness of such changes For example, determining a vehicle's performance sensitivity to the location of its center of gravity can indicate if a configuration change (such as mating position of the upper stages relative to the booster) is needed Determining a vehicle's performance sensitivity to a normal force constraint can indicate if design changes in wing structure are needed Once an optimal design and configuration are determined, development and operational cost are estimated using NASA's cost models

Thesis Problem Statement

Determine an ascent trajectory for the proposed small satellite launcher, SSL-1, that maximizes weight to orbit given its mission requirements, vehicle configuration, propulsion system, aerodynamic characteristics and trajectory constraints In addition, determine the SSL-1 performance sensitivity to variations in vehicle configuration and trajectory constraints

Approach

For a given mission and SSL-1 vehicle characteristics, an optimal trajectory will be determined using NASA's Program to Optimize Simulated Trajectories (POST) Several basic trajectory approaches to achieving the desired orbit will be used in developing initial guesses of flight control parameters The flight control parameters will be identified as independent variables in POST and optimized to achieve maximum weight to orbit. Note that POST must start its optimization process from an initial guess that results in an orbit reasonably close to the desired orbit The trajectory that results in the largest weight to orbit will be taken as optimal No guarantee of global optimality can be made Once an optimal trajectory is determined, performance sensitivity to vehicle configuration changes and constraint variations will be determined POST will also be used to conduct performance sensitivity studies. Constraint values and configurations will be varied incrementally over a selected range and a trajectory run for each value to determine the corresponding change in weight to orbit. The results from the studies will be documented and can be used in trade studies to determine if cost reductions are possible. An outline of the approach is given below

1 Architecture

   a. Reference missions

   b SSL-1 architecture

   c Propulsion, structural and aerodynamic characteristics

   d Vehicle weights and sizing

2. Theory

   a Optimal ascent

   b Three D.O F equation of motion

   c Propulsive force representation

   d Aerodynamic force representation

   e Thrust force representation

   f Vehicle mass

   g Gravity representation

h. Optimization technique

3. Post Models

a. Modeling approach

b. Ascent model and constraints

c. Glide back model and constraints

4. Trajectory Analyses

a. Ascent approaches

b. Optimal ascent trajectory

c. Ascent performance sensitivities

i. Trimming effects

ii. C G location sensitivity

iii. Constraint sensitivities

iv. Launch angle sensitivity

v. Atmospheric wind Sensitivity

vi. Separation point sensitivity

d. Glide back approaches

e. Optimal glide back trajectory

f. Glide back performance sensitivities

i. Separation point sensitivities

ii. Glide back constraint sensitivities

iii. Ascent constraint sensitivities

iv Atmospheric wind sensitivity

5 Conclusions and Recommendations

CHAPTER 1

ARCHITECTURE

1.1 Missions

The small satellite launcher architecture is being sized to fulfill two primary missions The first mission is to place a 330 lb payload into a circular polar orbit at an altitude of 150 nautical miles while returning its reusable booster to the launch site [1]. Polar missions will be launched from Vandenberg Air Force Base launch pad SLC-2W with the booster gliding back to Vandenberg's 30 runway The second mission is a rapid resupply mission to the International Space Station (ISS) [1] The resupply mission will place 800 lb of cargo into a circular orbit at an altitude of 220 nautical mile and inclination of 51.6° and return the reusable booster to its launch site Resupply missions will be launched from Wallops Island launch pad 0B with the reusable booster gliding back to Wallops Island runway 28

1.2 Small Satellite Launcher Architecture

The small satellite launcher architecture consists of two vehicle configurations, SSL-1 and SSL-2 The SSL-1 is configured to perform the polar mission while the SSL-2 is configured to perform an International Space Station servicing mission [1]. The SSL-

1 configuration consists of a three stage sequential burn configuration and is sized to meet polar mission requirements. The SSL-2 configuration adds two strap-on expendable boosters to the SSL-1 configuration to increase performance levels to that required for International Space Station servicing missions

The SSL-1 stages consist of a reusable glide back booster and two expendable upper stages Figures I 1 through I 3 show the booster, upper stages and booster combined with upper stages. The booster accelerates the upper stages to approximately Mach 3.2 at which point its main engines cut off and it separates from the upper stages After separation, the booster glides back to the designated runway for turnaround processing and reuse Its second and third stages are expendable upper stages All three stages utilize non-throttling pressure fed LOX/RP propulsion systems based on Microcosm's Bantam class launcher design [2] The SSL-1 configuration has a total dry weight of 26039 Lb, gross lift-off weight (GLOW) of 107134 Lb and overall length of 61 ft The booster has a wingspan of 32 ft The SSL-1 weights and dimensions are summarized in table 1 1

The SSL-2 configuration combines two expendable strap-on boosters with the SSL-1 elements making it a five stage system The strap-on boosters are identical to the SSL-1 second stage and are attached to the SSL-1 second stage The strap on boosters thrust in parallel with the glide back booster from lift-off In this configuration the glide back booster's main engine cut off (MECO) and separation occurs at Mach 2.8 The strap-on boosters continue to thrust up to Mach 9 0 at which point they separate and are expended on reentry. The SSL-2 configuration has a dry weight of 33,470 Lb and GLOW of 150,760 Lb The configuration's overall length and wingspan are the same as the SSL-1.

1.3 SSL-1 Vehicle Characteristics

The elements of the small launcher architecture are based on existing vehicles, with the exception of its reusable glide back booster, to minimize development cost The booster is being developed for the polar mission using existing hardware as much as possible to minimize cost. The propulsion, structural and aerodynamic characteristics of the initial SSL-1 configuration are described in the following sections. The launch system is in the conceptual design phase, thus only basic characteristics required for initial design studies are available. The characteristics will become more fully defined as the design matures.

1.3.1 Propulsion

All three SSL-1 stages utilize pressure fed propulsion systems based on a Microcosm design developed for their Sprite launch vehicle [2] All propulsion systems utilize liquid oxygen and refined petroleum (LOX/RP) fuel and are non throttling The reusable booster propulsion system is designed with four engines sized at 45 0 klb thrust each Each engine has a standard bell nozzle with an exit area of 3 33 ft^2, steady state mass flow rate of 163 6 slug/s and vacuum specific impulse (I_{sp}) of 275 seconds. The booster engines are mounted at their midpoint to minimize nozzle travel during gimbal used to cancel pitching moments resulting from center of gravity offset and aerodynamic loads The second stage is designed with two engines sized at 22 4 klb thrust This engine has a standard bell nozzle with an exit area of 6 78 ft^2, mass flow rate of 73 9 slug/s and vacuum I_{sp} of 303 seconds. The third and final stage is designed with one engine sized at 5.5 kLb thrust The engine has a standard bell nozzle with an exit area of 1 7 ft^2, mass flow rate of 18 4 slug/s and vacuum I_{sp} of 300 Propulsive characteristics are summarized in table 1 1

1.3.2 Structural Materials

The SSL-1 vehicle structures are a combination of aluminum and composite materials. The reusable booster structures are primarily aluminum while the second and third stage structures are primarily composite The booster's aluminum body acts as a heat sink and provides thermal protection during the high heating phases of its trajectory The materials used for the major structural components' of the booster and upper stages are summarized below

1.3.2.1 Booster

• wings	aluminum with titanium leading edges
• vertical tail	aluminum with titanium leading edge

• canard.	titanium
• body shell	aluminum with titanium nose
• propellant tanks	aluminum
• inter tank structure	aluminum
• engine thrust structure.	aluminum

1.3.2.2 Second Stage

• body shell.	aluminum
• propellant tanks:	graphite-epoxy with aluminum liner
• inter tank	graphite-epoxy
• engine thrust structure	VMI-graphite
• payload adapter	graphite-epoxy

1.3.2.3 Third Stage

• body shell	aluminum
• propellant tanks.	graphite-epoxy with aluminum liner
• inter tank	graphite-epoxy
• engine thrust structure	VMI-graphite
• payload adapter	graphite-epoxy
• payload fairing	graphite-epoxy

1.3.3 Aerodynamics

The SSL-1 reusable winged booster dominates the vehicle aerodynamic characteristics with the exception of pitch moment characteristics above Mach 1. The booster has a delta wing and canard configuration The wings are located to provide stable flight characteristics for its burnout center of gravity position of 68 percent of the reference length. The delta wings have a span of 32.0 ft, exposed surface area of 246 7 ft^2, aspect ratio of 2 59, root chord length of 16 3 ft and taper ratio of .175 Canards provide additional pitch control needed to trim the booster throughout its supersonic and transonic flight regime. The canards are mounted along the booster centerline and have an area of 30 1 ft^2

The SSL-1 aerodynamics of the booster and upper stages were determined using linear aerodynamic relationships The booster and upper stages aerodynamic characteristics were determined separately using APAS, aerodynamic preliminary analysis software [3]. The aerodynamic lift, drag and pitch moment of the booster combined with upper stages was taken as a linear superposition of the booster and upper stages aerodynamic lift, drag and pitch moment Due to the linearity of the aerodynamic relationships breaking down at high angles of attack (α), the aerodynamic data was limited to angles of attack between -18° and +18° up to Mach 3 0 and between -45° and +45° from Mach 3 0 to Mach 6 0 Aerodynamic characteristics beyond these angles of attack will have to be obtained from wind tunnel testing or nonlinear computational fluid dynamics methods

Aerodynamic data was generated for the four vehicle arrangements occurring during the polar mission These arrangements are

1) booster with upper stages attached to belly
2) second and third stages combined head to tail
3) booster alone
4) third stage alone

The aerodynamic data for the booster coupled to the upper stages and for the combined second and third stages consists of coefficient of lift, C_L , coefficient of drag, C_D , and pitch moment coefficient, C_m ,as a function of angle of attack and flight Mach number along with the change in base drag due to engine thrust as a function of flight Mach number. The effect of booster control surface deflections on the combined arrangement's lift, drag and pitch moment were not generated since engine gimbal was used during ascent to cancel aerodynamic moments and thrust moments resulting from center of gravity offset. The aerodynamic data for the booster alone consists of C_L , C_D and C_m as a function of angle of attack and Mach along with the change in C_L , C_D and C_m due to deflections of its control surfaces as a function of degrees deflection, angle of attack and Mach. The aerodynamic data for the third stage alone consists of C_L , C_D and C_m only The aerodynamic characteristics of the booster and the booster combined with upper stages are summarized in the following sections The aerodynamic characteristics of the combined second and third stages and third stage alone are omitted since they were found to have little impact on weight to orbit performance.

1.3.3.1 Lift Characteristics

The lift coefficients of the booster with upper stages and the booster alone are nearly the same for Mach numbers 0 2 to 2.0 APAS estimated both arrangements to have a small negative lift coefficient at 0° angle of attack and both arrangement's lift coefficients are linear functions of angle of attack over a ±18° range. Coupling the upper stages to the booster belly has the effect of increasing the lift coefficients by approximately 3% Above Mach 3 0, the addition of the upper stages increase lift coefficients by approximately 25% over the ±45° range. Figures 1.1 and 1 2 show the lift coefficients for the booster with upper stages and booster alone as a function of angle of attack for Mach numbers 0 2 to 2 0 and 3 0 to 6 0 Figure 1 3 depicts both arrangements change in lift coefficient with respect to angle of attack, $C_{L\alpha}$ Transonic effects begin to increase both arrangements' lift coefficients at Mach .8 with the maximum transonic effect occurring at Mach 0 9 The transonic effects are evident in figures 1 4 and 1 5 that show C_L as a function of Mach number for angles of attack ranging from 0° to 18° each arrangement The increase in C_L due to transonic effects is more pronounced for higher angles of attack The increased effect is highlighted in figures 1 6 and 1 7 that show C_L as a function of Mach for α=10°

from Mach 0 2 to Mach 6 0

1.3.3.2 Drag Characteristics

The drag coefficient vs angle of attack curves for both the booster and the booster combined with the upper stages indicate a parabolic drag characteristic with respect to angle of attack for both the booster and the booster combined with the upper stages Their drag characteristics are similar to the parabolic drag relationship

$C_D = C_{D\,p} + k\ C_L^2$ for an elliptical lift distribution where k is the parabolic constant and $C_{D\,p}$ is the parasitic drag coefficient The addition of the upper stages increases $C_{D\,p}$ approximately 22% while k remains approximately the same. For both arrangements $C_{D\,p}$ varies with Mach number, with the minimum occurring at Mach 0 2 and the maximum occurring at Mach 1 2. The parabolic constant does not vary significantly with Mach number for either arrangement. The parabolic nature of their drag coefficients is illustrated in Figures 1 8 and 1 9 that show the drag coefficient as a function of angle of attack for Mach numbers 0 2 to 6 0 Due to the drag coefficients' parabolic characteristics there is relatively little change in C_D for $-3° \le \alpha \le +3°$. Beyond 3°, C_D increases quickly with angle of attack Transonic effects begin to increase the drag coefficients at Mach 0 8 and reach a maximum at Mach 1 2 The transonic effects can be seen in figures 1 10 through 1 13 that show the drag coefficient as a function of Mach The dramatic increase in drag coefficient through the transonic regime is particularly evident in figures 1 12 and 1 13 that show the drag coefficient for a constant 10° angle of attack up to Mach 6 0

1.3.3.3 Pitch Moment Characteristics

The booster alone and booster with upper stages attached have similar pitch moment characteristics up to Mach 2.0 Up to Mach 2 0, both arrangements' pitch moments are approximately linear functions of angle of attack with negative slopes Beyond Mach 2 0 their characteristics change significantly and become dissimilar Both arrangements' pitch moment become positive for positive angles of attack due to the large positive pitching moment generated by the upper stages Their characteristics are dissimilar in that the booster pitch moment changes to a nonlinear function of angle of attack while the booster with upper stages pitch moment remains an approximately linear function of angle of attack. The booster with upper stages and booster alone pitch moment coefficients are shown as a function of α for Mach numbers 0 2 to 2 0 and 3 0 to 6 0 in figures 1 14 and 1 15 respectively The slope of the pitch moments with respect to angle of attack, $C_{m\alpha}$, is shown for each arrangement in figure 1 16 for Mach numbers up to 2 0 Coupling the upper stages to the booster decreases the magnitude of its $C_{m\alpha}$ by 25% to 45% The upper stages pitch moment is sufficiently positive for positive angles of attack that the negative pitch moment due to its drag is overcome and the pitch moment increased Both arrangements' pitch moment coefficients exhibit large increases in magnitude through the transonic regime The transonic increase in pitch moment is evident in figures

1 17 and 1 18 that show pitch moment coefficient as a function of Mach for a constant angle of attack

1.3.3.4 Aerodynamic Performance Characteristics

Figures 1 19 through 1 21 show the maximum lift, drag and pitch moment coefficients for the booster alone and booster with upper stages for Mach numbers 0.2 to 2 0 and 3.0 to 6 0 The powered flight maximum lift to drag ratio at each Mach number is shown for the booster with upper stages in figure 1 23 . The maximum powered lift to drag ratio occurred at $\alpha=8^\circ$ up to Mach 1 0 and at $\alpha=10^\circ$ for Mach numbers above 1. The powered lift to drag ratio decreases with increasing Mach number with subsonic ratios being approximately twice that of the supersonic values The untrimmed gliding lift to drag ratio for the booster alone is shown in figure 1 23 The untrimmed maximum lift to drag ratio for steady state glide is 6 77 occurring at $\alpha=6\ 5^\circ$. The aerodynamic pitch moment generated under glide conditions can be canceled with an elevon deflection of $+2\ 5^\circ$. Trimming reduces the maximum lift to drag ratio 11% to 6 00

1.4 Vehicle Weights and Sizing

The initial sizing of the booster was made based on estimations for a size required to meet the polar orbit mission requirement A weights and sizing model, CONSIZ [12], developed by NASA was used to estimated component weights, vehicle dry weight and gross lift-off weight (GLOW) corresponding to the estimated booster size The second and third stages are fixed in this study since they are based on Microcosm's design [2] The booster scales geometrically based on its reference length As the length is increased, the body diameter, wing area, etc. increase proportionally

CHAPTER 2

THEORY

2.1 Optimal Ascent

The goal of a launch vehicle's ascent is to obtain the flight conditions and inclination of a specified orbit at its point of insertion into the orbit. The orbital flight conditions to be met are altitude, velocity and flight path angle in a plane inclined from the equatorial plane by the specified inclination. Typically an orbital inclination and altitude are specified and the insertion point taken to be at the orbit's perigee where the flight path angle is zero. The velocity required to maintain the orbit is then easily calculated from equation 2.1 [4].

$$\upsilon_I = \sqrt{\mu\left(\frac{2}{r_p} - \frac{1}{a}\right)} \tag{2.1}$$

where μ is the planet's gravitation constant, r_p is the orbit's radius at periapsis and a is the orbit's semi-major axis.

For a vertical launch from a fixed launch pad at sea level the launch vehicle starts at an altitude of zero and flight path angle of 90°. The vehicle must accelerate to the calculated velocity and transition its flight path to zero degrees within a plane at the desired inclination as it climbs to the specified altitude. There are an infinite number of ascent trajectories that could be flown to achieve the flight conditions at orbit insertion However, most trajectories would require a vehicle unrealistic in size and cost The prudent approach to achieving the flight conditions is to define a trajectory that maximizes or minimizes a chosen objective function [5] The objective function is minimized or maximized by identifying an optimal set of trajectory parameters that influence the objective function. Typical trajectory parameters include but are not limited to launch azimuth, vehicle steering commands and points of stage separation This research obtained a flight trajectory that maximized the objective function of weight to orbit (WTO) for the SSL-1 within given trajectory constraints and orbital definitions

2.2 Equation of Motion

The launch vehicle's equation of motion defines its trajectory and is used as the basis for determining the influence of chosen parameters on a desired objective function such as weight to orbit An optimal set of flight parameters is determined as the set that minimize or maximize the objective function. For purposes of initial design studies, the equation of motion is based on a three degrees of freedom representation of the launch vehicle The launch vehicle was simplified to a point mass at its center of gravity with translational degrees of freedom. The vehicle's rotational degrees of freedom and associated polar inertia characteristics were ignored

The SSL-1 acceleration results from the forces acting on the vehicle. These forces consist of the aerodynamic forces, thrust forces and gravity forces. The aerodynamic and thrust forces act in the vehicle body coordinate system while the gravity force acts in the Earth centered inertial coordinate system The acceleration must be determined in the inertial coordinate system to maintain the validity of Newton's second law Thus, the thrust and aerodynamic forces must be transformed into the inertial coordinate system

During ascent, the body coordinate system is defined relative to an inertial launch coordinate system using Euler angles. The inertial launch coordinate system is located at the launch pad and is defined relative to the Earth centered inertial coordinate system by the pad latitude, longitude and azimuth angle that locates the body Z axis relative to North as the vehicle sits on the pad The launch coordinate system becomes inertial at liftoff Figure 2 1 shows the launch and body coordinate systems relative to the Earth centered system and their transformation matrices The transformation matrix that transforms body forces into the Earth centered system is the inverse of the combined launch system to body system and Earth centered system to launch system transformations This transformation relationship is given in equation 2 2

2 2 $$BI_{ij} = IB_{ji} = IL_{ji}\ LB_{ji}$$

where BI is the body coordinate system to inertial coordinate system transformation matrix, IL is the inertial coordinate system to launch coordinate system transformation matrix and LB is the launch coordinate system to body coordinate system transformation matrix

After separation from the upper stages, the booster body coordinate system is described relative to an atmospheric coordinate system using aerodynamic angles of bank, sideslip and angle of attack. This is done to simplify the description of steering commands used to define the booster glide back trajectory The aerodynamic coordinate system is defined relative to a local geographic coordinate system. These coordinate systems and their transformation matrices are also shown in figure 2.3 The transformation between the booster body coordinate system and Earth centered system is the inverse of the combined Earth to geographic, geographic to aerodynamic and aerodynamic to body coordinate transformations as shown in equation 2 3.

2 3 $$BI_{ij} = IB_{ji} = IG_{ji} GA_{ji} AB_{ji}$$

Where BI is the body coordinate system to inertial coordinate system transformation matrix, IG is the inertial coordinate system to local ground coordinate system transformation matrix, GA is the local ground coordinate system to aerodynamic coordinate system transformation matrix and AB is the aerodynamic coordinate system to body coordinate system transformation matrix The body to inertial transformation matrix allows the equation of motion to be written in terms of the instantaneous aerodynamic and thrust forces acting at the vehicle center of gravity Using Einstien's summation convention, the equation of motion is given by equation 2 4 below

2.4 $$r_{I_{i},t} = \frac{1}{m|_t} BI_{ij} \left[F_{AB_j} + T_{B_j} \right] + g_{I_i}$$

where $r_{I_{i},t}$ is the vehicle acceleration, F_{AB_j} represents the aerodynamic forces in the body system, T_{B_j} represents the thrust forces in the body system, g_{I_i} represents the gravity forces in the Earth centered system and $m|_t$ represents the vehicle mass at time t. The equation of motion is integrated numerically using the fourth order Runge Kutta process to determine v_{I_i}, r_{I_i} and m.

2.3 Aerodynamic Forces

The aerodynamic forces and moments acting on the vehicle are dependent on the atmospheric density, the vehicle's speed relative to the atmosphere, its orientation relative to the atmospheric velocity, its surface area and its aerodynamic characteristics The vehicle aerodynamic characteristics are represented with coefficients of normal force (C_N), axial force (C_A), side force (C_Y), pitch moment (C_m), and yaw moment (C_n) Using these coefficients, the aerodynamic forces and moments are expressed as.

2 5

$$F_{AB_x} = C_A\ q\ S$$
$$F_{AB_y} = C_Y\ q\ S$$
$$F_{AB_z} = C_N\ q\ S$$

$$M_{AB_y} = C_m\ q\ S\ L$$
$$M_{AB_z} = C_n\ q\ S\ L$$

where F_{AB}, M_{AB} are aerodynamic forces and moments in the body coordinate system respectively, $q = 1/2\,\rho v_{rel}^2$, S is the reference surface area used in calculating the force coefficients and L is the reference length used in calculating the moment coefficient. The above coefficients represent the characteristics of the complete vehicle configuration They are the sum of coefficients that represent zero lift conditions, the coefficient's change with respect to angle of attack, and incremental changes in the coefficient due to control surface deflections [6]. The sum of axial force coefficients also includes a coefficient representative of the vehicle's base drag Each coefficient's sum is given in equation 2 6

2.6

$$C_A = C_{A\,0} + C_{A\,\alpha} + C_{A\,base} + \sum C_{A\,\delta\,S_i}$$
$$C_Y = C_{Y\,0} + C_{Y\,\alpha} + \sum C_{Y\,\delta\,S_i}$$
$$C_N = C_{N\,0} + C_{N\,\alpha} + \sum C_{N\,\delta\,S_i}$$
$$C_m = C_{m\,0} + C_{m\,\alpha} + \sum C_{m\,\delta\,S_i}$$
$$C_n = C_{n\,0} + C_{n\,\alpha} + \sum C_{n\,\delta\,S_i}$$

Where C_{A0}, C_{Y0}, C_{N0}, C_{m0}, C_{n0} are coefficients of axial force, side force, normal force, pitch moment and yaw moment at zero angle of attack,

$C_{A\,\alpha}$, $C_{Y\,\alpha}$, $C_{N\,\alpha}$, $C_{m\,\alpha}$, $C_{n\,\alpha}$ are coefficients of change in axial force, side force, normal force, pitch moment and yaw moment with respect to angle of attack and

$\sum C_{A\delta S_i}$, $\sum C_{Y\delta S_i}$, $\sum C_{N\delta S_i}$, $\sum C_{m\delta S_i}$, $\sum C_{n\delta S_i}$ are the sum of changes in coefficients of axial force, side force, normal force, pitch moment and yaw moment due to all control surface deflections The vehicle aerodynamic moments cannot be directly incorporated into the three degrees of freedom equation of motion. In the three translational degrees of freedom representation, moments are statically balanced throughout the trajectory eliminating rotational degrees of freedom. During ascent the moments are balanced using engine gimbal. During glide back the moments are balanced using control surface deflections.

In engine gimbal, aerodynamic moments about the vehicle center of gravity are balanced by offsetting the engine thrust vector from the center of gravity as shown in figure 2 4 The moment balance in pitch and yaw are shown in equations 2 7 and 2.8 [6]

2.7 $$q\ S(C_m L + C_N \Delta xref - C_A \Delta zref) = e_{opq} r_{jp} T_{jq}$$

Where $j = 1$ to n, n = number of engines, $o = 2$ (pitch axes), $p = q = 1$ to 3 and e_{opq} is the permutation symbol

2 8 $$q\ S(C_n L + C_N \Delta xref - C_A \Delta yref) = e_{opq} r_{jp} T_{jq}$$

Where $j = 1$ to n, n = number of engines, $o = 3$ (yaw axes), $p = q = 1$ to 3 and e_{opq} is the permutation symbol

In control surface trimming, the aerodynamic moments created by the booster wing and body are canceled with elevon and canard deflections The elevon and canard deflections produce opposing moments that drive the overall vehicle C_m *and* C_n to zero. The moments generated by control surface deflections are nonlinear functions of Mach number and angle of attack Due to this nonlinearity, no equation is solved explicitly for the deflection required to cancel the wing and body moments Rather, an iterative root finding approach is used to search tables that contain the relationship between the moment coefficients, Mach number, angle of attack and control surface deflection and find control surface deflections that give over all vehicle moment coefficients of zero for the given Mach number and angle of attack

Trimming with control surfaces affects the axial and normal forces acting on the vehicle The axial drag component is increased while the normal lift component is reduced These effects are accounted for in the trimming calculation using incremental axial and normal coefficients The aerodynamic tables contain the incremental change in axial and normal coefficients due to deflections of each control surface over the vehicle's range of Mach number and angle of attack The incremental C_A *and* C_N values are added to the nominal C_A *and* C_N values to give trimmed C_A *and* C_N values

2.4 Thrust Forces

The SSL1 thrust forces are generated by rocket engines only The booster is designed to glide back without the aid of air breathing engines Each engine's vacuum thrust and nozzle exit area is specified as constant or input as a table that contains its relationship with time or other parameter The vacuum thrust is corrected for atmospheric pressure throughout the trajectory using the engine's exit area and atmospheric pressure as a function of altitude The thrust magnitude of the jth engine is then given by equation 2 9

2.9 $$T_j = T_{j\ vac} - A_{exit_j} P(alt)$$

The engine thrust forces can be misaligned from the body x coordinate due to engine gimbal used to trim the vehicle. Each engine's thrust vector is transformed into the body coordinate system using its gimbal directional cosines so that the total thrust vector in body coordinates is given by equation 2 10

2 10 $$T_{B_i} = \Theta_{ij} T_j$$

where the jth column of Θ contains the jth engine gimbal directional cosines

2.5 Vehicle Mass

The change in vehicle mass is equal to the propellant flow rate from each engine and any jettisoned masses Each engine's mass flow rate is defined as a constant or input as a table expressing the mass relationship to time or some other parameter The mass flow rate is then given by equation 2 11

2.11 $$\dot{m} = \sum_{j=1}^{n} \dot{m}_j$$

Discontinuities in vehicle mass occur when mass is jettisoned. Mass is jettisoned at booster separation, stage burnout or other user defined events such as aerodynamic fairing jettison when dynamic pressure falls to a specified level The mass of the vehicle at time t is then given by equation 2 12

2 12 $$m = m_o - \int_0^t \dot{m}\, dt - \sum_{i=1}^{n} m_{jet\,i}]_{t \geq t_{jett\,i}}$$

2.6 Planet Gravity

The inertial gravity vector g_I is based on an oblate spheroid planet The planet's equatorial radius, r_e, polar radius, r_p, gravitational constant, μ and seven gravitational harmonic coefficients, $J_2 - J_8$ are used to define a gravity potential function G The potential function at any radial distance r from the planet's center is given in equation 2 13 [6]

2 13

$$G = \frac{\mu}{r}\,\Pi$$

$$\begin{aligned}
\textit{where}\quad \Pi = 1 &- \frac{J_2}{2}\left(\frac{r_e}{r}\right)^2\left(3\left(\frac{z^2}{r^2}\right) - 1\right) \\
&- \frac{J_3}{2}\left(\frac{r_e}{r}\right)^3\left(5\left(\frac{z^3}{r^3}\right) - 3\left(\frac{z}{r}\right)\right) \\
&- \frac{J_4}{8}\left(\frac{r_e}{r}\right)^4\left(35\left(\frac{z^4}{r^4}\right) - 30\left(\frac{z^2}{r^2}\right) + 3\right) \\
&- \frac{J_5}{8}\left(\frac{r_e}{r}\right)^5\left(63\left(\frac{z^5}{r^5}\right) - 70\left(\frac{z^3}{r^3}\right) + 15\left(\frac{z}{r}\right)\right) \\
&- \frac{J_6}{16}\left(\frac{r_e}{r}\right)^6\left(231\left(\frac{z^6}{r^6}\right) - 315\left(\frac{z^4}{r^4}\right) + 105\left(\frac{z^2}{r^2}\right) - 5\right) \\
&- \frac{J_7}{16}\left(\frac{r_e}{r}\right)^7\left(429\left(\frac{z^7}{r^7}\right) - 693\left(\frac{z^5}{r^5}\right) + 315\left(\frac{z^3}{r^3}\right) - 35\left(\frac{z}{r}\right)\right) \\
&- \frac{J_8}{128}\left(\frac{r_e}{r}\right)^8\left(6435\left(\frac{z^8}{r^8}\right) - 12012\left(\frac{z^6}{r^6}\right) + 6930\left(\frac{z^4}{r^4}\right) + 1269\left(\frac{z^2}{r^2}\right) + 35\right)
\end{aligned}$$

The inertial gravitational vector is given by equation 2 14

2 14

$$g_{I_x} = \frac{\partial G}{\partial x}\ ,\quad g_{I_y} = \frac{\partial G}{\partial y}\ ,\quad g_{I_z} = \frac{\partial G}{\partial z}\ ,$$

2.7 Optimization

The overall goal of the SSL-1 development program is to minimize the cost of placing a 330 Lb payload into a 150 nmi polar orbit There are many factors that influence the cost of placing the payload into orbit with an optimal trajectory being one Other major factors include vehicle development cost and operational cost Development and operational cost increase as vehicle size increases Cost relationships such as these are not readily incorporated into POST for direct evaluation. Instead, they are used to identify technologies such as propulsion and structural materials to be used in a baseline vehicle configuration The trajectory for a given baseline vehicle is then optimized for maximum weight to orbit subject to specified constraints Refer to section 3 2 1 for a summary of SSL-1 ascent constraints The trajectory optimization objective function is defined as maximum weight to orbit For a fixed payload, maximizing weight to orbit minimizes vehicle size since the vehicle is scaled down as weight to orbit performance increases in order to maintain a fixed payload value

In the optimization, weight to orbit is defined as a 'cost' function with the goal of maximizing 'cost' within given constraints The cost function is not an explicit function of the independent variables used to shape the trajectory. Rather, it is an explicit function of the trajectory state variables r_I, v_I and m The state variables are explicit functions of the independent variables. The cost function is related to the independent variables through integration of the equation of motion

The equation of motion is integrated as being piecewise continuous since events such as booster separation, mass jettison or impulsive velocity maneuvers produce discontinuities in the state variables These events divide the trajectory into segments The equation of motion is initialized at the beginning of each segment using the state variables at the end of the previous event plus the instantaneous change in state variables defined to occur at the event as shown in equation 2.15

2.15 $$(x_i)_n^+ = (x_i)_n^- + (\Delta x_i)_n$$

Where $(x_i)_n^+$ represents the state variable vector after the nth event, $(x_i)_n^-$ represents the state variable vector before the nth event and $\Delta(x_i)_n$ represents the instantaneous change in state variables at the nth event. The relationship between the state variables and independent variables over the continuous segment from the nth event to the n+1 event is given by equation 2.16

2.16 $$(x_i)_{n+1}^- = EOM\left[(x_i)_n^+, (u_i)_n^+\right]$$

Where EOM represents the equation of motion and $(u_i)_n^+$ represents the set of independent variables.

The optimization process utilizes the equation of motion to identify the set of independent variables that produce state variables for maximum weight to orbit while meeting defined constraints. Maximization of a cost function such as weight to orbit is equivalent to minimization of an alternate cost function that is defined as the negative of the original cost function [7]

For a continuously smooth, twice differentiable multi-variable function it can be shown that a minimum occurs where the norm of the function's gradient is zero and its Hessian is positive definite [7]. The presence of constraints alters these conditions somewhat Constraints eliminate degrees of freedom Each linearly independent constraint eliminates one degree of freedom from the original n-dimensional vector space $\Re^n$. The constraints define a subspace of the original n-dimensional vector space as shown in equation 2 17

2.17 $$\Re^n \to \mathbb{C}^m$$

where $m = n - c$, c being the number of constraints Possible solutions to the constrained problem lie within the subspace $\mathbb{C}$. The subspace $\mathbb{C}$ can be represented by a set of m dimensional linearly independent vectors. These vectors comprise a basis of the subspace and a solution to the constrained problem must be a linear combination of these vectors [7]. The conditions for a minimum of the vector function then become.

2 18 $$\begin{gathered} A_{ij} x_j = b_i \\ Z_{ji} g(x) = 0 \\ Z_{ji} G(x) Z_{ij} \textit{ is positive definite} \end{gathered}$$

where A_{ij} is a matrix containing constraint equation coefficients, b_i is the constraint vector, Z_{ij} is a matrix containing the subspace basis vectors, $g(x)$ is the gradient of the function and $G(x)$ is the Hessian of the function. $Z_{ji} g(x)$ is referred to as the projected gradient since it projects the function's n-dimensional gradient into the m-dimensional subspace The location at which it vanishes is a constrained stationary point and is a possible minimum or saddle point The projected Hessian is used to determine if the point is a local minimum

One of POST's search methods is the projected gradient method that determines the values of the independent variables which produce minima The projected gradient solution process is similar to a root finding process. A detailed description of the method can be found in reference 7. An overview is as follows The defined constraints are used to determine the subspace basis vectors. The search is limited to points within that subspace The function, which in this case is the equation of motion, is evaluated using an initial guess for the independent variables The variables are then perturbed and the function gradient determined The gradient is used to determine the change in independent variables that produce the largest decrease in the cost function, referred to as the direction of steepest descent The independent variables are perturbed successively along the steepest descent direction until the function changes sign. The interval over which the function changed is successively reduced in size until the root is determined.

CHAPTER 3

POST MODEL

3.1 Modeling Approach

Trajectory analyses were performed using separate ascent and glide back models A branching type trajectory where the glide back trajectory 'branches' from the ascent trajectory and the separation conditions are automatically adjusted based on the vehicle's ability to meet or exceed glide back endpoint constraints was not used due to vehicle scaling not being incorporated into the version of POST used to conduct these studies Without vehicle scaling to match the stage sizes to the separation point, a non- optimal ascent would have to be flown to reduce the separation Mach number and a separation point with higher Mach number would be unobtainable To minimize the cost of placing the 330 lb payload in orbit, the vehicle must scale with adjustments made in separation Mach number Thus, separate ascent and glide back trajectory analyses were performed with the glide back trajectory beginning at the booster separation point of the ascent trajectory Weight to orbit was maximized in the ascent trajectory In the glide back trajectory, altitude upon reaching a heading alignment cylinder (HAC) at the landing site was maximized If the maximized glide back altitude at the HAC equaled or exceeded a minimum allowable HAC altitude the glide back was considered successful and no changes in the ascent trajectory were required If the maximized glide back altitude at the HAC was less than the allowable minimum then the booster size was reduced to reduce its separation point Mach number and increase glide back altitude at the HAC

3.2 Ascent Model

The ascent trajectory was optimized with a penalty function of maximum weight to orbit for the given SSL-1 vehicle and set of constraints summarized in section 3.2.1 Steering commands that shape the ascent trajectory and the launch azimuth were chosen as independent variables to be optimized for maximum weight to orbit The steering commands were defined using the pitch angle of the vehicle relative to an inertial launch coordinate system. The pitch angle was defined as a linear function of Mach number over defined intervals up to booster separation and as a linear function of time over defined intervals after booster separation Pitch angle was defined as a function of Mach number during the boost phase to match changes in steer commands with changes occurring in the aerodynamic characteristics. Time intervals were independent of changes in the trajectory occurring due to adjustment of pitch angle functions As a result, changes in vehicle attitude did not occur simultaneously with changes in aerodynamic characteristics such as those resulting from transonic effects, yielding a less than optimal solution The pitch function's linear coefficients of Mach number and time were defined as independent variables and optimized for maximum weight to orbit using a projected gradient optimization algorithm POST assumes that the attitude control system can produce pitch rates required for an optimal ascent and makes no check of the ability of control surfaces or thrust vectoring to produce those rates. Thus, constraints matching the expected ability of the control system were placed on the magnitude of the pitch rate coefficient.

The vehicle model consisted of a discrete stage representation of the vehicle with propulsion and aerodynamic characteristics of the SSL-1 vehicle. Each stage burns its propellant load based on the defined mass flow rate and is jettisoned The position of the vehicle's center of gravity was entered as a linear function of propellant consumed Propulsive forces were corrected for atmospheric pressure losses using the defined nozzle area The vehicle's aerodynamic data was input in tabular format for each vehicle configuration occurring during ascent. Linear interpolation was used to determine intermediate values

The Earth's gravity potential was defined using the Earth's oblate spheroid characteristics The 1976 standard atmosphere was used to specify atmospheric characteristics of density, pressure and temperature as a function of altitude Wind velocity and direction around Vandenberg Airforce Base were obtained from a range reference atmosphere in GRAM [8] Wind speed and direction as a function of altitude at Vandenberg Air Force Base launch site are shown in figures 3 1 and 3 2

Wind velocity and direction were entered in POST as a function of altitude using a table format Linear interpolation was used to determine intermediate values.

Vehicle initial conditions of velocity and position were specified to initiate the Runge Kutta integration Velocity initial conditions were defined as relative velocity magnitude, velocity azimuth angle and flight path angle relative to the horizontal plane at the launch site Position initial conditions were defined using geodetic altitude, geodetic latitude and longitude East of the prime meridian.

3.2.1 Ascent Trajectory Constraints

The maximization of weight to orbit was performed within seven flight constraints, four orbital constraints a launch constraint and the constraint that the booster must glide back to the HAC at or above a minimum allowable altitude determined from the length of the glide back. Since the ascent and glide back were separate analyses, the glide back altitude constraint could not be explicitly defined in the ascent trajectory. Instead, the altitude attained by a glide back trajectory was compared to the minimum allowable altitude and the ascent trajectory modified manually if the altitude was not met Flight constraints consisted of angle of attack limits, pitch rate limits, normal force limits and dynamic pressure limits Orbital constraints consisted of the altitude, inertial velocity, inclination and flight path angle required to maintain the desired circular polar orbit The launch constraint consisted of launch azimuth to ensure a launch direction within range safety requirements. These constraints are described below

Flight Constraints

1. Boost phase angle of attack constraint. The angle of attack throughout the boost phase was limited to ±18° due to the linear aerodynamic relationships used to predict the aerodynamic characteristics The data became inaccurate for angles of attack magnitudes greater than ±18°. After booster separation, no angle of attack limits were placed on the upper stages' trajectory The dynamic pressure after separation was low enough as not to require limiting angle of attack

2. Angle of attack at separation constraint: The combined vehicle's angle of attack at separation was limited between +2° and -6° to ensure a safe separation. Earlier studies conducted by Naftel [3] indicated that angle of attack had be within these bounds to safely fly the booster off the upper stages and maintain orientation control

3. Pitch rate constraint: The vehicle's pitch rate was limited to ±5 °/sec due to expected control system capabilities Historically launch vehicle control systems have been capable of pitching large vehicles at these rates

4 Normal force constraint The aerodynamic force acting normal to the booster wings was limited between -59750 lb and +47800 lb in the vehicle coordinate system These values are equivalent to the standard of +2 and -2 5 times the

vehicle landed weight

5. Maximum dynamic pressure constraint The maximum dynamic pressure during ascent was limited to 1000 lb/ft^2 The maximum dynamic pressure constraint ensures that variations in flight control or aerodynamics are not amplified to the point of producing unacceptably large variations in lift forces

6 Maximum dynamic pressure at separation. The dynamic pressure at separation was limited to 300 lb/ft^2 to limit aerodynamic forces during separation. Dynamic pressure amplifies any uncertainties and could produce error forces large enough to drive the vehicles together or produce flight instabilities if too large The 300 lb/ft^2 limit is based on Naftel's [9] a six DOF model used to determine angle of attack limits required to safely fly a booster away from an upper stage

7 The SSL-1 could only be trimmed using engine gimbal during ascent Canard and eleven deflections were not allowed during ascent

Launch Constraint

1 Launch azimuth: The launch azimuth was constrained between 165° and 200° East of North to ensure a Southward launch for range safety purposes

Orbital Constraints

1 Altitude constrained to 911450 ft ±500 ft

2 Inertial velocity constrained to 25425 ft/s ±100 ft/s

3 Inclination constrained to 90° ± 01°

4 Flight path angle constrained to $0° \pm .01°$

3.3 Glide Back Trajectory Model

The glide back to the landing site was performed on the basis of a landing maneuver similar to the Space Shuttle The maneuver uses a heading alignment cylinder to align the booster with the runway as shown in figure 3.3 After separation the booster would execute a turn until it obtains a heading tangent to the heading alignment cylinder, HAC Once reaching the HAC, the booster would begin a bank turn and travel along the HAC until it reached a point tangent with the runway azimuth This point is referred to as the nominal entry point, NEP At that point the booster would bank back to 0° and begin its approach The diameter of the HAC was calculated to be 23000 ft using a nominal 15° bank angle. The HAC was placed six nautical miles from the end of Vandenberg's 30 runway and tangent to its azimuth. The placement of the HAC was based on a distance required for safe approach, flare and landing determined in a landing analysis conducted for a similar glide back booster [9] Vandenberg's runway 30 was chosen so that the booster will land into the wind that predominantly blows off the ocean

The detailed landing maneuver was not included in the glide back trajectory to reduce the complexity of the analysis Instead, the glide back end point was targeted to the point on the HAC shown in figure 2 3 and the altitude at that point maximized The altitude obtained at the target point was then compared to an altitude goal The goal was calculated using the requirements for a glide back control system and landing maneuver developed by Naftel [9]

Naftel's study [9] indicated that a control system should have the ability to adjust the booster's glide slope up or down 20% throughout its glide once a heading to the HAC is obtained A nominal glide slope 20% lower than the maximum glide slope calculated in POST will have to be flown to allow that capability. In addition, Naftel [9] indicated that the booster should be at an altitude of approximately 10 kft when it reaches the NEP The author developed a general altitude goal equation to determine the altitude at which the booster should reach the HAC target point The equation is given below.

$$h_{\min} = h_{HAC} + \kappa_g \left(\frac{D}{L} \right)_g \kappa_R \left[R_g + r_{HAC} \left(azvelr \cdot azrw \right) \right] + \kappa_{HAC} \left(\frac{D}{L} \right)_{HAC} \kappa_{arc} r_{HAC} \left[\arccos \left(azvelr \cdot azrw \right) + \theta_T \right]$$

Where $h_{\min}$ is the minimum altitude at the landing site, κ_g, κ_{HAC} are factors to account for the control system's required reduction in maximum glide slope and glide slope while on the heading alignment cylinder, κ_R, κ_{arc} are factors to account for expected variations in the glide range and arc length traveled on the heading alignment cylinder due to atmospheric and ascent performance variations and variations in the glide back heading tangent point on the HAC , R_g, r_{HAC} are the glide range and HAC radius, $azvelr$, $azrw$ are the azimuth of the booster heading at the HAC and the runway azimuth, θ_T is the angle between the runway azimuth and target point on the HAC and h_{HAC} is the recommended minimum altitude upon reaching the NEP If the glide back trajectory could be optimized to an altitude equal to or greater than the calculated altitude, it was considered acceptable

The structure of the glide back trajectory model was very similar to the ascent trajectory model. The two differed in definition of the penalty function and type of steering commands The booster glide back trajectory was optimized with a penalty function of maximum altitude upon returning to the target point on the HAC Glide back guidance commands were defined as aerodynamic angles rather than inertial pitch angles used in the ascent optimization Aerodynamic angles made the formulation of an initial guess of the guidance commands much easier POST optimized the initial guess of angle of attack and bank angle over defined intervals of the glide back for maximum altitude at the landing site. The booster's position and flight conditions at separation were used as initial conditions for the glide back trajectory Initial conditions were input relative to the local horizontal Aerodynamic data for the booster alone was entered in tabular format with linear interpolation used to determine intermediate values The description of the Earth's gravity, the atmosphere and winds were the same as for ascent

3.3.1 Glide Back Trajectory Constraints

The maximization of altitude upon returning to the landing site was performed within five flight constraints and two landing site constraints The maximum angle of attack, pitch rate, dynamic pressure and normal force constraints were the same as those for ascent An additional constraint forcing the angle of attack to increase just after separation was added to ensure the booster moved away from the upper stages The landing site constraints consisted of latitude and longitude of the HAC target point The landing constraints are summarized below

1 Geodetic Latitude of HAC · 34 6096°, ± 001°

2 East Longitude of HAC 239.4771°, ± 001°

CHAPTER 4

TRAJECTORY ANALYSES

4.1 Ascent Approaches

Due to the inability of the projected gradient optimization technique used in the POST analyses to alter the fundamental approach used in a trajectory's initial guess, different approaches of ascending to orbit were investigated to determine which is optimal An upright and an inverted ascent to orbit were investigated. For an upright ascent, the SSL-1 body Z axis was aligned with the launch azimuth (183° East of North) and the vehicle pitched nose down as it ascended to orbit For the inverted ascent, the SSL-1 body Z axis was aligned 3° East of North at launch and the vehicle pitched nose up as it ascended to orbit

The upright and inverted trajectories were significantly different Figures 4.1 through 4.6 compare the inertial pitch angle, flight path angle, angle of attack, lift, dynamic pressure and gimbal angel required to maintain trim. The differences arise as a result of the gimbal angle required to trim the vehicle In the upright approach positive gimbal angles are required to trim the aerodynamic moments which add to the positive gimbal angle required to direct the thrust through the C G This results in large gimbal angles and thrust vectoring losses for a lifting trajectory. The effect of trim losses on the upright ascent are evident in figures 4 7 and 4.8 that compare flight path angle and lift with and without trim With trim losses the vehicle doesn't have the ability to meet a dynamic pressure constraint at separation if it pitches over and generates lift As a result, the vehicle doesn't fly a lifting trajectory but rather climbs nearly vertical for 40 seconds before pitching over. Without trim, the vehicle is able to pitch over and develop lift and still climb to meet the separation q constraint

In an inverted ascent, negative gimbal angles are required to trim aerodynamic moments reducing the gimbal angle required to direct the thrust vector through the C G. Thus, lift helps reduce thrust vectoring losses for an inverted ascent This is evident in figures 4 4 and 4 6 that show lift and gimbal angel The vehicle pitches over and generates the maximum allowable lift which results in a reduction in gimbal angle Note that negative lift relative to the vehicle is upward lift relative to the ground for an inverted orientation Figure 4 9 shows that the booster performance is increased for the inverted ascent due to the utilization lift The separation Mach number is increased from 3 15 to 3 25

4.2 Optimal Ascent Trajectory

The weight to orbit performance is essentially equal for the upright and inverted ascent. The upright ascent achieves 1022 lb weight to orbit while the inverted ascent achieves 1020 lb This is surprising considering the inverted ascent's performance gain from lift The inverted ascent's slightly lower performance is a result of greater drag losses, atmospheric pressure losses and thrust vectoring losses offsetting the reduction in gravity losses shortly after separation Figures 4 10 through 4.14 show drag, atmospheric, thrust vectoring, gravity and total losses The inverted ascent's utilization of lift results in a flight path angle at separation that is 10° greater than the upright ascent. Its gravity losses increase during this phase of steeper ascent reducing the gains derived from lift. In addition, the upper stages must pitch over more to depress the flight path angle back to an optimal level required for attaining the orbit. The pitch over produces thrust vectoring losses large enough to increase the total losses above that of the upright ascent.

The extent to which constraints influence the trajectory differs between the two approaches The inverted ascent required that the limits of normal force and dynamic pressure be met to achieve the weight to orbit performance whereas the upright ascent's maximum normal force and dynamic pressure were well below the limits Thus, it is felt that there is more potential for increasing performance in the upright ascent

Due to the upright ascent's slightly greater weight to orbit performance and its greater potential for increased performance it is considered the optimal ascent trajectory Its weight to orbit performance of 1022 lb yields a payload of 384 lb exceeding the goal by 54 lb. The SSL-1 mass ratio (WTO/GLOW) for this trajectory is .0095

The optimal pitch angles determined by POST are shown in figure 4.1 The vehicle's flight path angle, altitude and velocity are shown in figures 4.2, 4.15 and 4.16 The flight path angle time history indicates that the vehicle maintains a near vertical climb for the first forty seconds of ascent. The initial drop in flight path angle was a result of the transverse velocity produced by trimming A 3.8° gimbal angle was required to trim the vehicle at launch producing a 10.5 lb transverse thrust component and 76° flight path angle The trimming effects were countered with a small positive pitch (nose up) immediately following a five-second rise from the launch pad over which time no steer commands were allowed. Steering commands are not allowed until the launch pad gantry is cleared to eliminate the possibility of the vehicle rotating into the gantry as a result of a pitch maneuver

The steep ascent during the first portion of the trajectory limits the SSL-1 ability to take advantage of lift. Lift is generated but at a flight path angle near 90° the orientation of the vehicle is such that lift does not offset gravity loss In addition, the trajectory must be bent over more abruptly following the vertical rise resulting in a negative angle of attack and negative lift. Figure 4 17 shows a plot of lift and normal force acting on the booster up to separation From the plot, it can be seen that only one third the allowable normal force is generated during the boost phase and that the majority of lift is negative as a result of the pitch over The net effect is that lift does little to offset gravity losses as would be desired for a winged configuration The trajectory seems to be less than optimal but is optimal for the given set of constraints and vehicle characteristics

The ascent trajectory doesn't fully utilize the SSL-1's lifting capability primarily due to the dynamic pressure constraint at separation. The vehicle's thrust to weight ratio is high at 1.42 . As a result, it accelerates quickly and if left unconstrained would produce high dynamic pressures during the boost phase To meet the dynamic pressure constraint at separation the vehicle climbs vertically to attain altitudes that offset the increasing velocity with decreasing density Density and dynamic pressure are shown as a function of Mach during the boost phase in figure 4 18 . The plot shows that the maximum allowable dynamic pressure is not attained when the 300 lb/ft^2 constraint is met at separation. The separation constraint has the effect of scaling the dynamic pressure relationship Figure 4 19 compares dynamic pressure during the boost phase with and without the dynamic pressure at separation constraint

The dynamic pressure constraint at separation determined the shape of the ascent trajectory As a result, neither the maximum normal force nor dynamic pressure constraints were met Eliminating the constraint at separation increases weight to orbit to 1038 lb yielding a 400 lb payload Figures 4.20 through 4.22 compare pitch angle, flight path angle and lift during the boost phase Eliminating the dynamic pressure constraint at separation allowed the vehicle to pitch over and take advantage of its lifting characteristics. The vehicle pitched over quickly after the 5 second rise and generated lift up to the allowable normal force limit The maximum allowable dynamic pressure was also nearly met as a result of flying lower in the atmosphere In addition to increasing lift, elimination of the separation q constraint also eliminated the negative lift portion of the boost phase and allowed a more efficient use of lift in reducing gravity losses

Lift is less costly in terms of drag losses during the subsonic phase of the trajectory For transonic speeds there are dramatic drag increases making low angles of attack and hence lower lift optimal Figure 4.23 shows the transonic drag increase with and without the q constraint at separation In addition, the lift to drag ratio decreases to half its subsonic maximum for transonic and supersonic speeds making lift more expensive in terms of losses due to drag at Mach numbers 1 and higher Figure 1 23 shows the maximum attainable lift to drag ratio as a function of Mach number The optimized trajectories reflect the trend of reducing angle of attack and lift for Mach numbers 1 and above Figures 4 24 and 4 25 show the vehicle's angle of attack and corresponding lift as a function of Mach with and without the q constraint at separation As the vehicle approaches Mach 1 the angle of attack is reduced During transonic speeds the angle of attack is reduced to 0° for the constrained case and to 2° for the unconstrained case Due to the parabolic nature of the drag coefficient/angle of attack relationship there is little increase in drag coefficient for small changes in angle of attack This allows the vehicle to fly at small angles of attack without incurring excessive drag penalties The trend of reducing alpha and lift for Mach numbers 1 and above is particularly evident in constraint sensitivity studies All trajectories reflect the trend regardless of constraint values. As a result, a non vertical launch was considered in the constraint sensitivity studies to determine the benefit of utilizing more subsonic lift.

4.3 Ascent Performance Sensitivities

4.3.1 Trim Effects

Trimming was required to balance thrust and aerodynamic moments. Thrust moments resulted from the center of gravity (C G) offset relative to the booster engines Aerodynamic pitch moments resulted from the pitch moment characteristics of the combined booster and upper stages. Engine gimbal was used to cancel moments generated during ascent At liftoff, a 3 9° gimbal was required to direct the resultant thrust vector through the C.G and eliminate thrust moments The gimbal angle increased as the vehicle ascended due to rearward C G movement and development of aerodynamic pitch moments Figure 4.26 shows the gimbal angle required to trim the vehicle during the boost phase. After separation, trimming was not significant due to the fact that the upper stages did not have a C.G. offset and that q was small and quickly dropped to zero

As mentioned earlier, the C G. movement of the booster/upper stages combination was approximated as a linear function of propellant consumed The gimbal required to maintain the resultant thrust vector acting through the C.G from launch to burnout also varied linearly from 3.9° to 8.2° . The gimbal angle required to trim aerodynamic moments is approximately the difference between the linear transition from 3.9° to 8 2° and the total gimbal angle It can be seen from figure 4 26 that the aerodynamic pitch moment adds between 1° and 2° of gimbal angle during the positive lifting portion of the boost phase increasing trim losses and decreases the gimbal angle by as much as 3° during the negative lift phase reducing trim losses. The net effect of aerodynamic pitch moment on trim loss is negligible

4.3.2 C.G. Location Sensitivity

Moving the vehicle C G has opposing effects on the gimbal angle required to trim the C G offset moment and aerodynamic pitch moment Moving the C G forward reduces the gimbal angle required to direct the resultant thrust vector through the C G and eliminate the C.G offset moment. However, moving the C G forward increases the distance between the center of pressure and C G resulting in larger aerodynamic pitch moments and larger gimbal angles for trim. Figure 4 26 indicates that the C G position is the dominant factor in the gimbal requirement

Table 4.1 summarizes the effect of C.G movement on weight to orbit, payload and mass ratio Moving the C G. had little effect on weight to orbit. Moving the C G forward 7% of the reference length increased weight to orbit 2 lb while rearward movement of as much as 8% had almost no impact on weight to orbit. This trend is as expected for the trajectory with the separation q constraint due to its small amounts of lift during the boost phase.

The effect of C G movement on weight to orbit is reversed for a high lifting trajectory Table 4 2 summarizes the effect of C G. location on weight to orbit, payload and mass ratio for the higher lift trajectory that results from eliminating the separation q constraint. For the high lift trajectory, moving the C.G. rearward up to 8% of the reference length increased weight to orbit 6 lb while moving it forward as much as 7% had no effect on weight to orbit

The gains in weight to orbit due to shifting the C G. location are no more than 0 5% while the losses are approximately 0% Thus, vehicle performance is considered insensitive to C.G location

4.3.3 Constraint Sensitivities

Of the constraints placed on the ascent trajectory, only the dynamic pressure at separation constraint impacted the trajectory The constraints placed on pitch rate, angle of attack, normal force and maximum dynamic pressure were not met during the ascent when the $\dot{q}$ constraint at separation was active Thus, q at separation was considered the driving factor in shaping the trajectory and influencing weight to orbit.

The dynamic pressure constraint at separation was varied to quantify its impact on weight to orbit. The constraint was varied from 250 lb/ft^2 to 500 lb/ft^2 in increments of 50 lb/ft^2 Figures 4 27 through 4.29 show the vehicle's flight path angle, lift and drag throughout the boost phase for each constraint value. Figure 4.27 indicates that the vehicle becomes sensitive to the constraint between 350 lb/ft^2 and 400 lb/ft^2 Dynamic pressure constraints 350 lb/ft^2 and below altered the trajectory from a lifting type trajectory to a vertical ascent that develops small amounts of lift. Figure 4 28 shows that there isn't an incremental decrease in lift as the constraint is incrementally reduced. Instead, there is a step change resulting in two groupings of lift magnitudes Figure 4 29 shows a similar trend for drag.

The weight to orbit, payload and mass ratio for each value of the separation q constraint are summarized in table 4 1 . The payload is not significantly impacted for constraint values of 400 lb/ft^2 and above This is consistent with the trend in lift

Below 400 lb/ft^2, the payload is impacted with the magnitude of loss increasing with each decrement in allowable dynamic pressure

The advantage of utilizing subsonic lift due to greater lift to drag ratios is evident for all values of dynamic pressure constraints. Figures 4 30 and 4 31 show that lift and angle of attack is sharply reduced for Mach numbers 1 and above (up to separation) to reduce drag losses

4.3.4 Launch Angle Sensitivity

The launch angle of the SSL-1 was made an independent variable to be optimized for maximum weight to orbit with and without the q constraint at separation This was done in an effort to develop more lift during the subsonic flight regime for the unconstrained case POST optimization determined the optimal launch angle to be $90°$ with the q constraint at separation active. This was as expected since the constraint forced the vehicle to climb vertically. However, POST optimization determined the optimal launch angle to be $2\ 5°$ off vertical without the constraint active Thus, no benefit is gained from orienting the vehicle in a position to generate lift from launch This is due to lift induced drag exceeding lift benefits at low speeds With a wingspan of only 32 ft, the SSL-1 has high span loading resulting in high lift induced drag at low Mach numbers

4.3.5 Wind Sensitivity

The ascent performance is insensitive to the mean atmospheric winds at Vandenberg's launch site Including the atmospheric wind profile into the ascent trajectory reduced weight to orbit 2 lb (0 2%) The high thrust to weight ratio and steep ascent negate wind effects Table 4.1 lists weight to orbit, payload and mass ratio with and without wind

4.3.6 Separation Point Sensitivity

The effect of booster staging conditions on weight to orbit performance was investigated by scaling the booster size The booster was scaled using the Vehicle Analysis Branch weights and sizing model Booster scaling was based on incremental changes in propellant load to influence the booster MECO Mach number The booster engines and upper stages were fixed in the scaling process since the design is constrained to use commercially available engines and upper stages Table 4.3 lists the booster length, dry weight, propellant weight and the SSL-1 GLOW for each change in propellant load

Figures 4 32 through 4 35 show Mach, altitude, flight path angle and lift during the boost phase for vehicle sizes corresponding to -5 klb, nominal, +5 klb and +10 klb changes in propellant Figures 4 32 and 4 33 indicate that separation Mach number increases with increasing size while separation altitude decreases. Figures 4 34 and

4 35 show the flight path angle and lift during the boost phase The vehicle pitches over and develops more lift as vehicle size increases The increased size reduces acceleration that leads to reduced q throughout the boost phase The vehicle doesn't have to climb as steeply to meet the q constraint at separation allowing it to pitch over and develop more lift during the boost phase.

The booster size has a lower bound in order to meet the separation q constraint. For propellant reductions exceeding 5 klb, the vehicle cannot climb to an altitude sufficient to reduce q before MECO occurs. Thus, the booster cannot be scaled below this size and meet the q constraint. At its minimum size, the SSL-1 weight to orbit performance and payload are 998 lb and 360 lb respectively. The booster's dry weight and GLOW at the lower bound are 22550 lb and 100775 lb respectively Table 4.1 summarizes weight to orbit, payload and mass ratio for each scaling. The mass ratio is based on the overall system to give an indication of system weight to orbit performance. The mass ratios decrease with increasing vehicle size The weight to orbit performance per pound of dry mass is highest at the booster's minimum size Based on this result, the separation Mach number should not be increased but rather decreased to reduce the cost of placing the payload in orbit This is counter to findings of earlier studies that found maximum efficiency to occur at separation Mach numbers near 6 0 [10] and minimum cost to occur for Mach numbers in the 3 3 to 3.5 range [11] due to the cost and operational expense of thermal structures required for the higher speeds The SSL-1 optimal separation point differs from the previous findings due to its constraints of fixed booster engines and fixed upper stages

4.4 Glide Back Approaches

Several glide back approaches were investigated in determining an optimal trajectory The approaches were based on the booster's flight conditions at separation, specifically its flight path angle, altitude and speed In general, an optimal approach to a glide back will be a function of the separation conditions as well as the aerodynamic and structural characteristics of the glide back vehicle. Due to the 52° flight path angle and 86 kft altitude at separation the dynamic pressure that develops aerodynamic force drops below 20 lb/ft^2 approximately 30 seconds after separation. Once q diminishes, the booster approximates a symmetric ballistic trajectory with a reentry flight path angle approximately the negative of the ascent flight path angle. Thus, the altitude attained after separation and the reentry flight path angle are determined by the booster's ascent flight path angle at the point where q diminishes. The maximum altitude attained by the booster can be reduced and its reentry flight path angle made less steep by decreasing the ascent flight path angle as much as possible during the 30 seconds following separation The reduced altitude and less steep reentry angle work together to reduce the reentry sink rate allowing the booster to arrest the downward velocity and begin its glide back to the landing site at higher altitudes However, decreasing the flight path angle increases the downrange position at which the glide back begins requiring a longer glide to the landing site The reverse is true if the flight path angle is increased after separation. For increasing flight path angle following separation, altitude is increased and reentry flight path angle becomes steeper This increases the reentry sink rate and reduces the altitude at which the glide begins However, the downrange distance is reduced requiring a shorter glide The optimal glide back will balance these opposing effects These characteristics form the basis of the glide back approaches.

The approaches to the glide back trajectories were based on upright and inverted separation Two inverted approaches were investigated In the first inverted approach the booster rolled to an upright orientation after reaching its peak altitude and performed a bank turn to attain a heading toward the landing site. The second inverted approach utilized an inside loop to obtain a heading toward the landing site A lateral separation (bank angle of 90°) was not investigated since the booster has unstable yaw characteristics for Mach numbers above 1 2 For a successful lateral separation, the vehicle would have to roll 90° and maintain a 0° slide slip trajectory Yaw control would be required to maintain 0° slide slip due gravity effects introducing the possibility yaw instability

In the first inverted separation approach, the booster separated in an inverted position and remained inverted at high angles of attack until reaching its maximum altitude at which point it rolled upright and maintained a high angle of attack descent until reentering denser portions of the atmosphere. Once q reached sufficiently high values, the booster began a bank turn. The inverted orientation developed downward lift reducing the ascent flight path angle and minimizing altitude attained after separation. The upright high angle of attack descent increased the reentry flight path angle and reduced the sink rate allowing for a higher altitude turn In the second inverted separation glide back approach (inside loop approach) the booster separated in an inverted orientation and maintained a high angle of attack inverted position until it looped back into an upright orientation with a heading toward the landing site No bank turn was performed to eliminate crossrange motion and reduce the length of glide back to the landing site In the upright separation glide back, the booster separated in an upright position and maintained an upright, high angle of attack position through descent When sufficiently high q was developed a bank turn was begun The upright orientation developed upward lift increasing the ascent flight path angle and minimizing the downrange travel

4.5 Optimal Glide Back Trajectory

For the ascent trajectory separation conditions and the booster's aerodynamic and structural limitations, the optimal glide back trajectory is an inverted separation trajectory Thus, a $180°$ roll will have to be performed during the ascent prior to booster separation for the booster to be in the optimal orientation for glide back The booster does not have the ability to perform an inside loop or upright separation glide back from its separation point with the imposed angle of attack and 2.5g normal force limits For the inside loop approach sufficient levels of q required to produce a 2.5 g turn do not occur until the booster descends to 75 kft. At 75 kft, the booster's flight path angle and speed are approximately -50° and Mach 2 5 respectively. Gravity and lift work together to increase the sink rate until γ reaches -90° Due to the increasingly large sink rate, the booster is unable to attain a flight path angle of -90° before reaching ground level

In the upright separation glide back, the booster made a successful turn back toward the landing site but reached ground level before reaching the HAC The upright separation depressed the reentry flight path angle 22° below that of the inverted separation. The steeper reentry significantly increased its sink rate resulting in the booster sinking to an altitude of 45 kft, 15 kft lower than inverted separation, before stopping its descent The booster was unable to glide back to the HAC from this lower altitude Figures 4 36 through 4 38 compares the inverted separation and upright separation glide backs latitude, longitude, altitude, and flight path angle.

For variations in lift and drag characteristics or changes in allowable normal force, the inverted separation glide back trajectory is not always optimal Studies of the SSL-1 booster with aerodynamic characteristics of a generic wing body design indicated the upright glide back trajectory became optimal when the allowable normal force was increased to 3g loads However, with the linear aerodynamic characteristics determined for the booster using APAS, this transition did not occur before the normal force limit was increased to 5g loads The results from this limited study suggest that for high drag aerodynamics coupled with high load limits the upright separation glide back trajectory is optimal while for low drag aerodynamics coupled with low normal force limits the inverted separation glide back trajectory is optimal. A general guideline as to the optimal approach for any vehicle and separation condition cannot be made based on these results. Further studies involving a broad range of vehicle characteristics and separation points would have to be performed to develop a general guideline

For the inverted separation glide back trajectory, the booster returns to the HAC at an altitude of 11995 ft and speed of Mach 55 when trimmed and gliding in mean wind conditions The booster reaches a maximum altitude of 146 kft and obtains a maximum range from the HAC target point of 51 nmi during the glide back. A heading toward the HAC target point is obtained 325 seconds after separation Figures 4.39 and 4 40 show the trajectory latitude, altitude, and distance form the HAC target as a function of longitude Figures 4 41 through 4 43 show the booster's altitude, Mach number, dynamic pressure, angle of attack, bank angle, flight path angle and heading azimuth over the first 350 seconds of the trajectory These figures show that the booster maintains its inverted position up to its peak altitude As the booster descended it rolled to a bank angle of 38° This initiated a slight Westward turn in its heading The dynamic pressure peaked between 150 and 200 seconds after separation. During this time, the bank angle increases to as much as 55° and the angle of attack is modulated to limit the maximum normal force to a 2 5g load. The pullup/bank maneuver stops the booster descent at 60 kft and turns its heading Northward. The booster speed drops to Mach 9 by the end of the maneuver due to high drag forces generated in the bank. Figure 4 44 and 4 45 show the lift, normal force and drag developed during the bank turn Between 200 and 325 seconds, the bank angle decreases to 0° when a heading toward the HAC is obtained. The heading toward the HAC is obtained near 325 seconds at 43 kft and 32 nmi from the target point. Once the HAC heading is obtained the bank angle is maintained at 0°

The glide slope that will be modulated by the control system was considered to begin when the flight path angle settled to a near constant value Figure 4.46 shows that γ settles to -8 5° at about 325 seconds after separation when the HAC heading is obtained The altitude margin required for this trajectory is calculated to be18813 ft The glide back altitude is 6819 ft below the goal Thus trajectory and/or vehicle changes are required for a successful glide back Modification of the separation point alone is not recommended during the initial development stage since it ignores increases in glide performance due to changes in vehicle characteristics Results from both ascent and glide back performance sensitivities studies should be considered using a multi-disciplinary approach to determine the most cost effective method of meeting the glide back constraint. Glide back performance sensitivities are presented below.

4.6 Glide Back Performance Sensitivities

4.6.1 Separation Point Sensitivity

The Mach number at which the booster separated was reduced by scaling the booster to its smallest allowable size The booster length was scaled down approximately 3 % resulting in 1 35 klb dry weight reduction and 5 klb propellant weight reduction. The booster could not be scaled below this point and meet the ascent constraint on q at separation. The ascent trajectory of the SSL-1 vehicle with the scaled down booster was optimized to determine the new separation point conditions. The new separation point conditions were used as the initial conditions of the glide back

Scaling the booster size down reduced the separation Mach number from 3 15 to 3.00, decreased the altitude at separation to 80786 ft, and increased the flight path angle to 61° Lowering the separation point Mach number to 3.00 increased the glide back altitude at the HAC 2830 ft to 14826 ft. This is 1740 ft below the desired altitude. Table 4 4 compares the range, altitude obtained at the HAC and altitude goal desired for the trajectory glide range For the given vehicle aerodynamic and structural limitations, it is not possible to utilize vehicle scaling alone to attain the required glide back altitude Aerodynamic and/or structural limitations of the booster must be changed for the SSL-1 to meet the mission constraint of the booster reaching the HAC with sufficient altitude

4.6.2 Sensitivity to Glide Back Constraints

The dominant constraint in the glide back trajectory is the maximum allowable normal force No other constraint limits are reached during the glide back with the exception of the limitation on angle of attack The normal force limit has a significant impact on the altitude attained at the heading alignment cylinder. By doubling the allowable normal force to 5g loads the altitude is nearly doubled, increasing to 23410 ft The normal force limit determines the booster's ability to stop its descent and turn back toward the landing site The glide back ranges, altitudes attained at the HAC target point and the desired altitude margins corresponding to maximum normal force limits ranging from 2 5g to 5.0g are listed in Table 4 4 . Figures 4.47 through 4 49 show the booster altitude, latitude and range versus longitude normal force limits from 2 5g to 5 0g The altitude gains from increasing normal force limits are evident in figure 4 47 As the allowable normal force is increased, the minimum turn radius of the booster is decreased. The decreasing turn radius reduces the range from the HAC and reduces the arc length of the glide back resulting in higher altitudes at the HAC A glide back that meets the altitude goal is possible if the normal force limit can be increased to 3 0g .

An interesting trend regarding the altitude at which the booster stops its descent is also seen in figure 4 47 As the allowable normal force increases, the altitude at which the descent stops decreases With higher normal force limits the booster has the ability to stop its descent at higher altitudes. However, POST optimization shows that it is more beneficial to steepen the reentry angle to reduce range and execute a smaller radius turn at a lower altitude than to make the reentry angle less steep and make a turn back to the HAC at a higher altitude. Refer to figures 4 50 and 4 51 for a plot of flight path angles and range from HAC corresponding to the normal force limits A comparison between the inverted separation glide back and upright separation glide back was made to determine which approach is optimal at a 5g normal force limit. Figure 4.51 shows that the two approaches are nearly equal with the inverted separation approach's altitude at HAC being slightly higher

4.6.3 Sensitivity to Ascent Constraints

Glide back performance is affected by the ascent constraint of limiting q at separation since it alters the separation point conditions from which the glide back starts The separation q constraint has an equally significant impact on glide back performance as does the normal force limit constraint Glide back altitude at the HAC increases significantly with increasing q at separation An altitude of 24603 ft is attained with a

q at separation of 500 lb/ft^2 Table 4 4 lists the range, altitude attained at the HAC and desired altitude goal for separation q values ranging from 300 lb/ft^2 to 500 lb/ft^2 Figures 4 52 through 4 56 compare altitude, range, flight path angle, lift and dynamic pressure for the various q limits. The effect of the q limit on altitude at the HAC is clear in figure 4 52 As q at separation increases the flight path angle at separation decreases, reducing the maximum altitude and making the reentry angle less steep Refer to figure 4 54 for plots of flight path angle As the maximum altitude is reduced, q throughout the arch of the trajectory increases to values sufficient to develop aerodynamic forces Figures 4.55 and 4.56 show plots of q and lift. The increasing aerodynamic force enables the booster to begin its turn sooner making significant changes in its heading earlier in the trajectory and reducing the glide back range Figure 4 53 shows that turn radius and range from the HAC is significantly reduced as q at separation increases. A glide back that meets the altitude goal is possible if the q at separation constraint can be increased to a value between 350 lb/ft^2 and 400 lb/ft^2

4.6.4 Sensitivity to Aerodynamic Data

The glide back performance is sensitive to the booster's aerodynamic lift and drag characteristics. The aerodynamic data used in the trajectory analyses was based on the assumptions of linear aerodynamic relationships As a result, angles of attack were limited to $\pm 18°$ throughout the glide back trajectory The glide back trajectory is significantly effected by the amount of drag that can be generated after separation and into its descent High angle of attack maneuvers increase drag and reduce the booster's speed and sink rate allowing the booster to stop its descent and perform a smaller radius turn back to the landing site. The aerodynamic data generated for the booster prevented such a maneuver from being performed However, aerodynamic data for a generic winged booster design was used that included lift and drag coefficients for angles of attack up to 60°. Performing a high angle of attack energy dissipation maneuver after separation with this data resulted in the booster reaching the HAC with an altitude approximately 20 kft above the desired goal. Wind tunnel testing is needed to determine the maximum angle of attack that the SSL-1 can be flown and still maintain trim and yaw stability from Mach 3 0 to subsonic flight.

4.6.5 Atomospheric Wind Sensitivity

The effects of mean atmospheric winds are minimal on the glide back performance. Without winds the altitude is reduced approximately 500 ft to 11488 ft Figures 4 57 through 4 62 compare altitude, latitude, flight path angle, heading azimuth, angle of attack, and bank angle with and without winds No significant changes in the trajectory are seen as a result of the mean winds Table 4.4 lists the glide back performance with and without wind The winds are beneficial to glide back performance due the booster performing its bank turn into the winds at an altitude where the wind velocity is peaking Figure 4 62 shows the bank turn that changes the booster's Westward heading of 270° to a Northeast heading of 40° occurs between 60 kft and 50 kft where the wind velocity peaks The axial component of the wind velocity increases the relative atmospheric velocity and hence q allowing increased turning performance. Note that the maximum normal force occurs during the turn from a Southward heading to a Westward heading and that q drops dramatically after this turn due to high drag force produced in the bank turn reducing velocity below Mach 1 The increases in q due to winds are usable and beneficial since they do not occur while the maximum normal force constraint is active

In addition to aiding the booster turn, the atmospheric wind has a tail wind component relative to the azimuth of the of the glide heading to the HAC The sensitivity to wind will change when the SSL-1 is launched from other sites due to differences in wind direction relative to the glide back heading. It is recommended that ascent/glide back trajectory optimization be performed for Wallops and Kennedy launch sites to quantify the wind sensitivities at those locations. This will allow any modifications in aerodynamic or structural limits required for those launch sites to be identified and incorporated into the conceptual design process

CHAPTER 5

CONCLUSIONS and RECOMMENDATIONS

5.1 Conclusions

- For the given vehicle configuration and constraints, the SSL-1 is unable to meet the mission constraint of gliding the booster back to the landing site HAC at a desired altitude goal of 18800 ft for the given aerodynamic and structural limitations However, it should be noted that the calculated altitude goal is sensitive to the estimated control system glide slope reduction and the range over which it is active A successful glide back may be possible with better estimates of these values
- A successful glide back may be possible with a high angle of attack drag maneuver after separation. Simulations using high angle of attack aerodynamic data for a generic winged booster design resulted in a glide back to the landing site HAC at an altitude of 38 kft
- For fixed booster engines and upper stages, the SSL-1 mass ratio improves as the booster size is reduced and separation Mach number lowered If the restriction of using fixed booster engine sizes and fixed upper stage sizes is removed, the SSL-1 mass ratio can be improved with increasing booster size

- With the booster engine thrust and upper stages being held constant, the booster cannot be scaled down to a size that reduces the separation Mach number to a point where a successful glide back can be performed.
- The SSL-1 booster size cannot be reduced more than 3% and meet the dynamic pressure constraint at separation For size reductions exceeding 3%, the booster MECO and separation occurs at an altitude to low for the constraint to be met
- The dynamic pressure limitation at separation is the dominant constraint influencing the SSL-1 ascent For the SSL-1 thrust to weight ratio, the q constraint forces the SSL-1 to ascend steeply and not utilize its lifting capability. Increasing q at separation increases both weight to orbit performance and glide back capability
- The influence of the dynamic pressure constraint at separation can be reduced with reductions in the SSL-1 thrust to weight ratio
- Weight to orbit performance is not sensitive to C G movements within ±7% of its reference length
- Weight to orbit performance is not sensitive to atmospheric winds
- Glide back performance is sensitive to the q at separation constraint A successful glide back can be performed with a q at separation value between 350 lb/ft^2 and 400 lb/ft^2
- Glide back performance is sensitive to the maximum allowable normal force

constraint. A successful glide back can be performed with a normal force limit of approximately 3.0 g.

- Atmospheric winds have a small impact on booster glide back capability

5.2 Recommendations

- Booster aerodynamic characteristics and maximum allowable angle of attack in the Mach 2.0 to 3.0 range should be determined. Glide back capability is significantly influenced by the drag that can be generated throughout this speed range.
- The separation maneuver should be investigated to determine the maximum dynamic pressure at which a safe separation can be performed.
- A booster control system should be approximated to determine what glide slope reductions will be needed and at what point the reductions will begin. The altitude goal calculated for a successful glide back is sensitive to the control system glide slope reduction and the range over which it is active.
- Glide back sensitivity to atmospheric winds at Wallops Island and Kennedy Space Center should be investigated. Wind effects at those locations are expected to be significant due to glide back headings having a larger windward component.

REFERENCES

References

1 Talay, T. A "Glideback Booster Application to Small Payload Launcher Development", NASA Langley Aerospace Systems, Concepts and Analysis Branch proposal, unpublished

2 Berry, J and Barlett, S "SR-2 System Requirements Review", Microcosm Incorporated, SBIR restricted rights data, unpublished.

3. Bonner, E , Clever, W. and Dun, K. Aerodynamic Preliminary Analysis System II Theory Manual, Rockwell International Corporation, Los Angeles California, NASA contractor report 182076, April 1991.

4 Bate, R., Mueller, D , White, J Fundamentals of Astrodynamics, Dover Publications Inc , New York, 1971

5 Sutton, G Rocket Propulsion Elements An Introduction to the Engineering of Rockets, John Wiley and Sons, Inc., New York, 1992.

6 Brauer, G , Cornick, D., Olson, D , Peterson, F , and Stevenson, R. Program to Optimize Simulated Trajectories (POST) Formulation Manual, Martin Marietta Corporation, Denver, Colorado1990

7 Gill, P., Murray, W , Wright, M. Practical Optimization, Academic Press Limited, San Diego, California, 1993

8 Justus, C , Jeffries W and Yung, S The NASA/MSFC Global Reference Atmospheric Model - 1995 Version (GRAM-95), NASA Technical Memorandum 4715, Marshall Space Flight Center, Huntsville, Alabama, August 1995

9 Naftel, J., Powell, R "Analysis of the Staging Maneuver and Booster Glideback Guidance for a Two-Stage, Winged, Fully Reusable Launch Vehicle", NASA Technical Paper 3335, 1993

10. Stanley, D., Talay, A., Lepsch, R., Naftel, J , and Cruz, C. "Parametric Trade Studies on a Shuttle II Launch System Architecture", NASA Technical Paper 3059, 1991

11 Freeman, D "Future Space Transportation System Study", *Astronautics and Aeronautics*, volume 21, no 6, 1983

12 Lepsch, R "CONSIZ weights and sizing program", NASA Langley Vehicle Analysis Branch, unpublished.

13 Rowell, L , Braun, R., Olds, J., Unal, R. "Multidisciplinary Conceptual Design Optimization of Space Transportation Systems", AIAA publications, New York, 1998.

APPENDICES

Appendix A

Tables

Table 1.1 . SSL-1 Vehicle Characteristics

	Booster	Stage 2	Stage 3
length (ft)	57 0	44 5	19.0
diameter (ft)	6 2	3 2	3 2
wing span (ft)	32 0	none	none
dry weight (Lb)	23906	3045	760
propellant weight (Lb)	55289	20814	2989
number of engines	4	2	1
vacuum thrust (kLb)	45 0	22.4	5 5
Isp (sec)	275 0	303 0	300 0
exit area (ft^2)	3 33	6 78	1 70
mass flow (slug/sec)	163 6	73 9	18 4

Table 4 1 Summary of Sensitivity Studies for Upright Ascent

Sensitivity Study	Weight to Orbit (Lb)	Payload (Lb)	Mass Ratio (E-3)
C G Location			
0 5	1024	386	9 558
0 525	1023	385	9 549
0 55	1023	385	9 549
0 57 (nominal)	1022	384	9 539
0 6	1022	384	9 539
0 625	1021	383	9 530
0 65	1022	384	9 539
Separation q limit			
250	1010	372	9 427
300 (nominal)	1022	384	9 539
350	1030	392	9.614
400	1034	396	9 651
450	1037	399	9 679
500	1038	400	9 689
MECO Mach Number			
3 00	998	360	9 900
3 15 (nominal)	1022	384	9 539
3 30	1046	408	9 250
3 40	1060	422	8 890
Wind			
mean wind	1022	384	9 539
no wind	1020	382	9 521

Table 4 2 Summary of Sensitivity Studies for Upright Ascent without the Dynamic Pressure at Separation Constraint

Sensitivity Study (without q limit at sep)	Weight to Orbit (Lb)	Payload (Lb)	Mass Ratio (E-3)
C G Location			
0 5	1037	399	9 679
0 525	1037	399	9 679
0 55	1037	399	9 679
0 57 (nominal)	1038	400	9 689
0 6	1039	401	9 698
0 625	1042	404	9 726
0 65	1044	406	9 745
MECO Mach Number			
2 85	986	348	10 420
3 00	998	360	9 900
3 15 (nominal)	1022	384	9 539
3 30	1046	408	9 250
3 40	1060	422	8.890

Table 4 3 SSL-1 Vehicle Scaling

Propellant Change (kLb)	Lref (ft)	dry weight (Lb)	propellant weight (Lb)	SSL-1 GLOW (Lb)
-10	53 61	21396	45291	94625
-5	55 36	22558	50282	100779
0 (nominal)	57 00	23906	22589	107134
5	58 54	24856	60286	113081
10	60 00	25989	65274	119202

Table 4 4 Summary of Sensitivity Studies for Inverted Separation Glide Back

Sensitivity Study	Glide Range	Alt. at HAC	Alt Margin Desired	Surplus/Deficit
	(nmi)	(ft)	(ft)	(ft)
Normal Force				
2.5g (nominal)	32 0	11995	18815	-6820
3 0g	20 0	15248	15585	-337
4 0g	12 5	20877	13950	6927
5 0g	8 0	23409	12970	10439
Separation q Limit				
300 (nominal)	32 0	11995	18815	-6820
350	25 0	15340	16675	-1335
400	15 0	18574	14495	4079
450	7 0	21964	12750	9214
500	1 0	24603	11730	12873
MECO point				
3 00	24 5	14826	16565	-1739
3 15 (nominal)	32 0	11995	18815	-6820
Wind				
mean wind	32 0	11995	18815	-6820
no wind	32 0	11488	18815	-7327

Appendix B

Figures

Figure I.1 : SSL-1 Booster

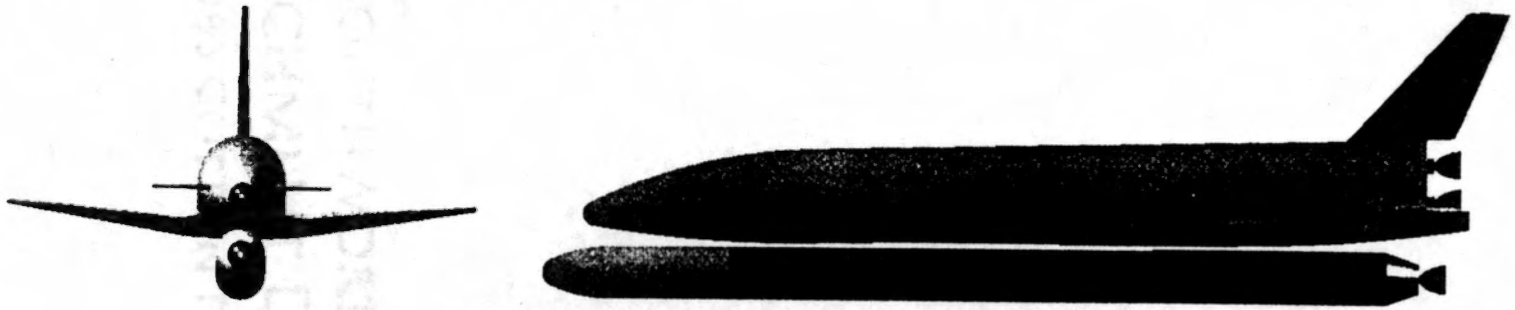

Figure I.2 : SSL-1 Booster with upper stages

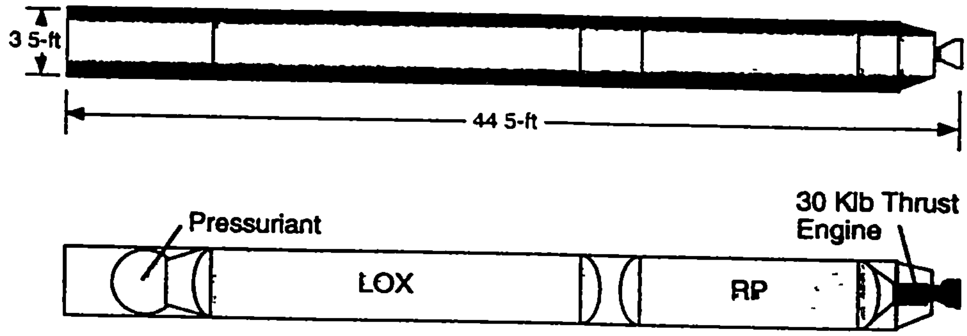

Stage 2 Expendable Design

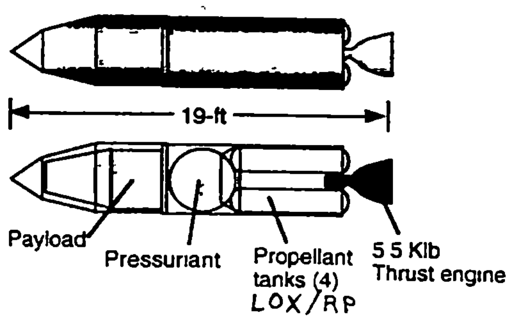

Stage 3 Expendable Design

Figure I.3 : SSL-1 Upper Stages

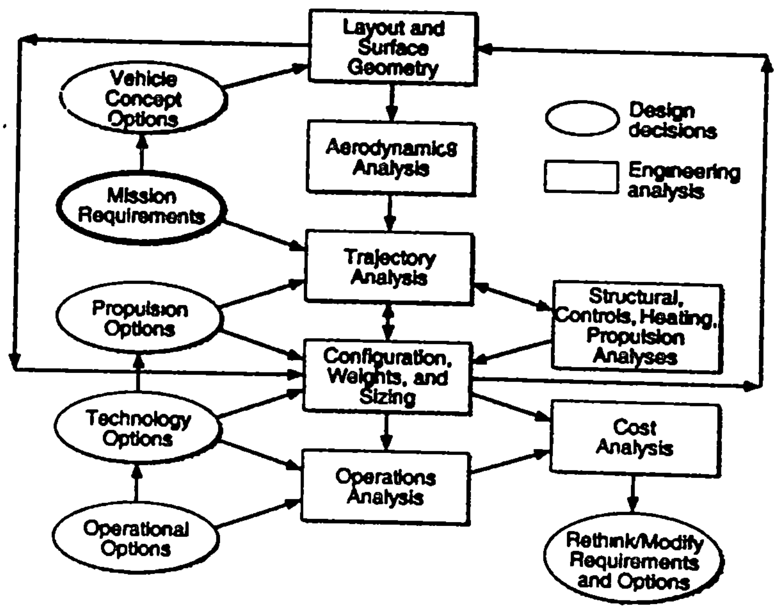

Figure I.4 : Vehicle Analysis Branch Conceptual Design Process
From Multidisciplinary Conceptual Design Optimization of Space Transportation Systems, AIAA 1998.

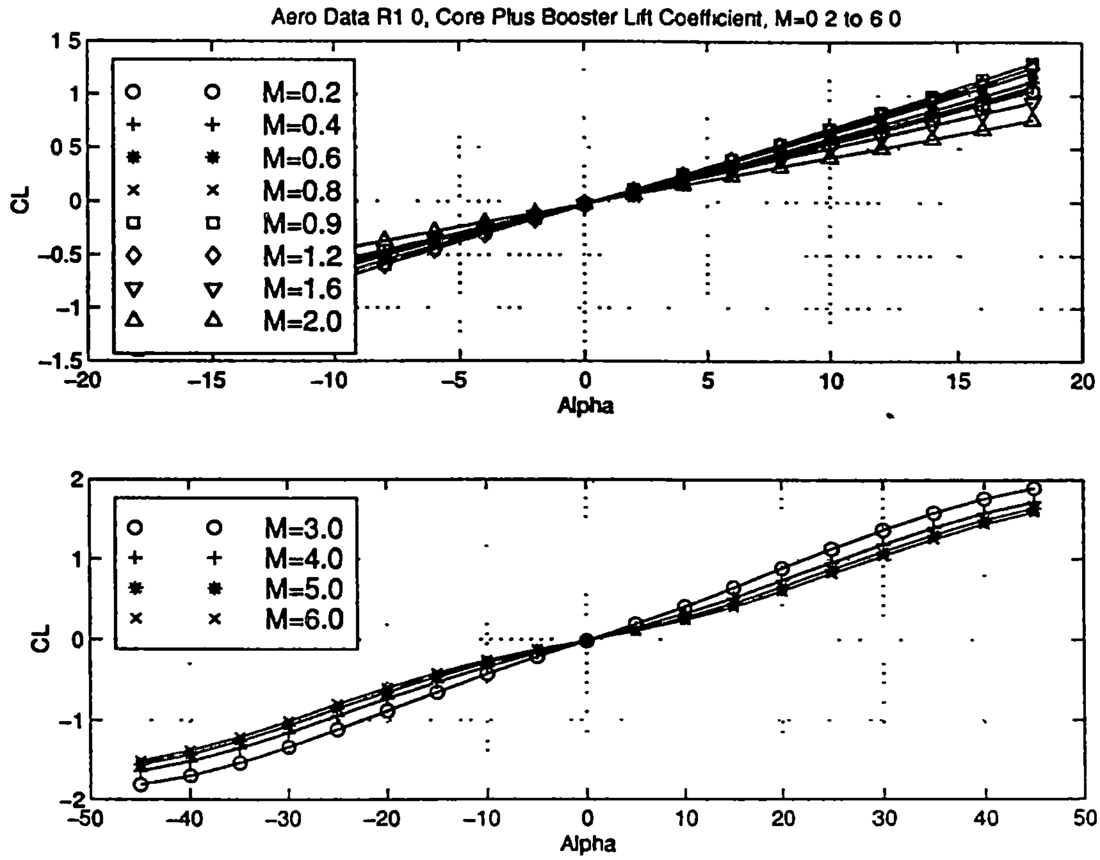

Figure 1 1 Booster with upper stages lift coefficient as a function of angle of attack for Mach numbers 0 2 to 6.0

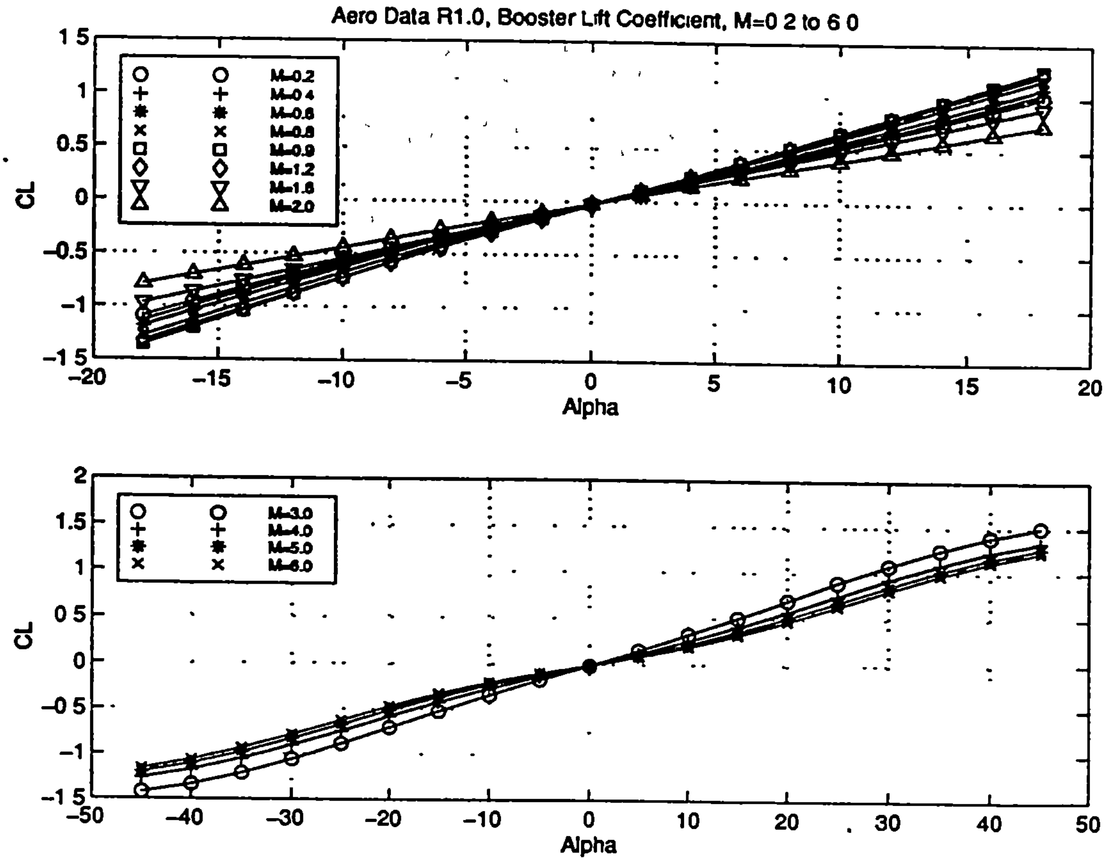

Figure 1.2 : Booster lift coefficient as function of angle of attack for Mach numbers .2 to 6.0

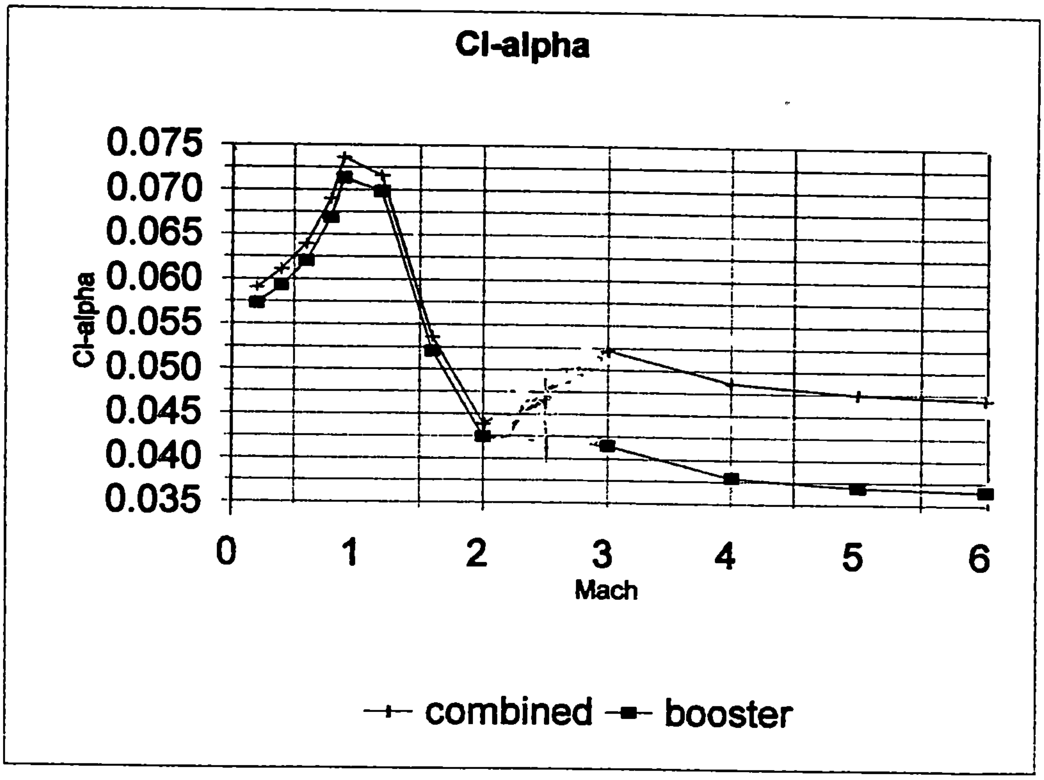

Figure 1 3 : $C_{L\alpha}$ of booster with and without upper stages

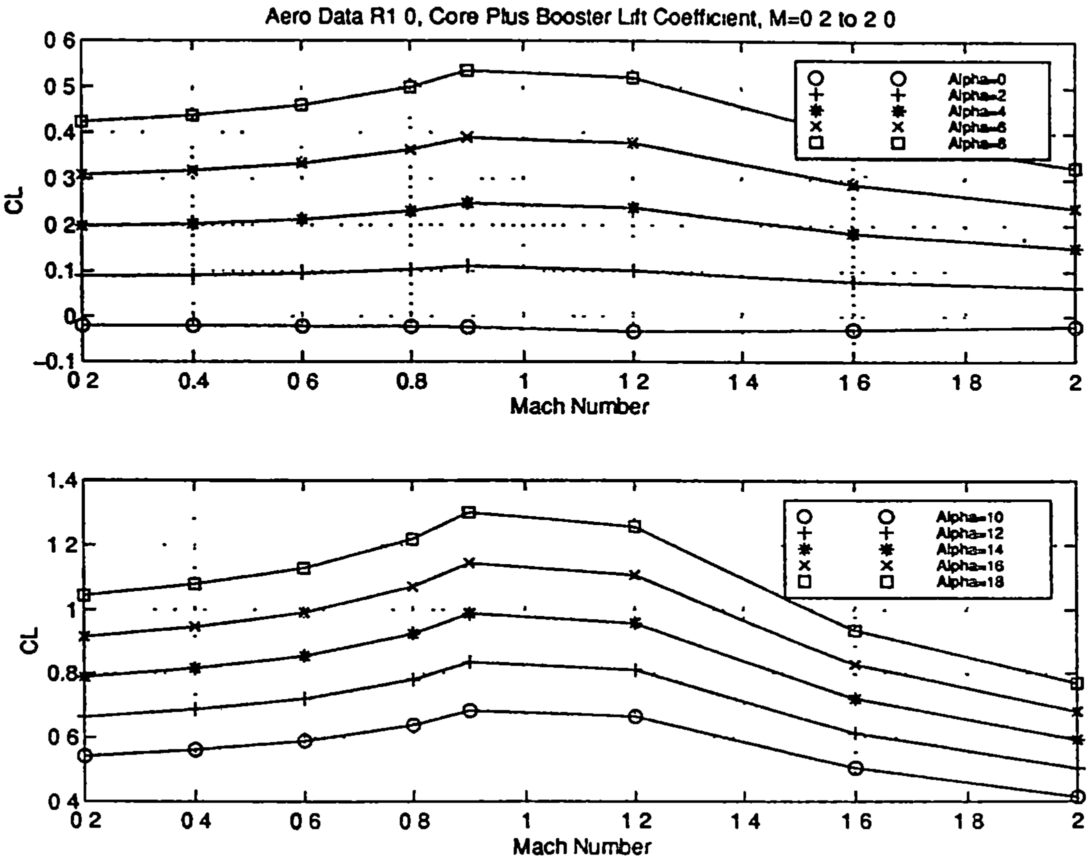

Figure 1.4 : Booster with upper stages lift coefficient as function of Mach

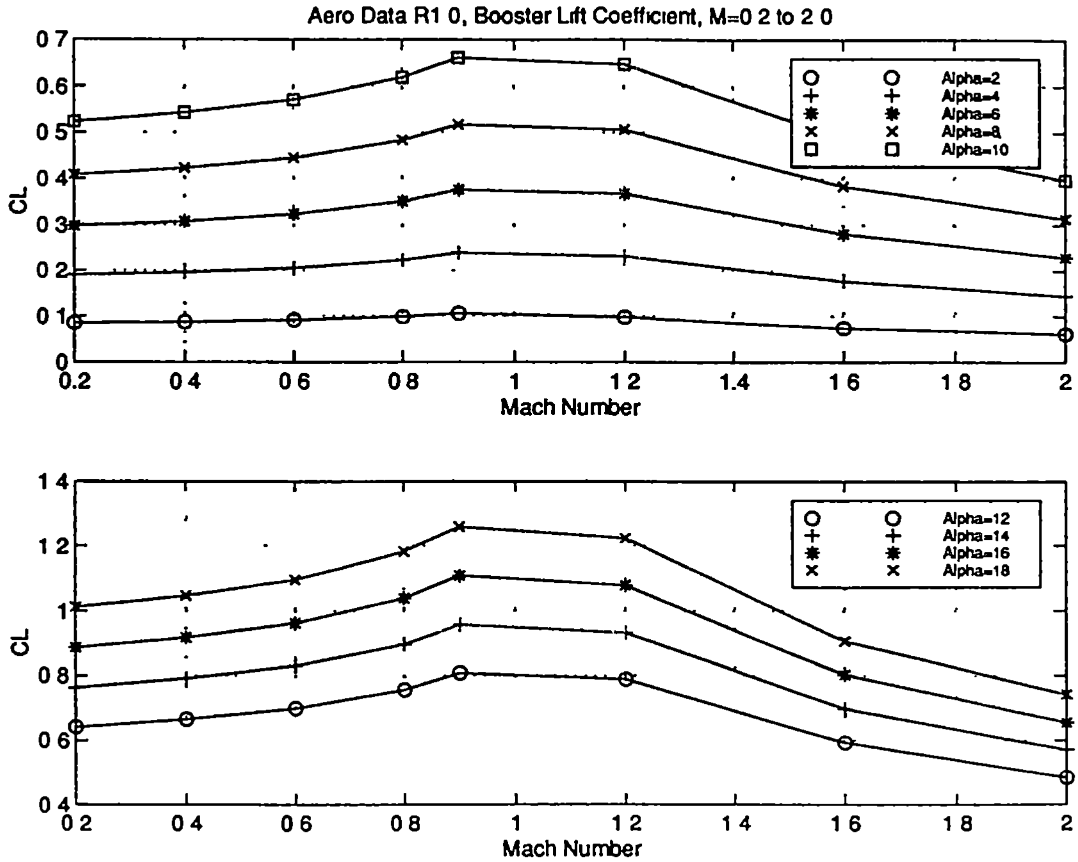

Figure 1.5 : Booster lift coefficient as function of Mach

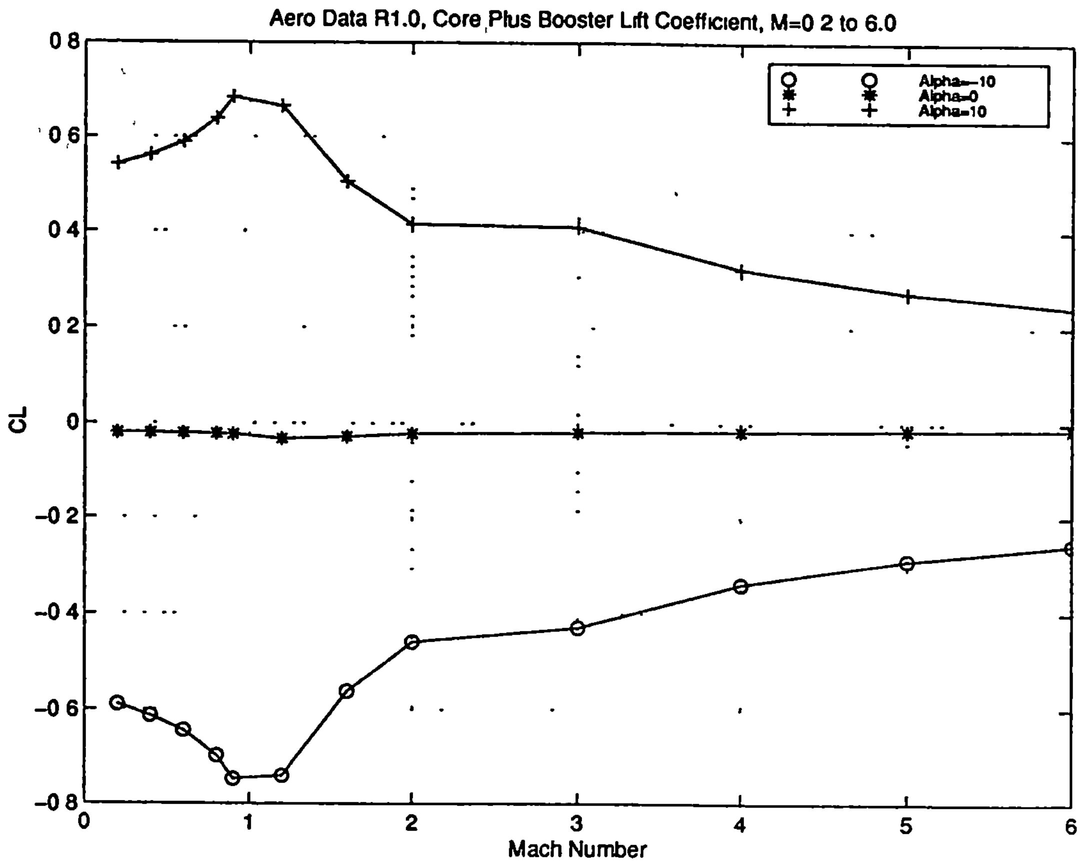

Figure 1.6 : Booster with upper stages lift coefficient as function of Mach up to Mach 6

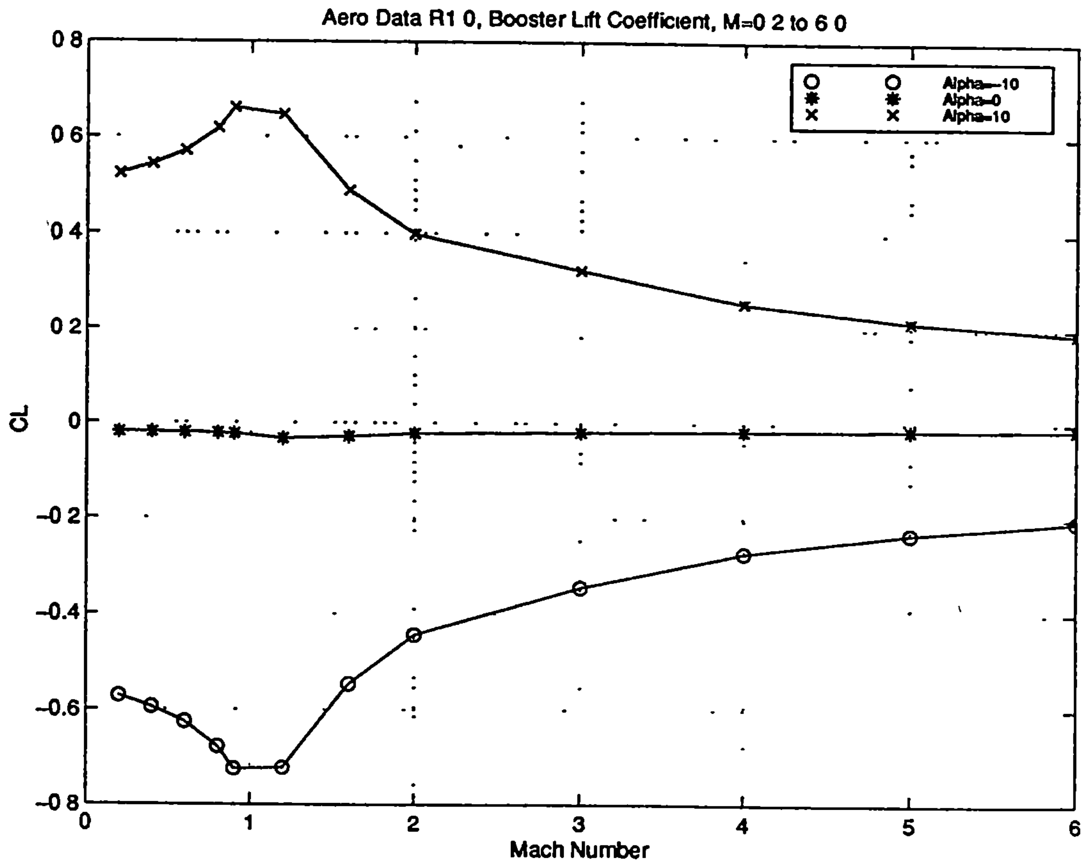

Figure 1.7 : Booster lift coefficient as function of Mach up to Mach 6.0

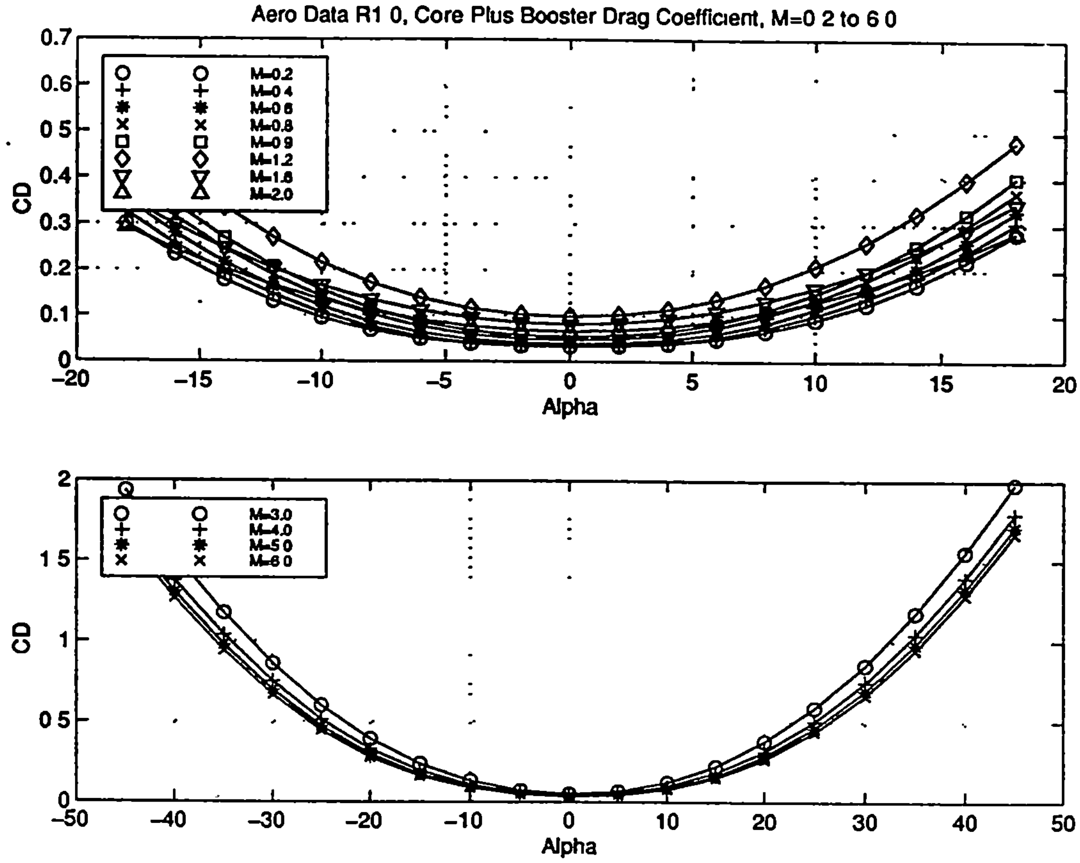

Figure 1 8 Booster with upper stages drag coefficient as a function of angle of attack for Mach numbers 0.2 to 6 0

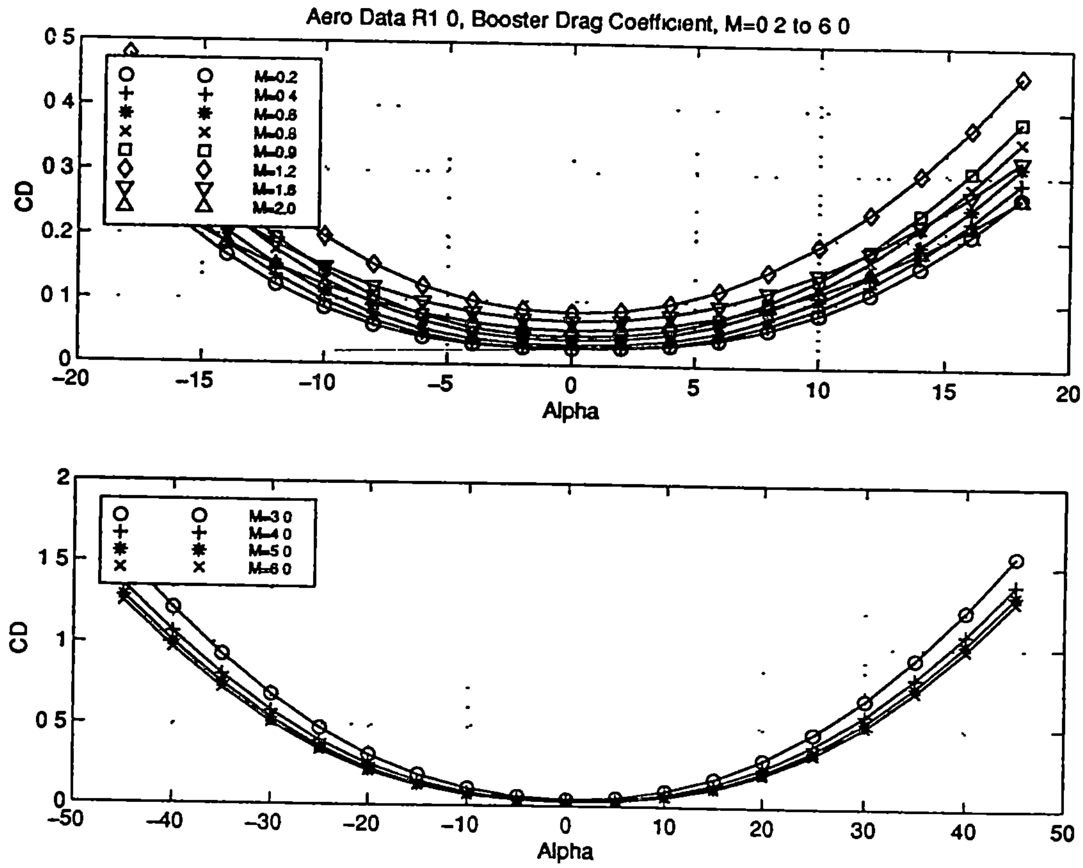

Figure 1.9 Booster drag coefficient as a function of angle of attack for Mach numbers 0 2 to 6 0

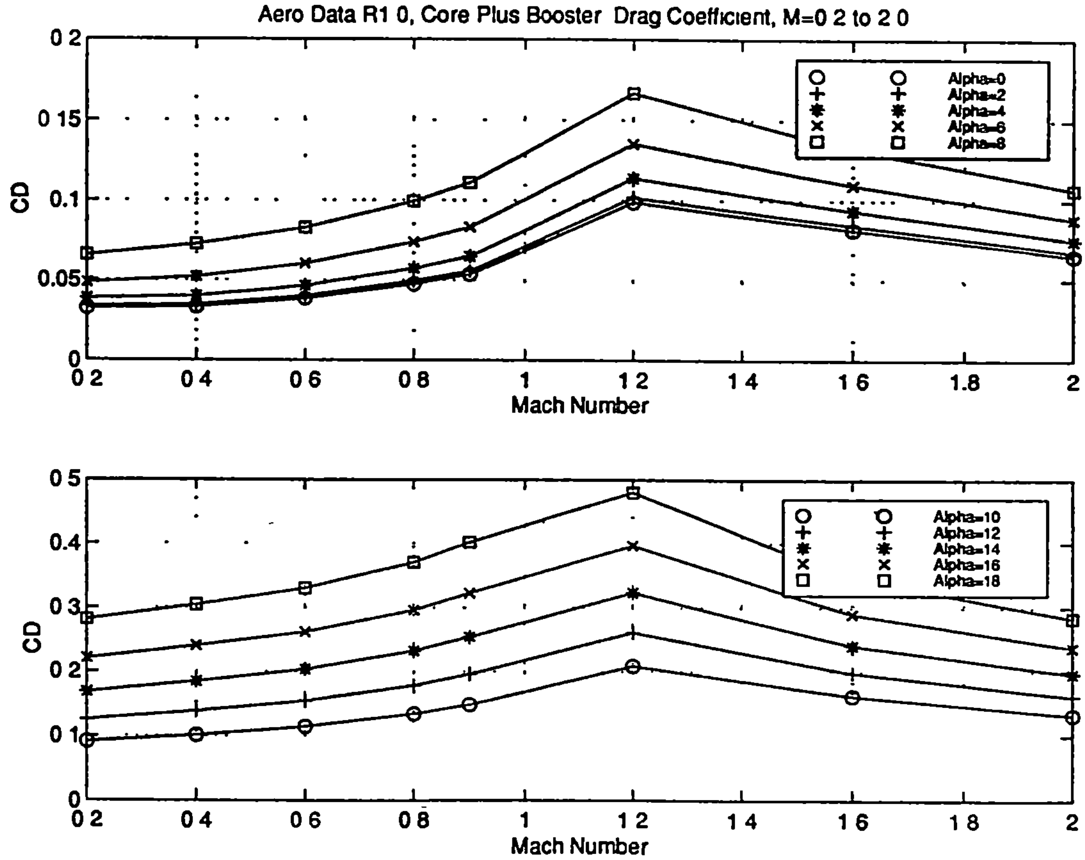

Figure 1.10 : Booster with upper stages drag coefficient as a function of Mach

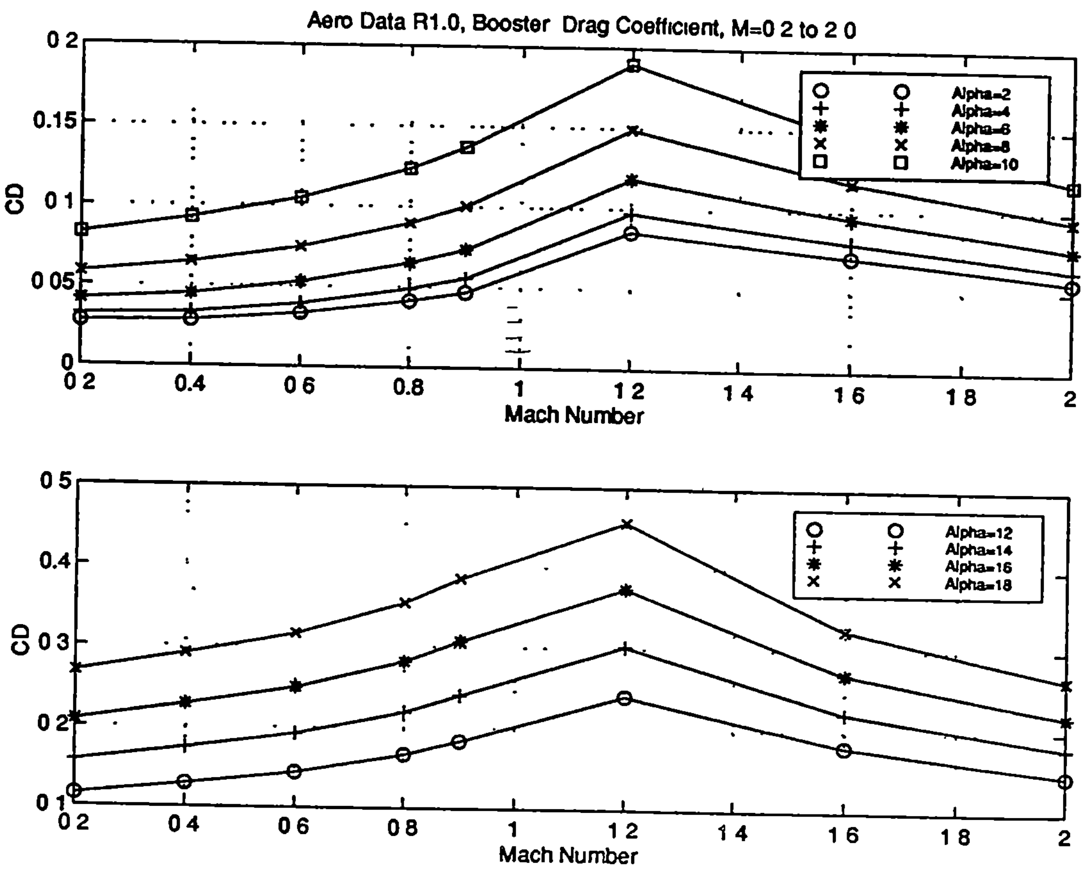

Figure 1 11 Booster drag coefficient as a function of Mach

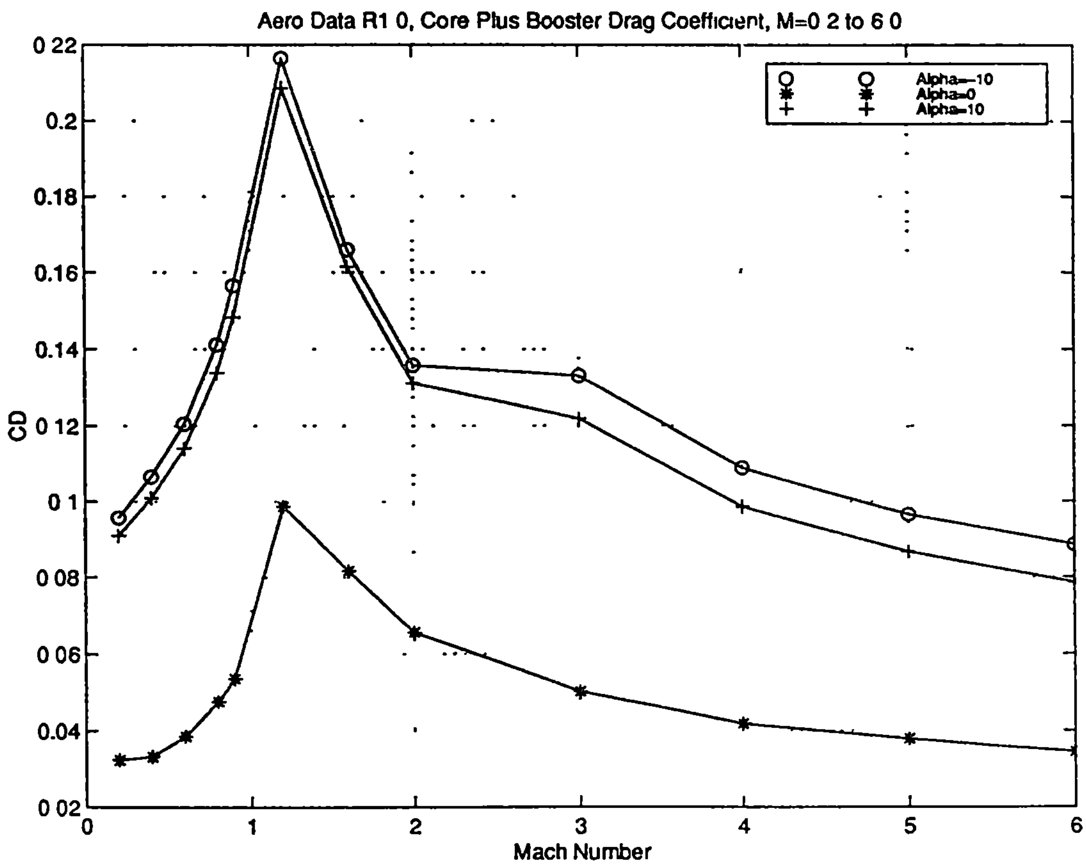

Figure 1 12 Booster with upper stages drag coefficient as a function of Mach up to Mach 6 0

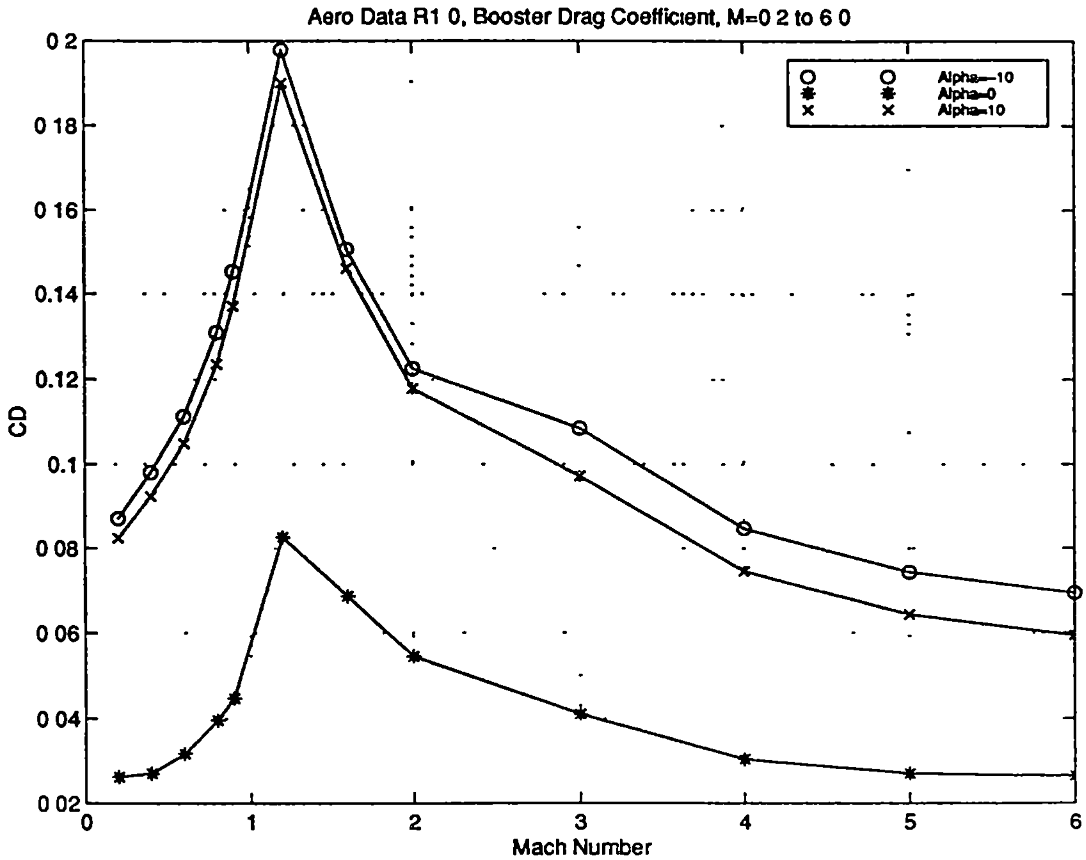

Figure 1 13 Booster with upper stages drag coefficient as a function of Mach up to Mach 6 0

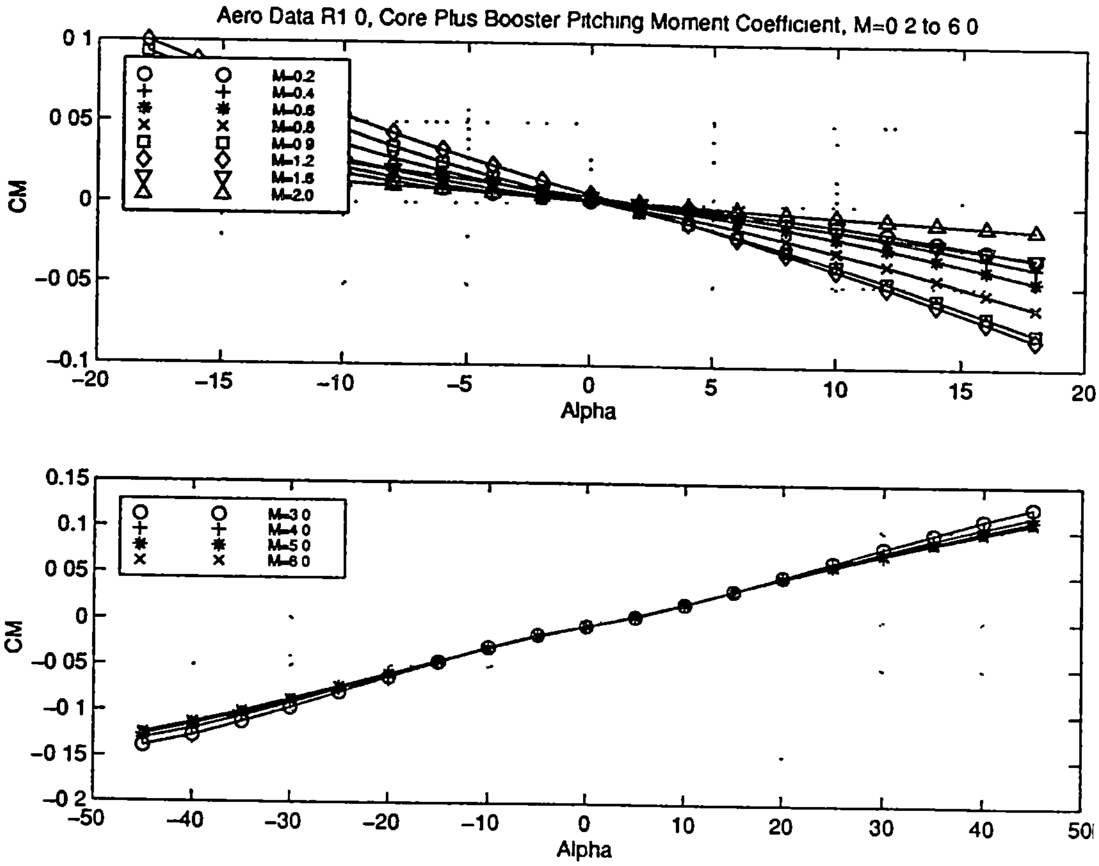

Figure 1 14 Booster with upper stages pitch moment coefficient as a function of angle of attack for Mach numbers 0 2 to 6 0

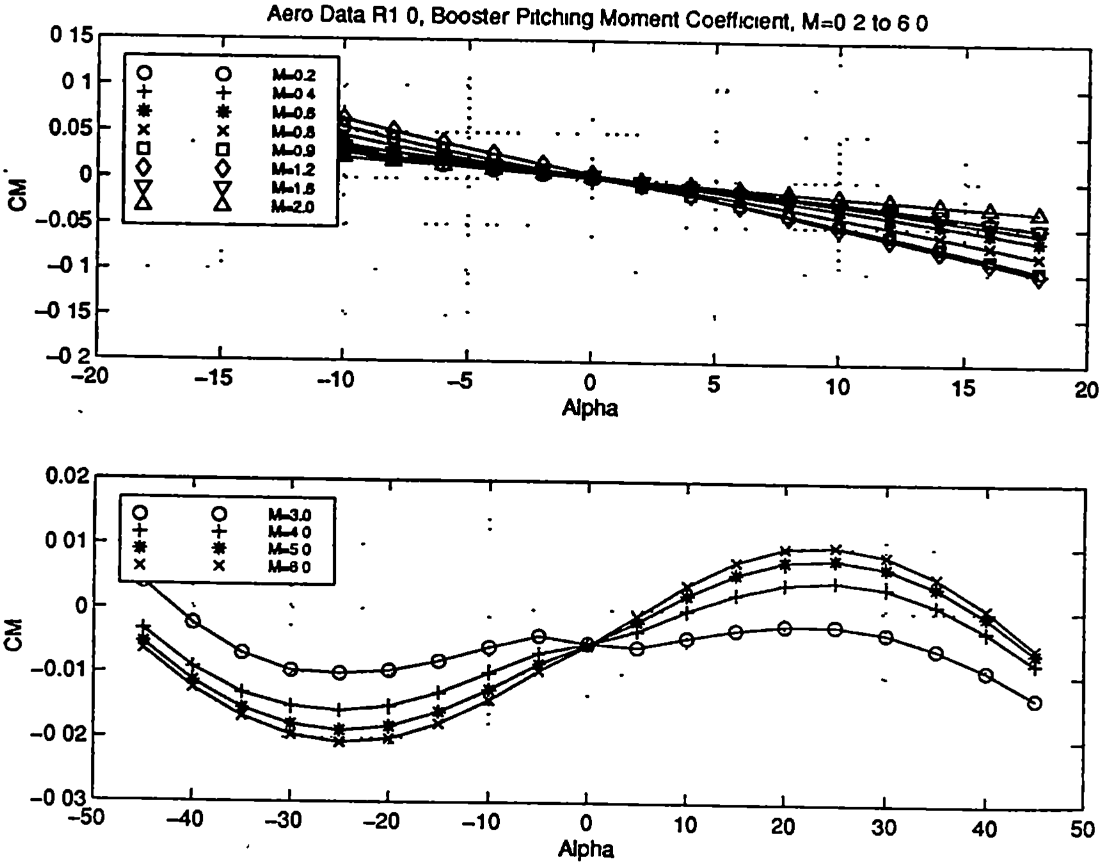

Figure 1 15 . Booster pitch moment coefficient as a function of angle of attack for Mach numbers 0 2 to 6 0

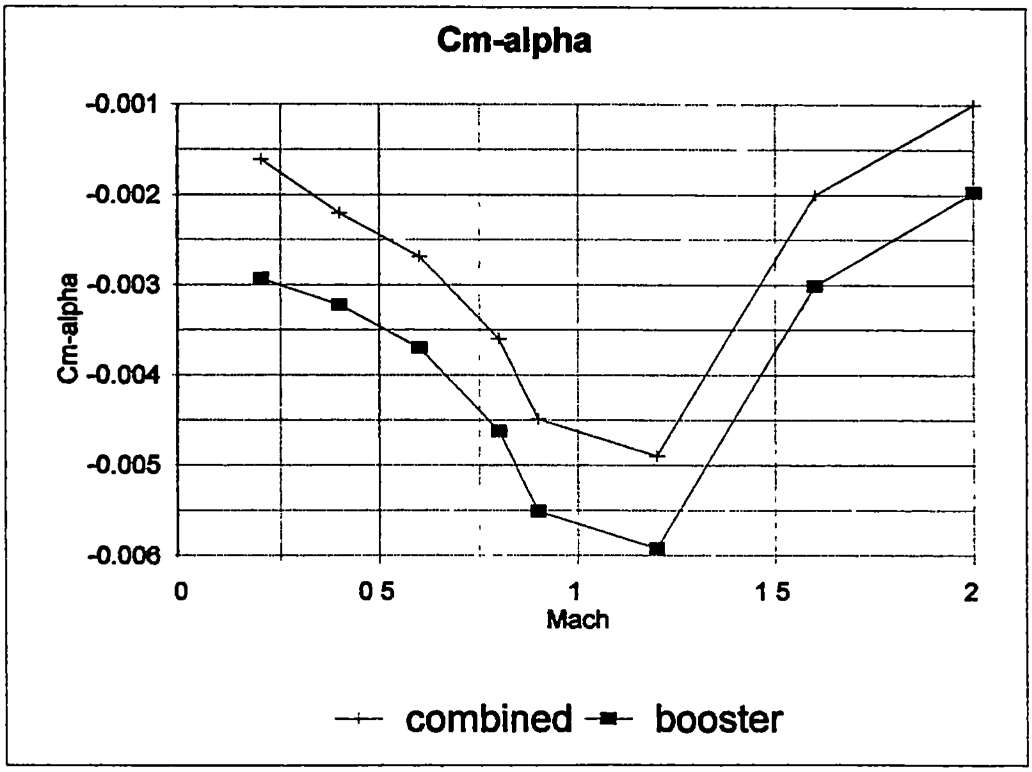

Figure 1 16 $C_{m\alpha}$ of booster with and without upper stages

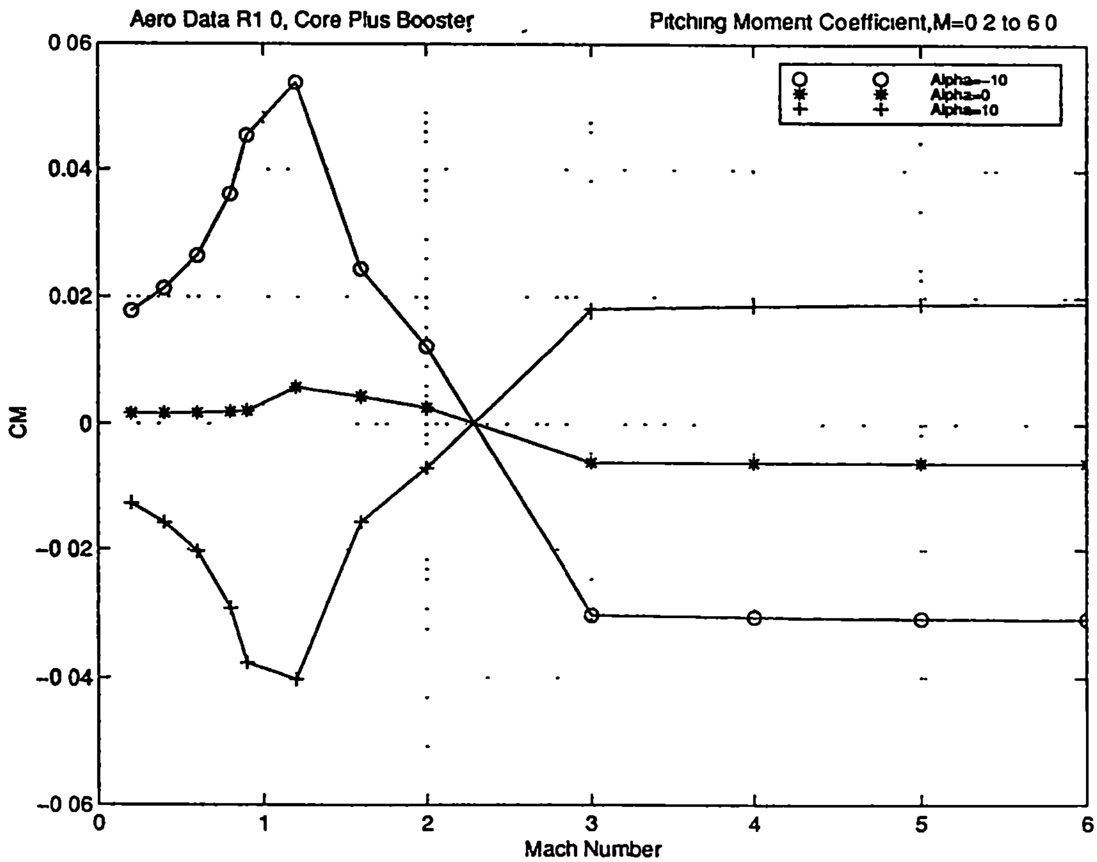

Figure 1 17 Booster with upper stages pitch moment coefficient as a function of Mach number up to Mach 6 0

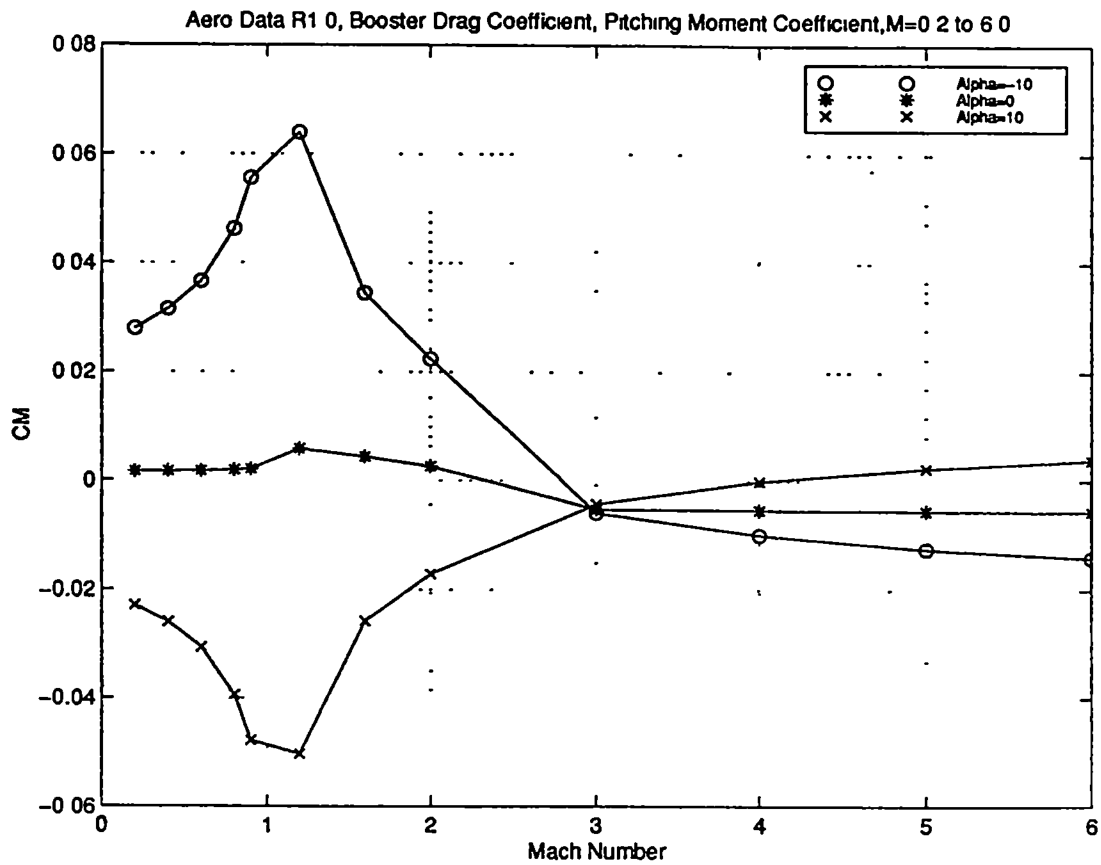

Figure 1 18 Booster pitch moment coefficient as a function of Mach number up to Mach 6 0

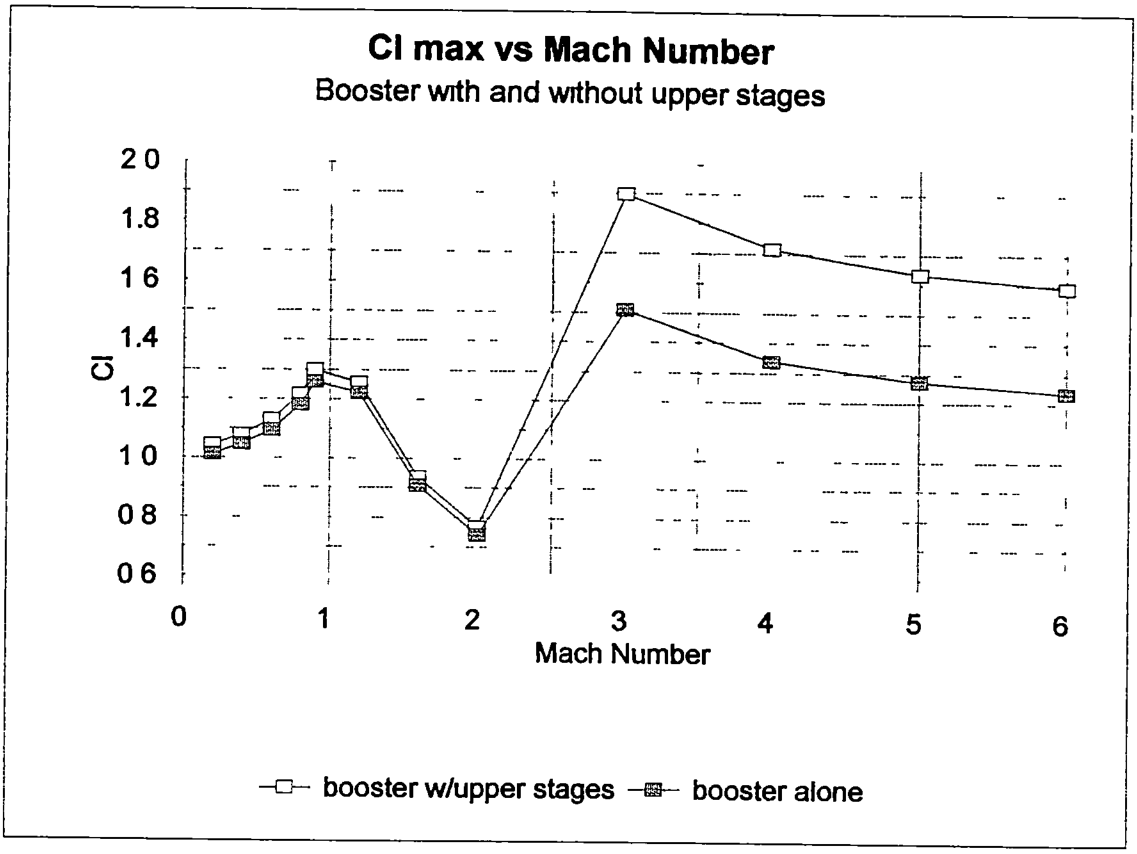

Figure 1 19 $C_{L\,max}$ of booster with and without upper stages

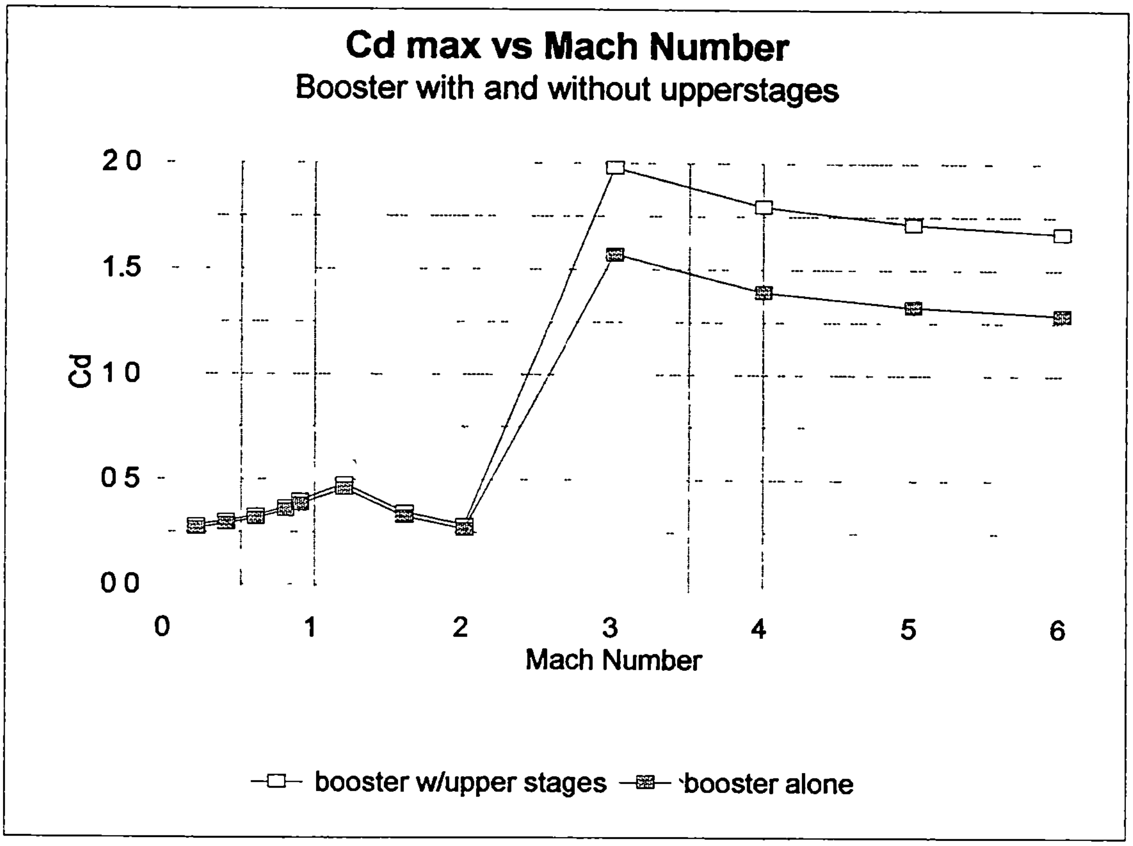

Figure 1 20 $C_{D\,max}$ of booster with and without upper stages

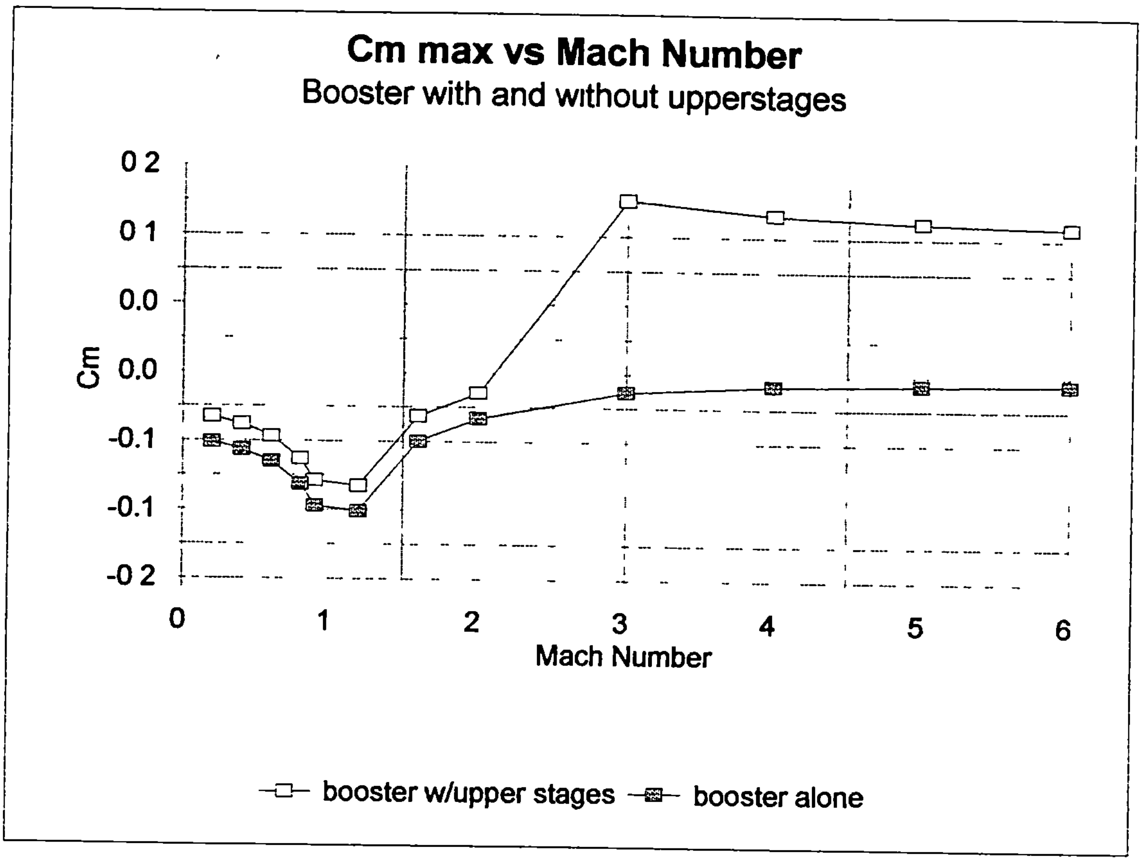

Figure 1 21 $C_{m\ max}$ of booster with and without upper stages

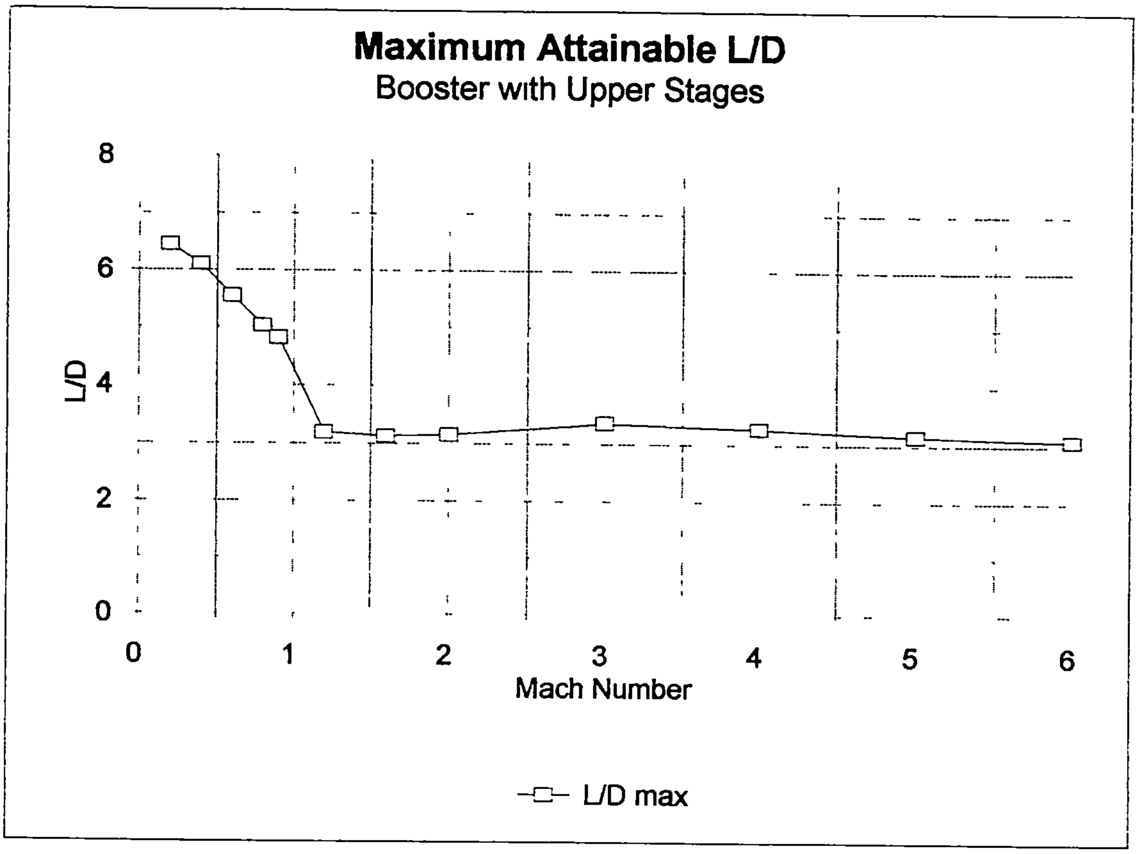

Figure 1 22 Maximum obtainable L/D

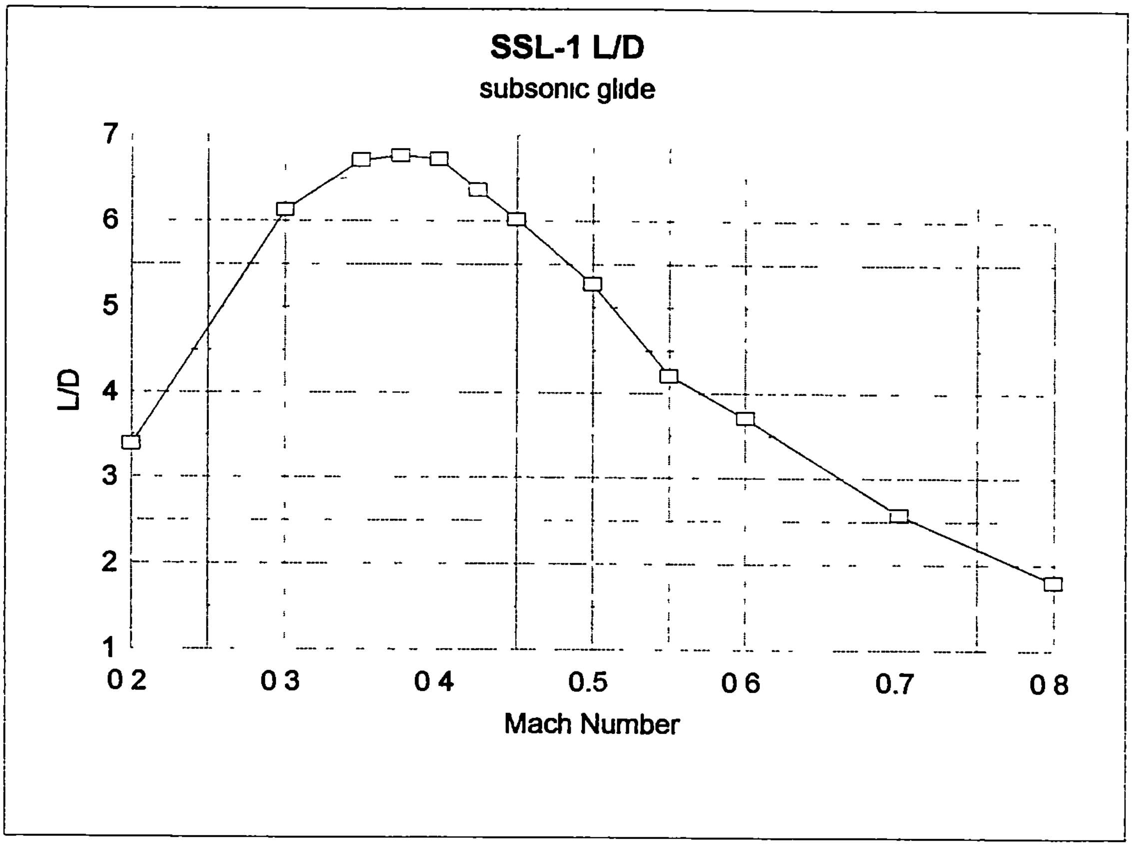

Figure 1 23 Maximum gliding L/D

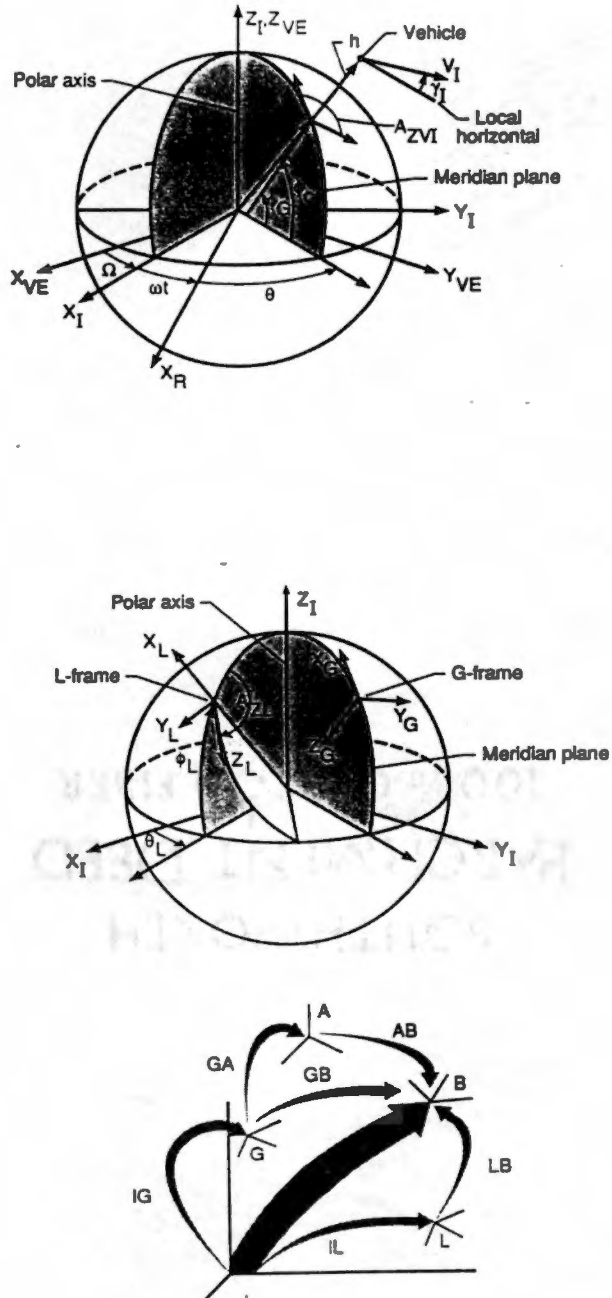

Figure 2.1 : Coordinate system transformations
Source: Program to Optimize Simulated Trajectories Formulation Manual, volume 1, September 1990

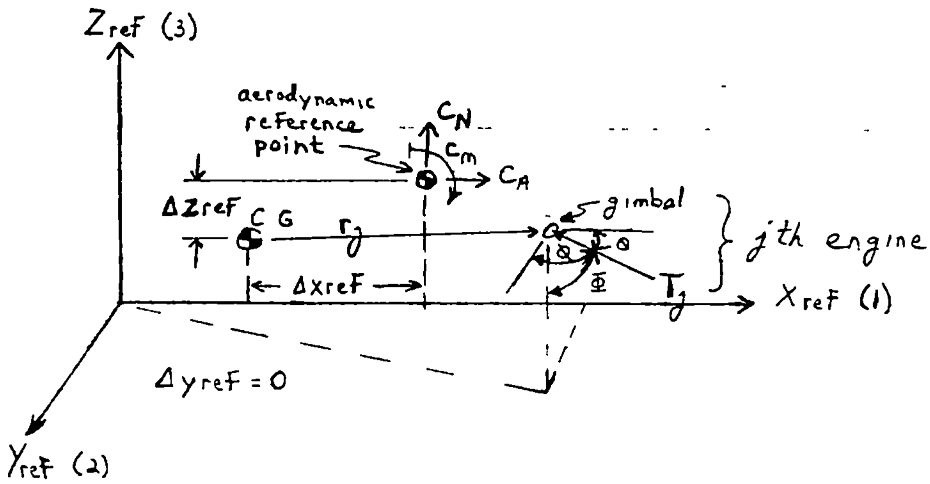

Figure 2 2 Engine Gimbal Moment Balance

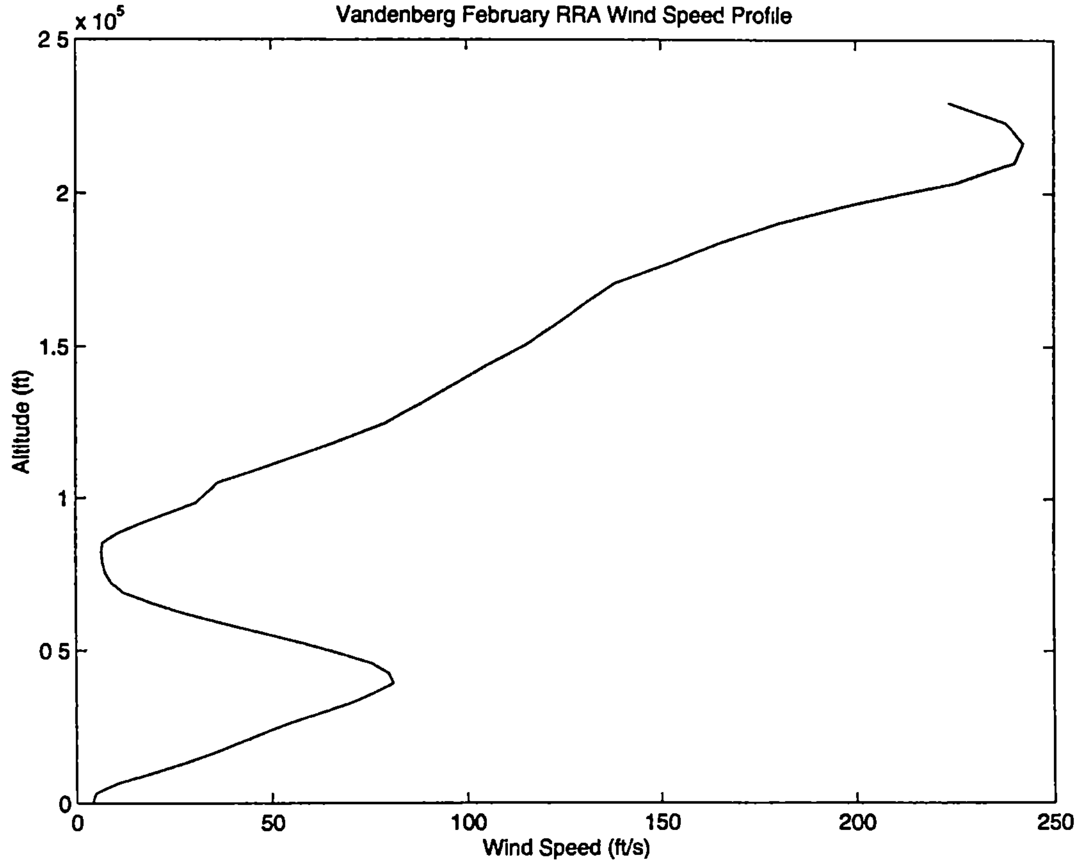

Figure 3.1 : Wind speed as a function of altitude at Vandenberg launch site

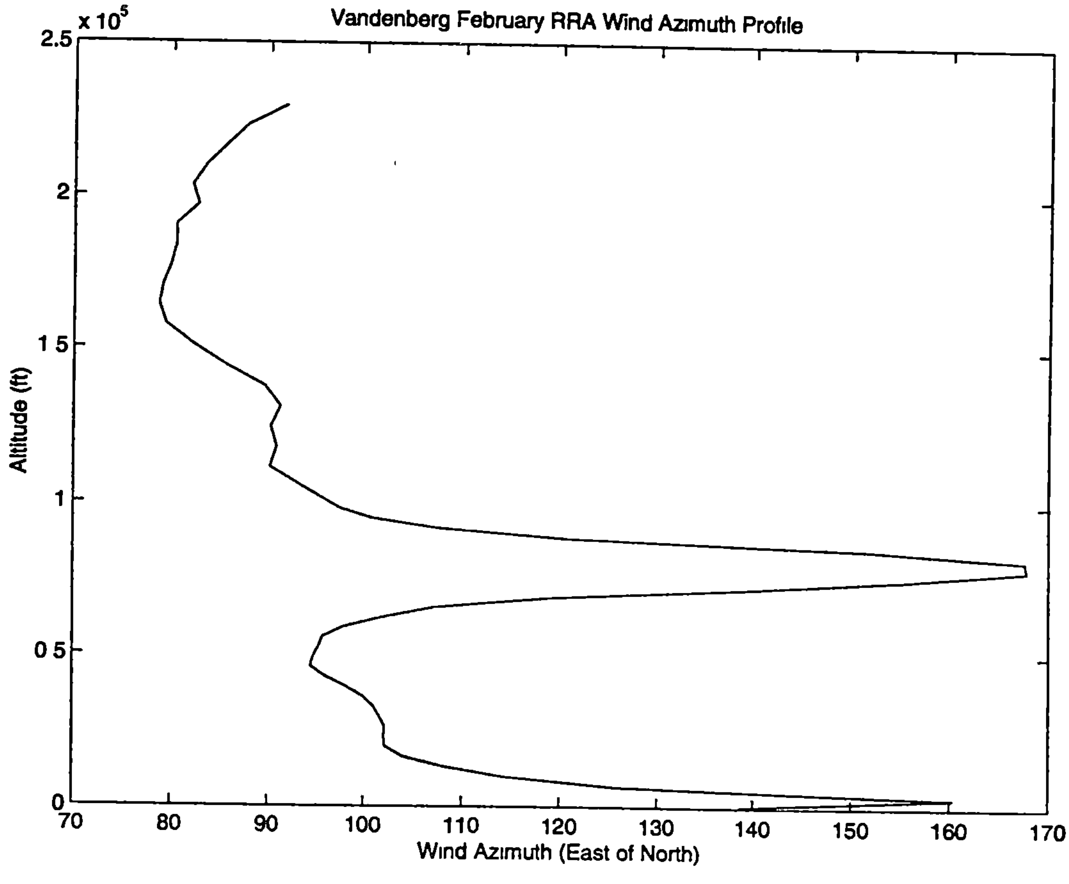

Figure 3.2 . Wind direction as a function of altitude at Vandenberg launch site

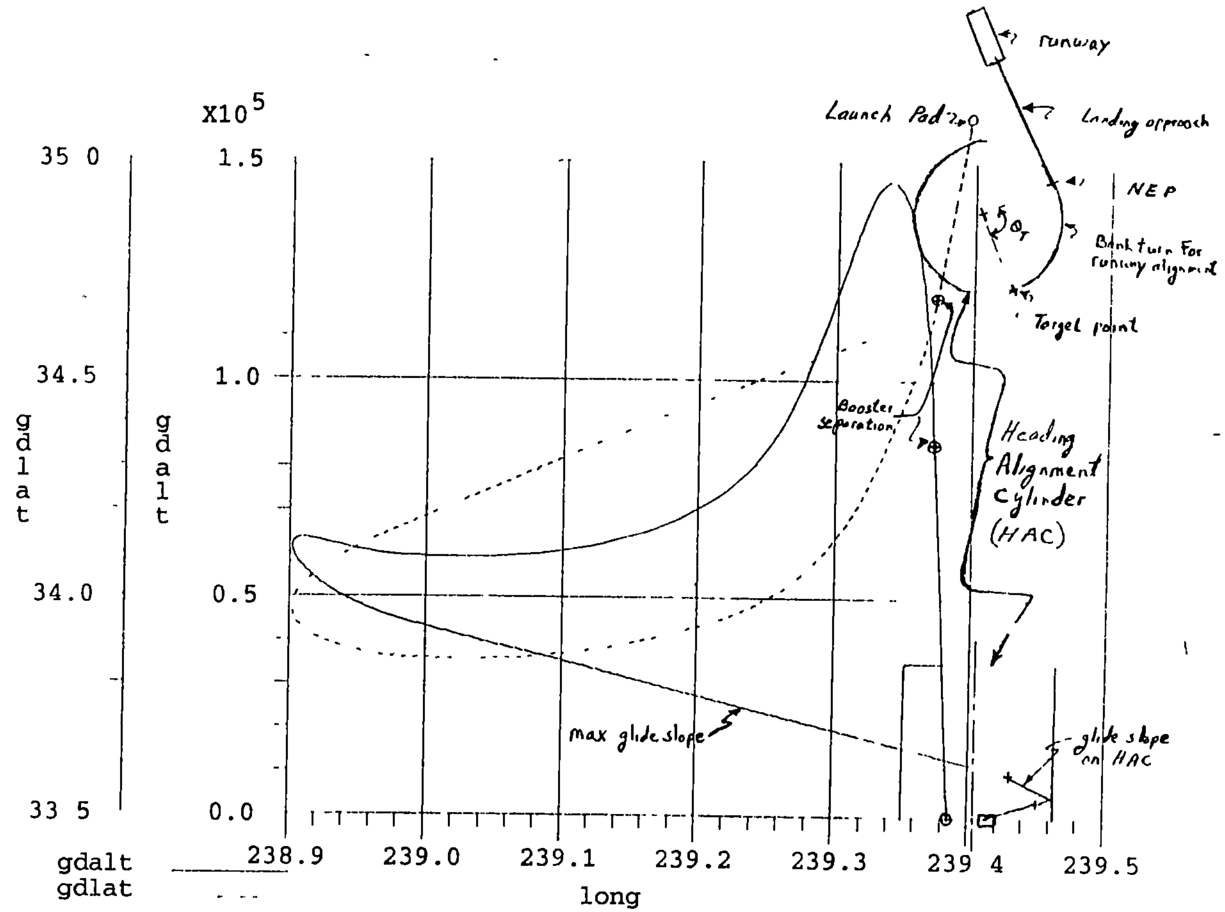

Figure 3.3 : Top and side view overlay of booster glide back trajectory with heading alignment cylinder and landing site

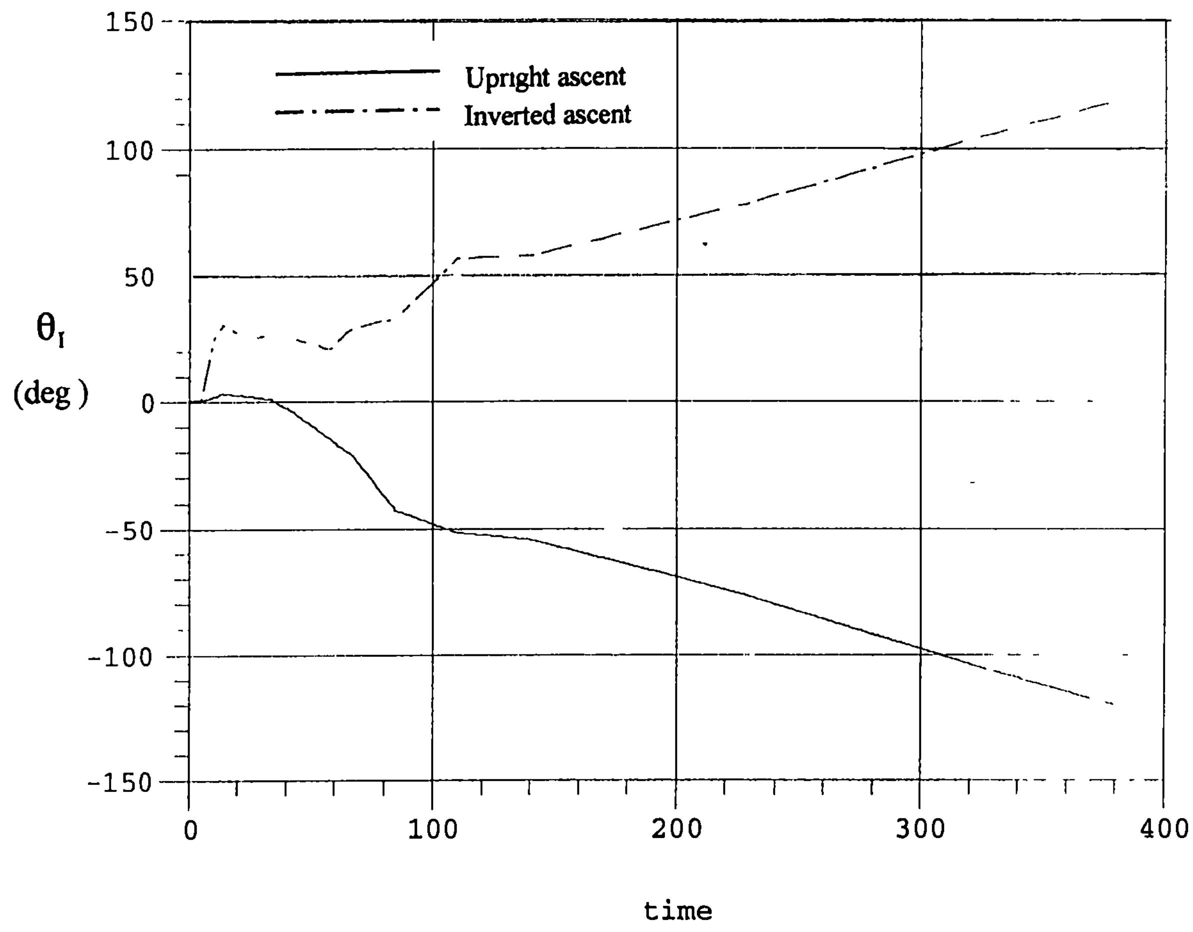

Figure 4.1 : Inertial pitch angles during upright and inverted ascent

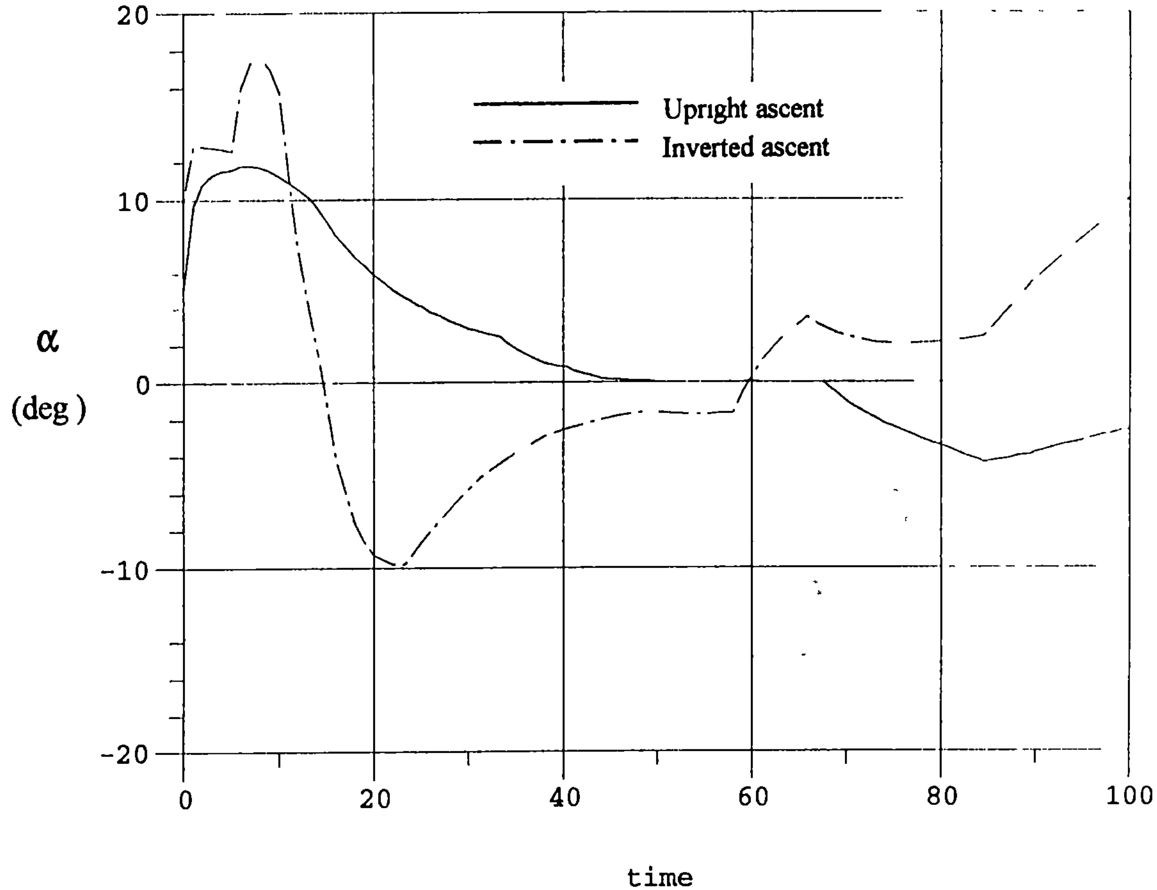

Figure 4 3 Angle of attack during boost phase of upright and inverted ascent

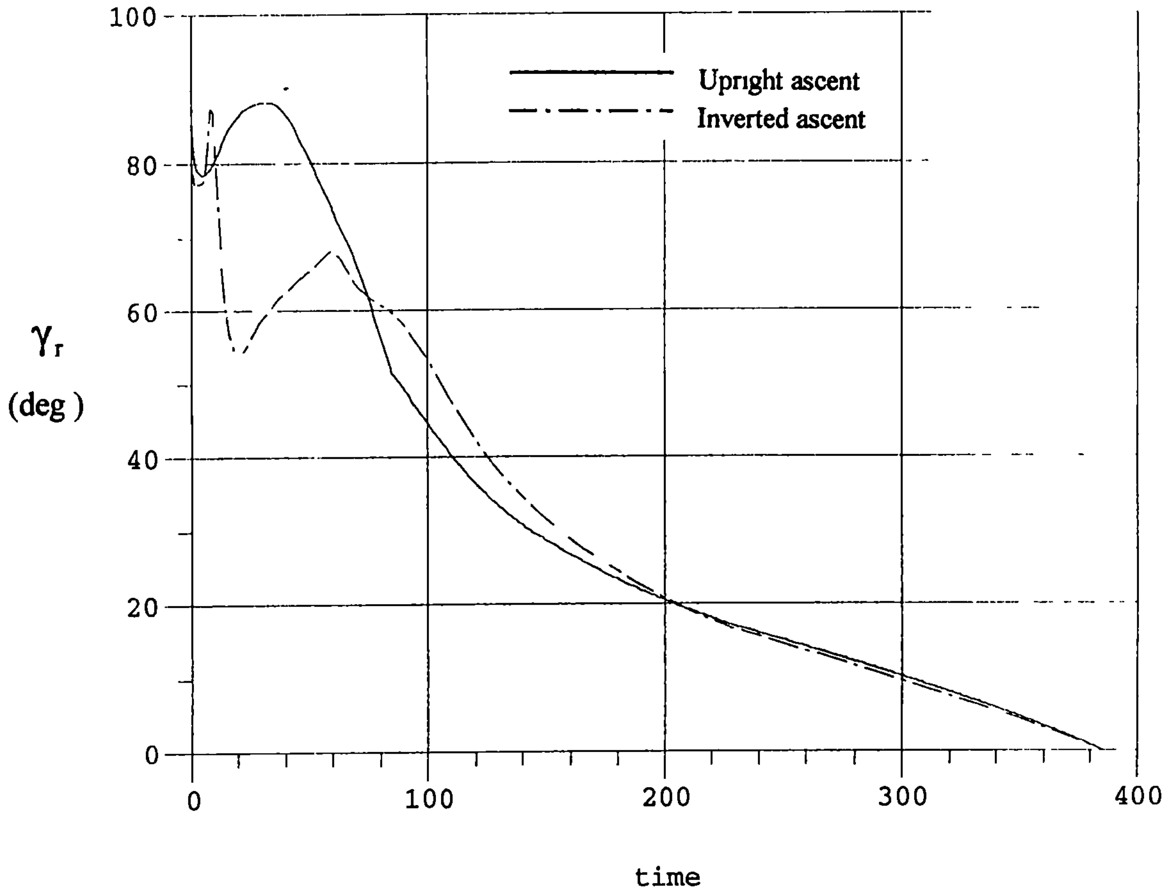

Figure 4.2 : Flight path angle during upright and inverted ascent

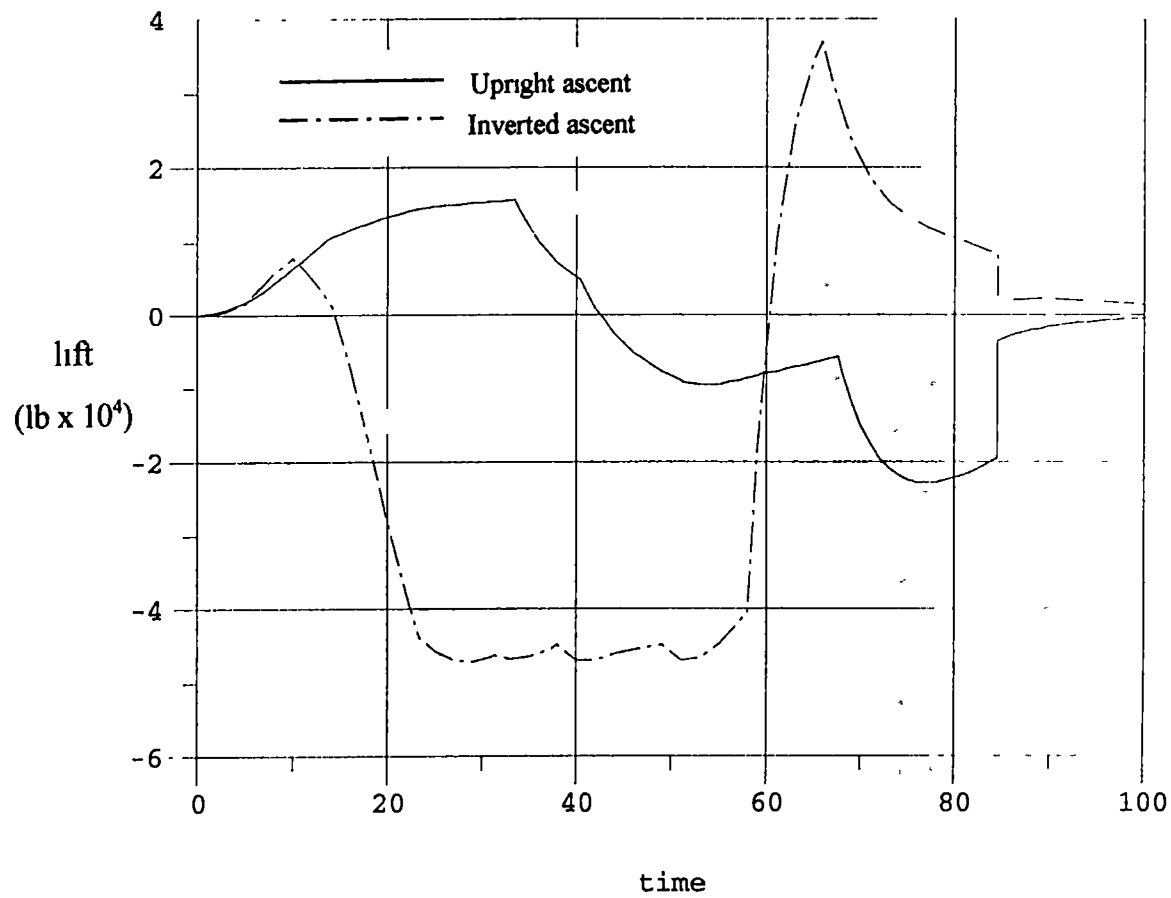

Figure 4.4 : Lift generated during upright and inverted ascent

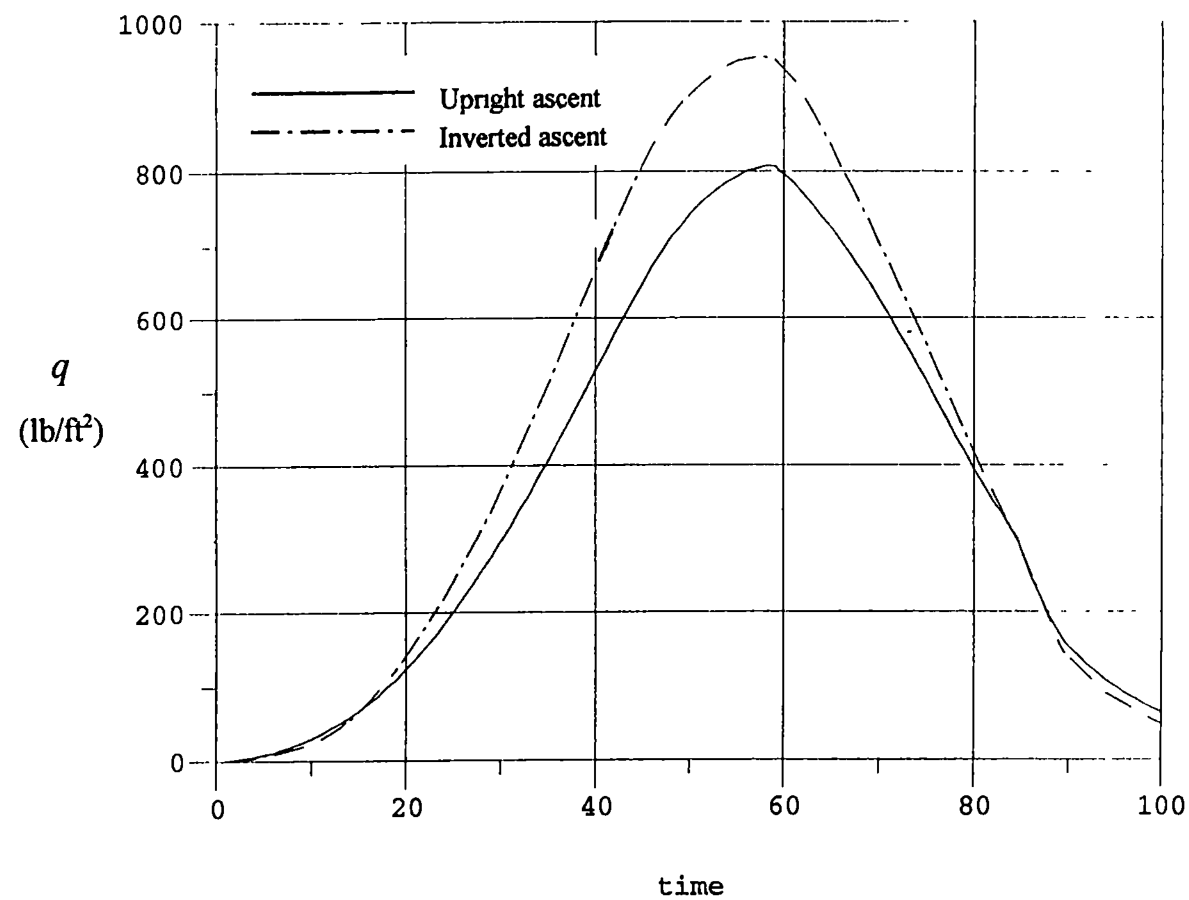

Figure 4 5 : Dynamic pressure during boost phase of upright and inverted ascent

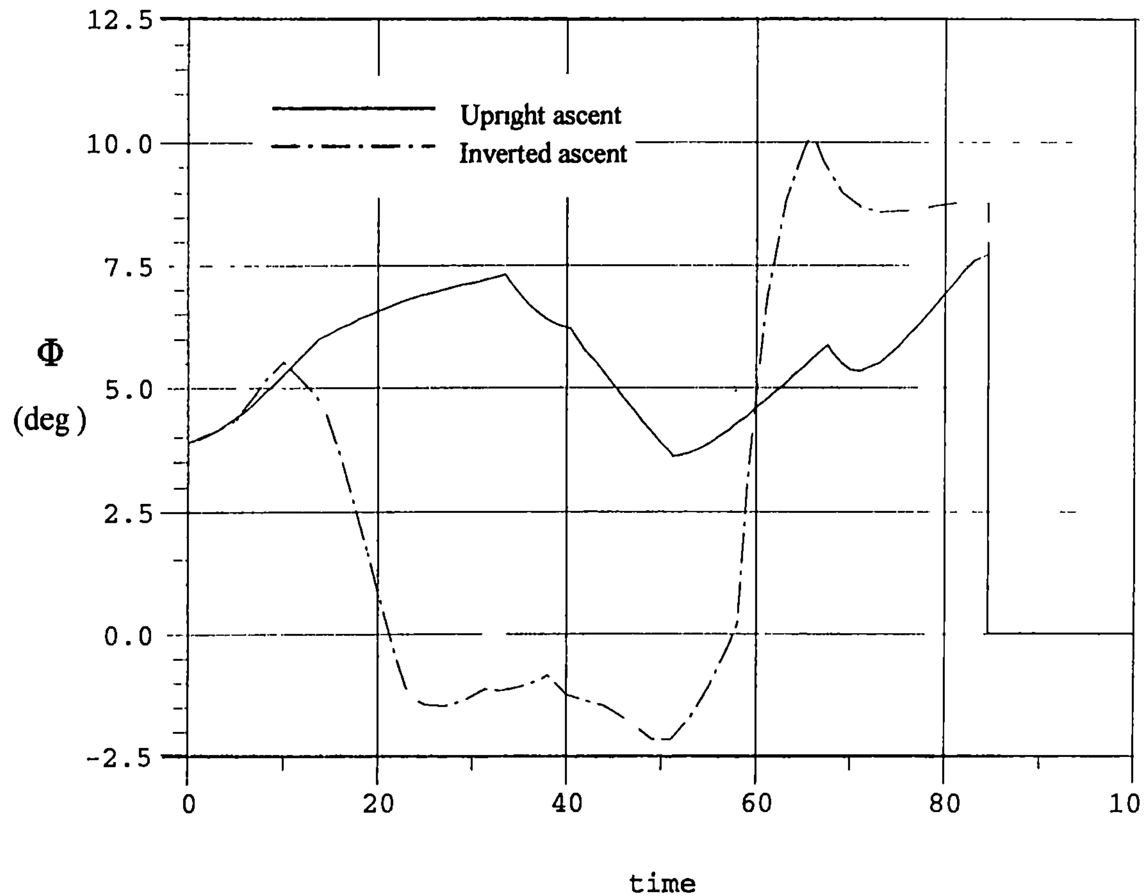

Figure 4.6 : Gimbal angle required to maintain static trim during upright and inverted ascent

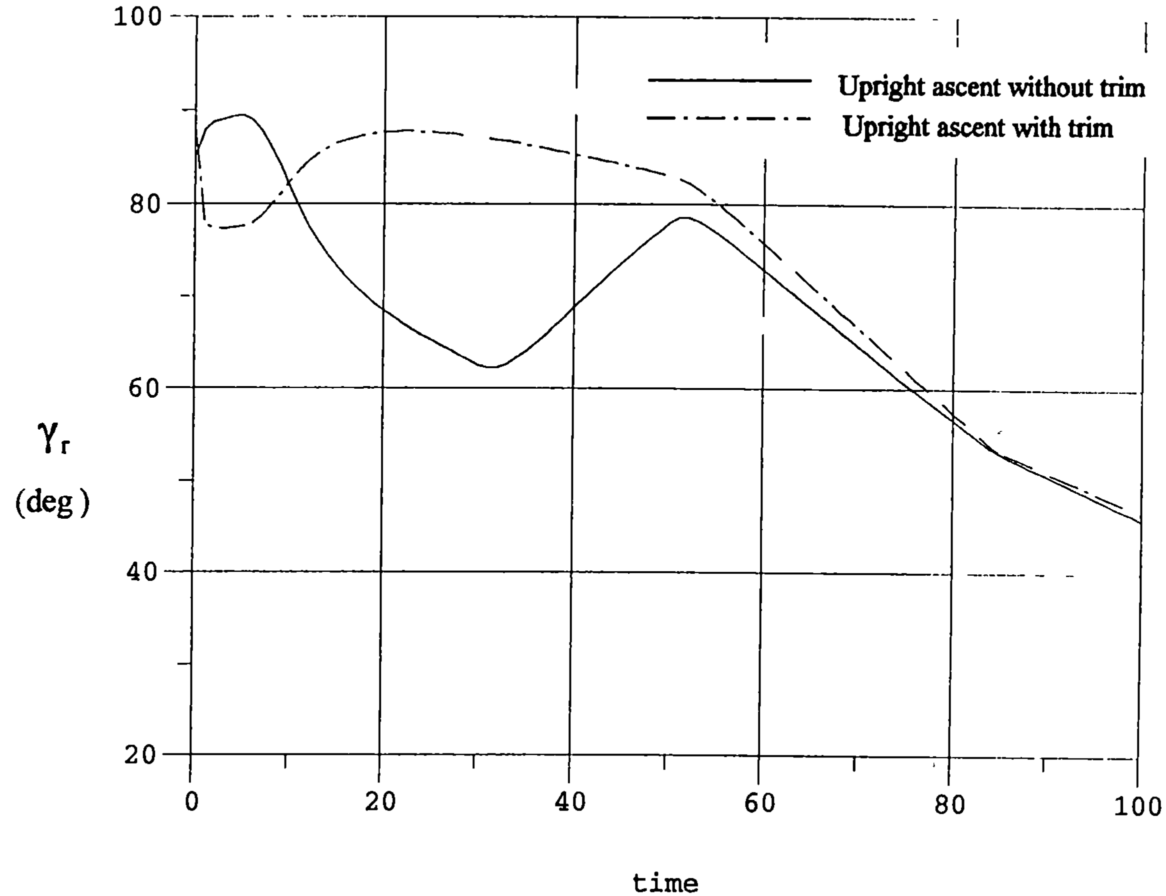

Figure 4.7 : Flight path angle during untrimmed and trimmed upright ascent

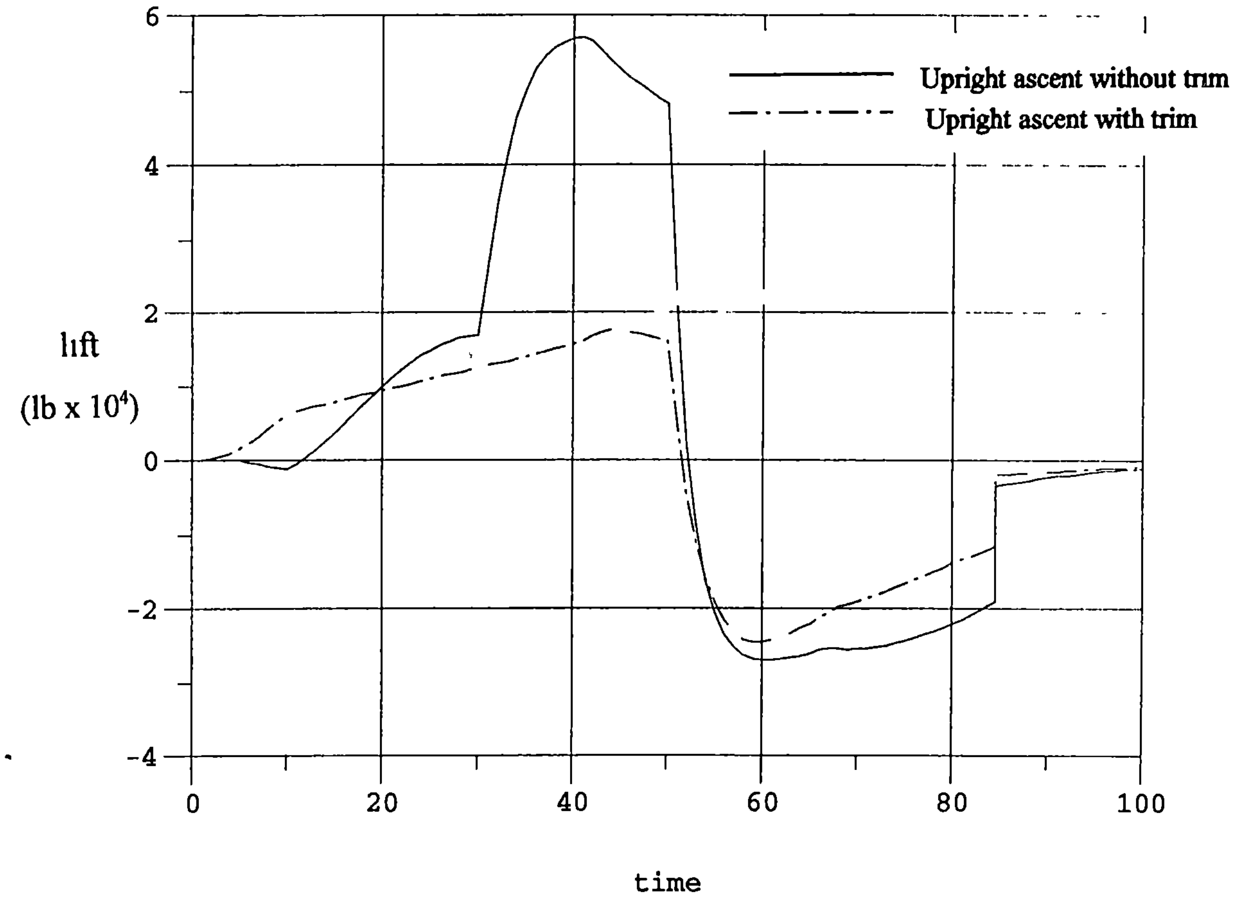

Figure 4.8 : Lift generated during untrimmed and trimmed upright ascent

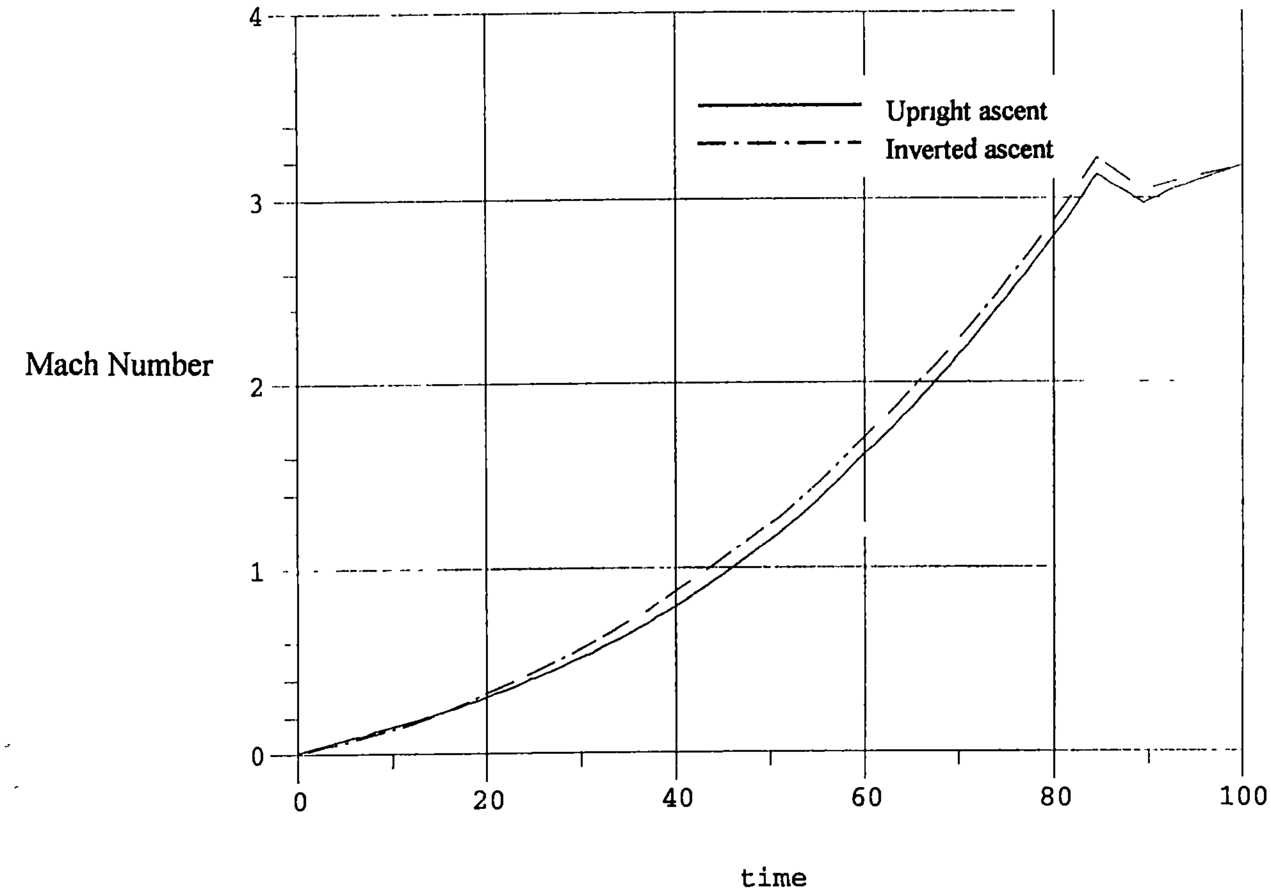

Figure 4.9 : Comparison of Mach number attained at separation point of upright and inverted ascent

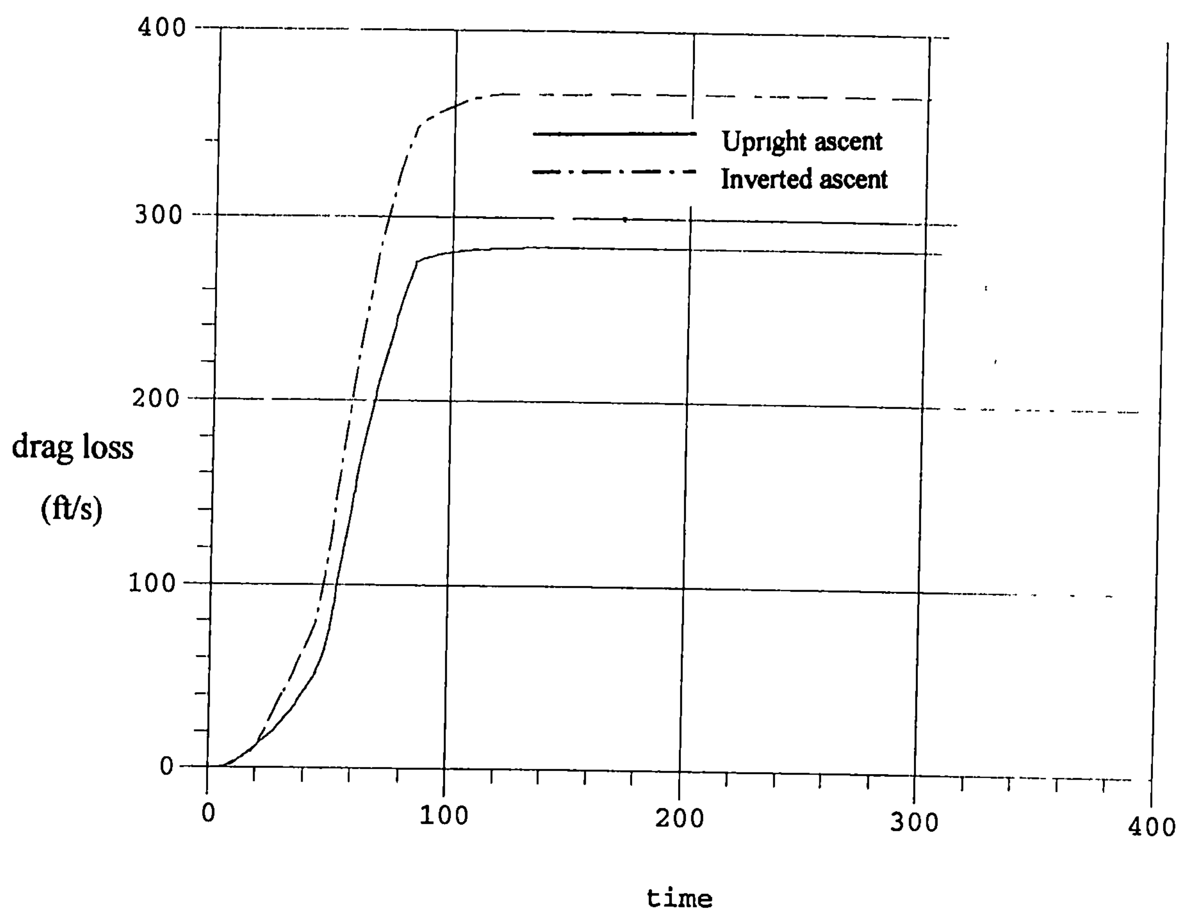

Figure 4.10 : Drag losses of upright and inverted ascent

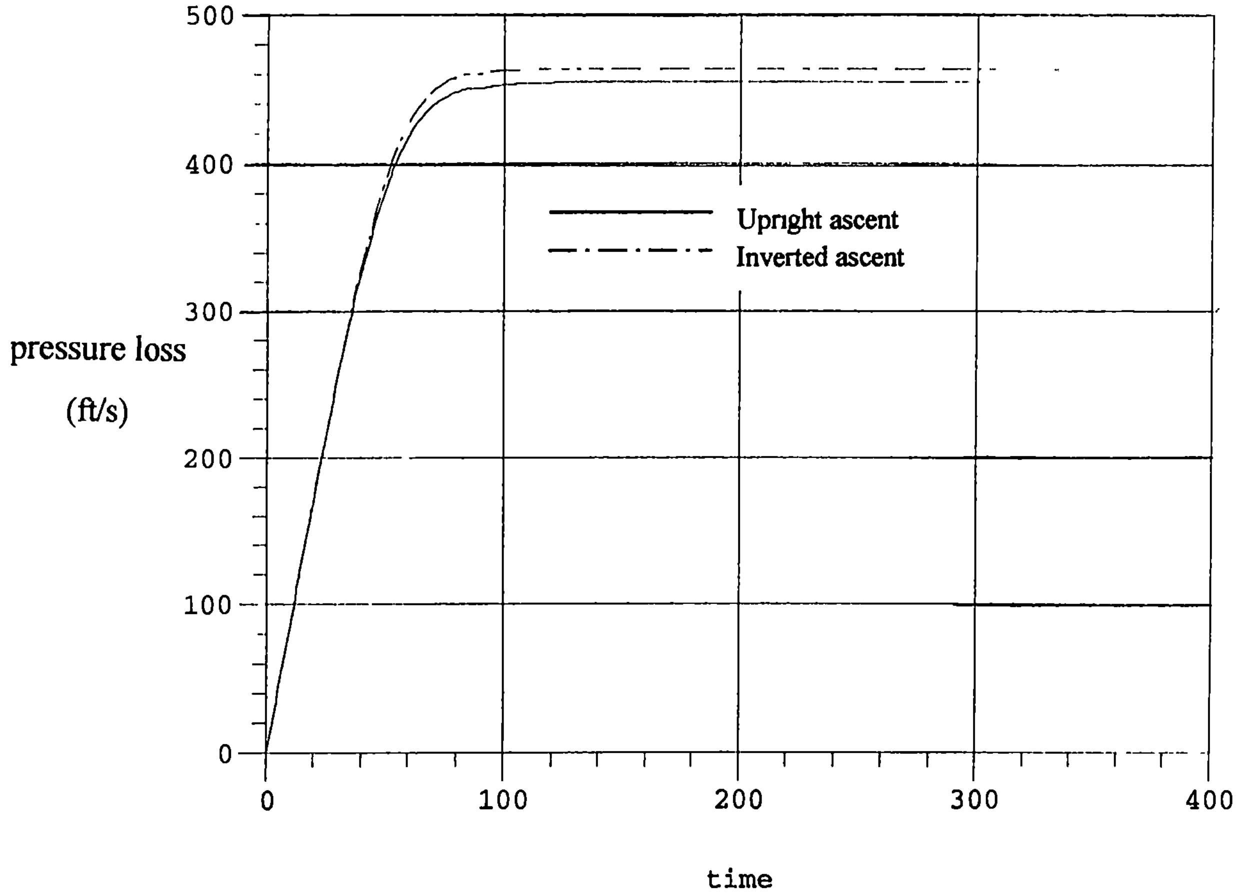

Figure 4.11 : Atmospheric losses of upright and inverted ascent

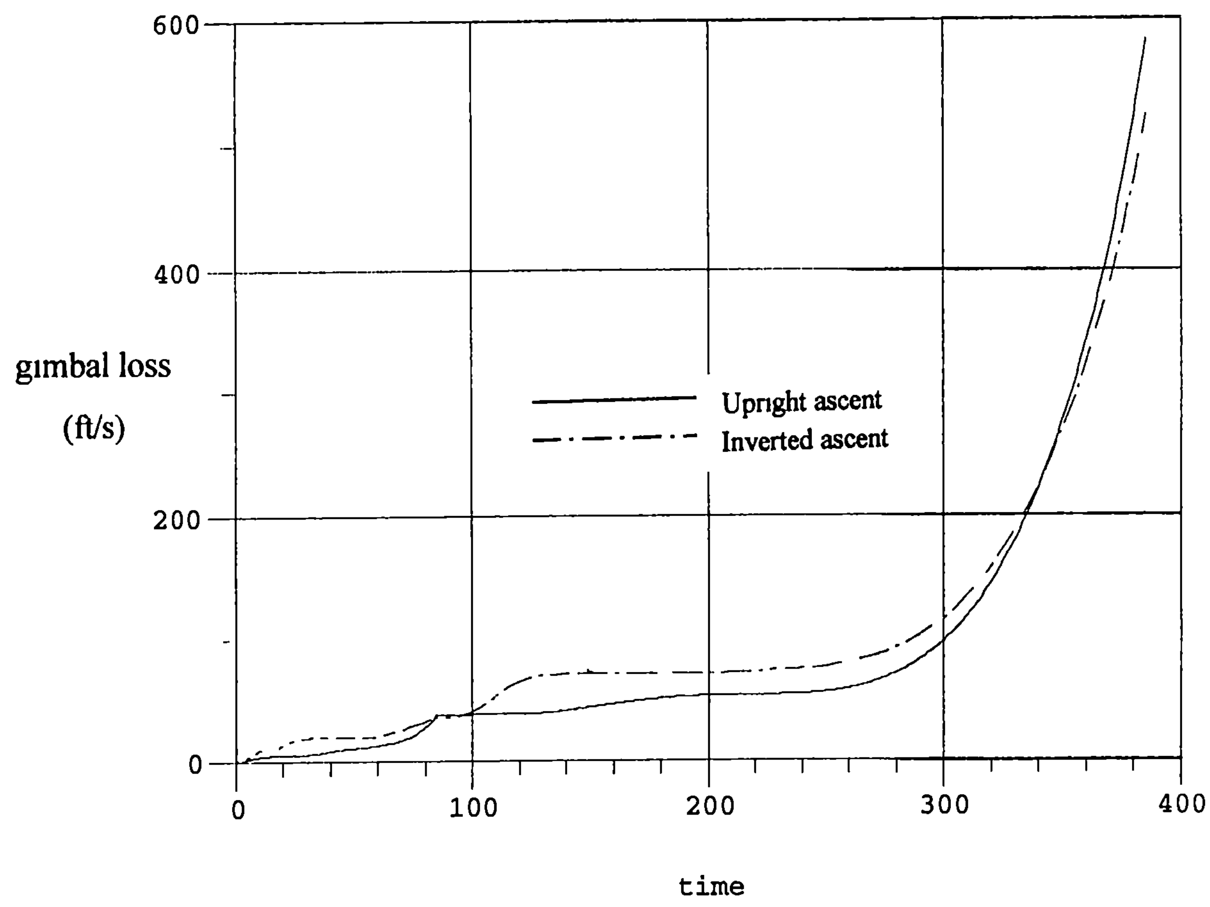

Figure 4.12 : Thrust vectoring losses resulting from engine gimbal during upright and inverted ascent

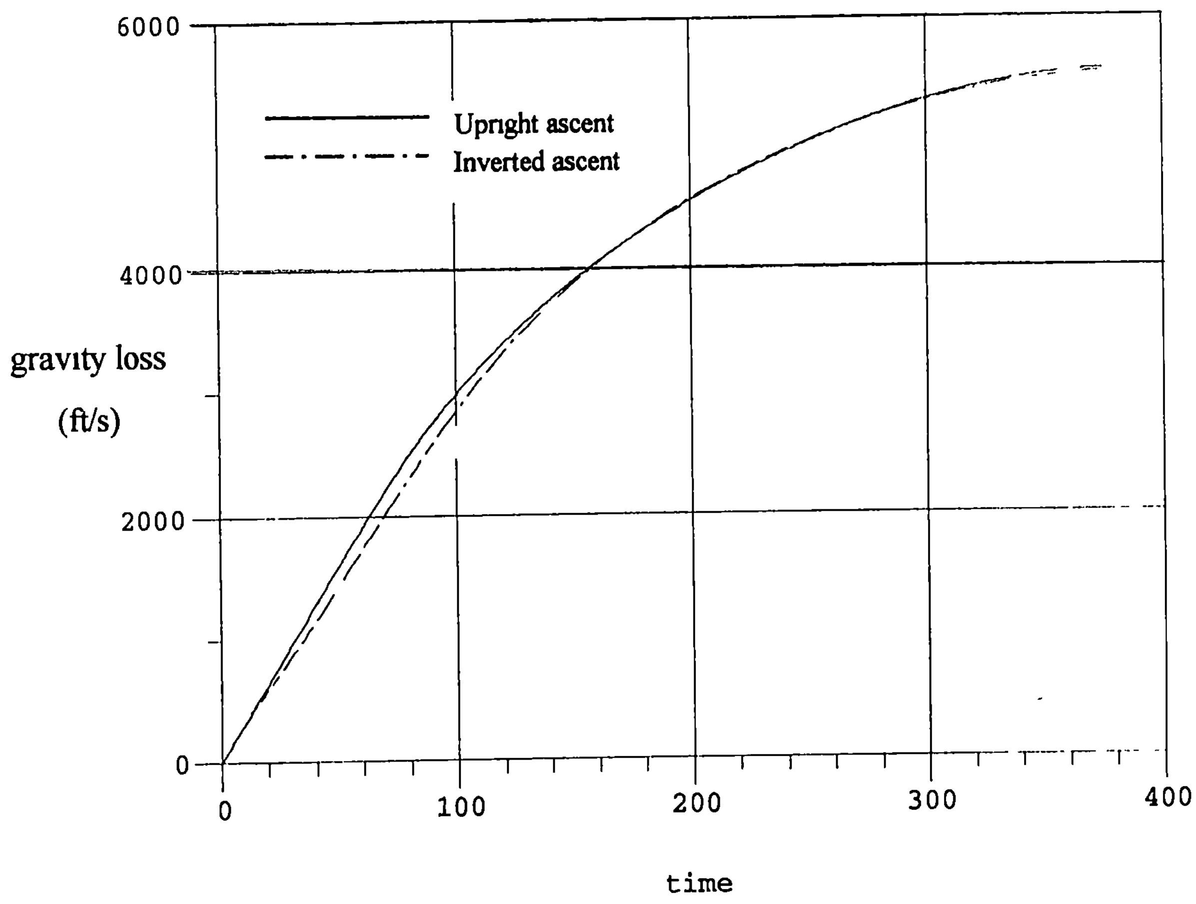

Figure 4.13 : Gravity losses of upright and inverted ascent

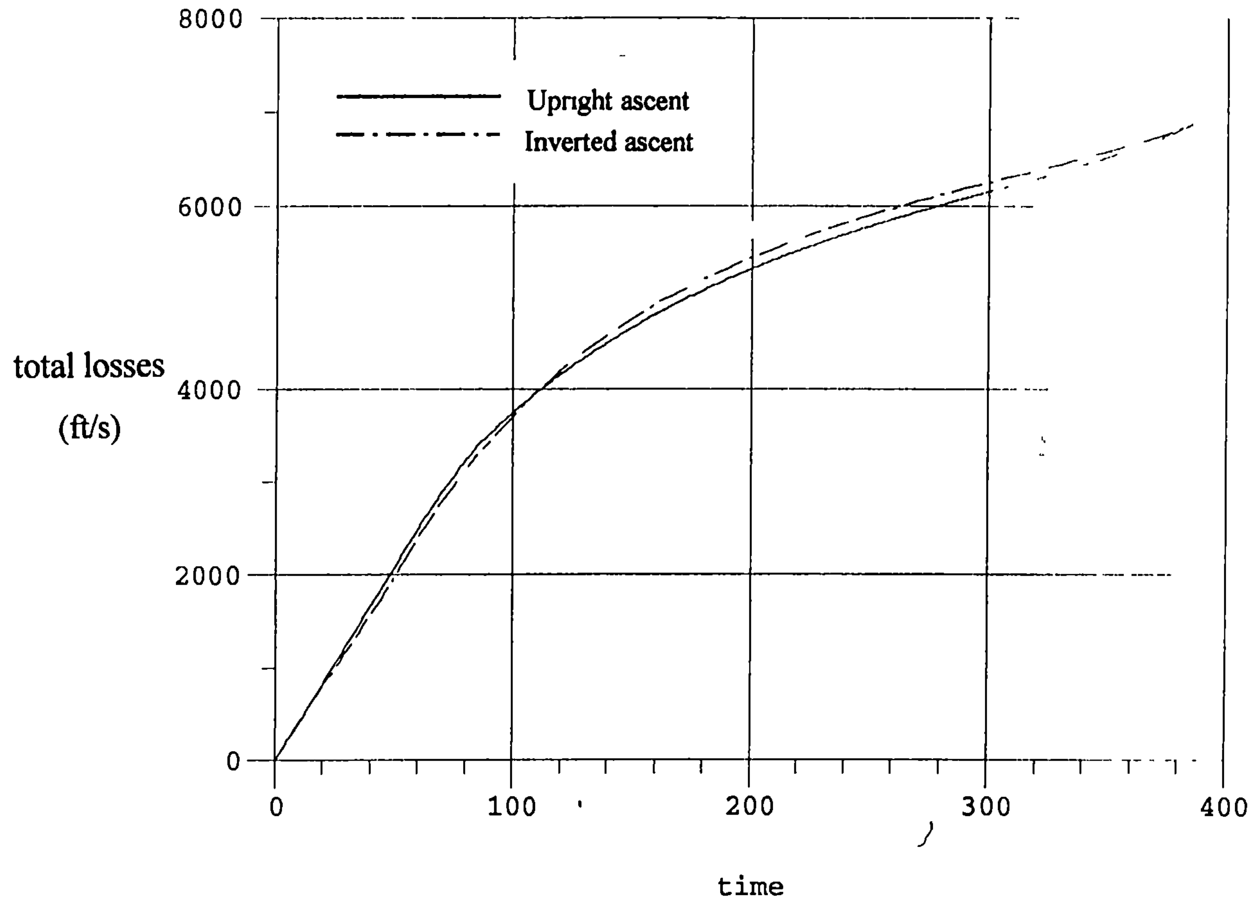

Figure 4.14 : Sum of all losses during upright and inverted ascent

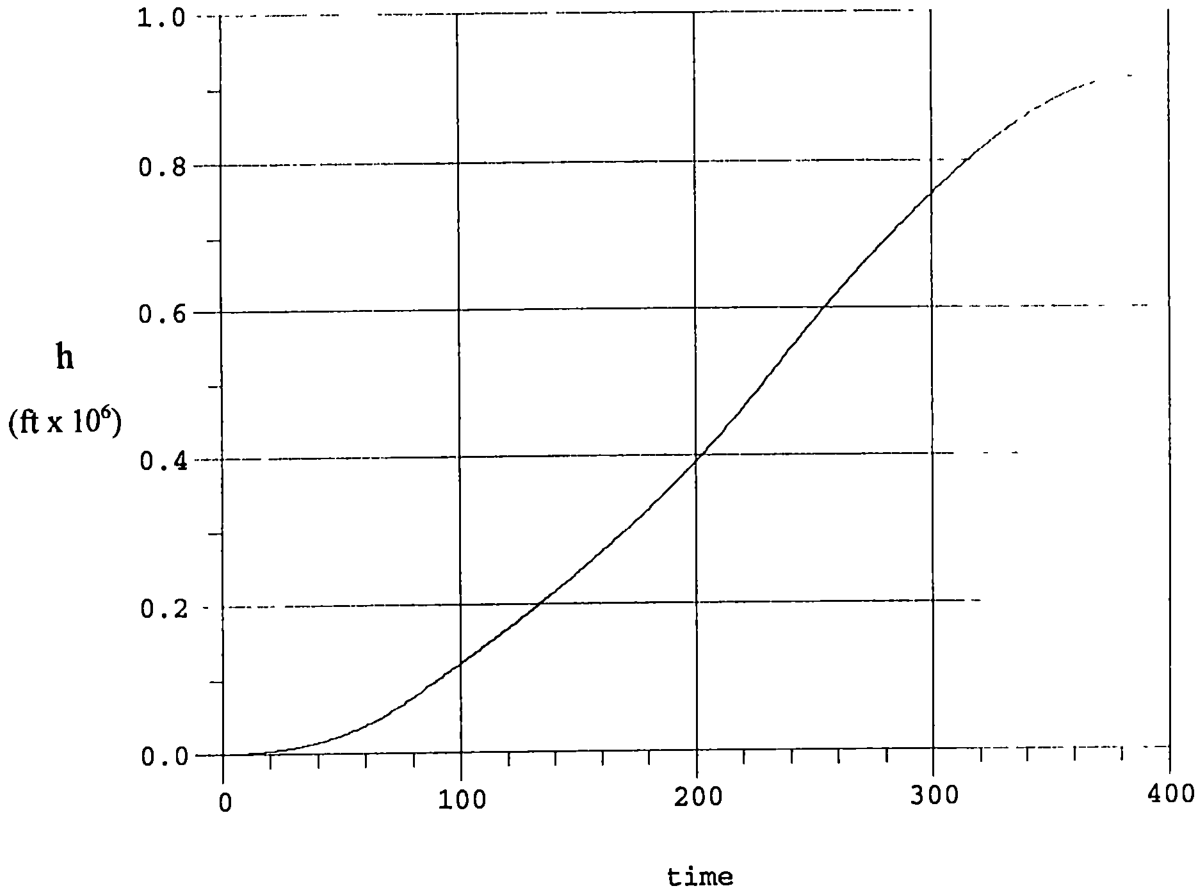

Figure 4.15 . Altitude profile of optimal upright ascent

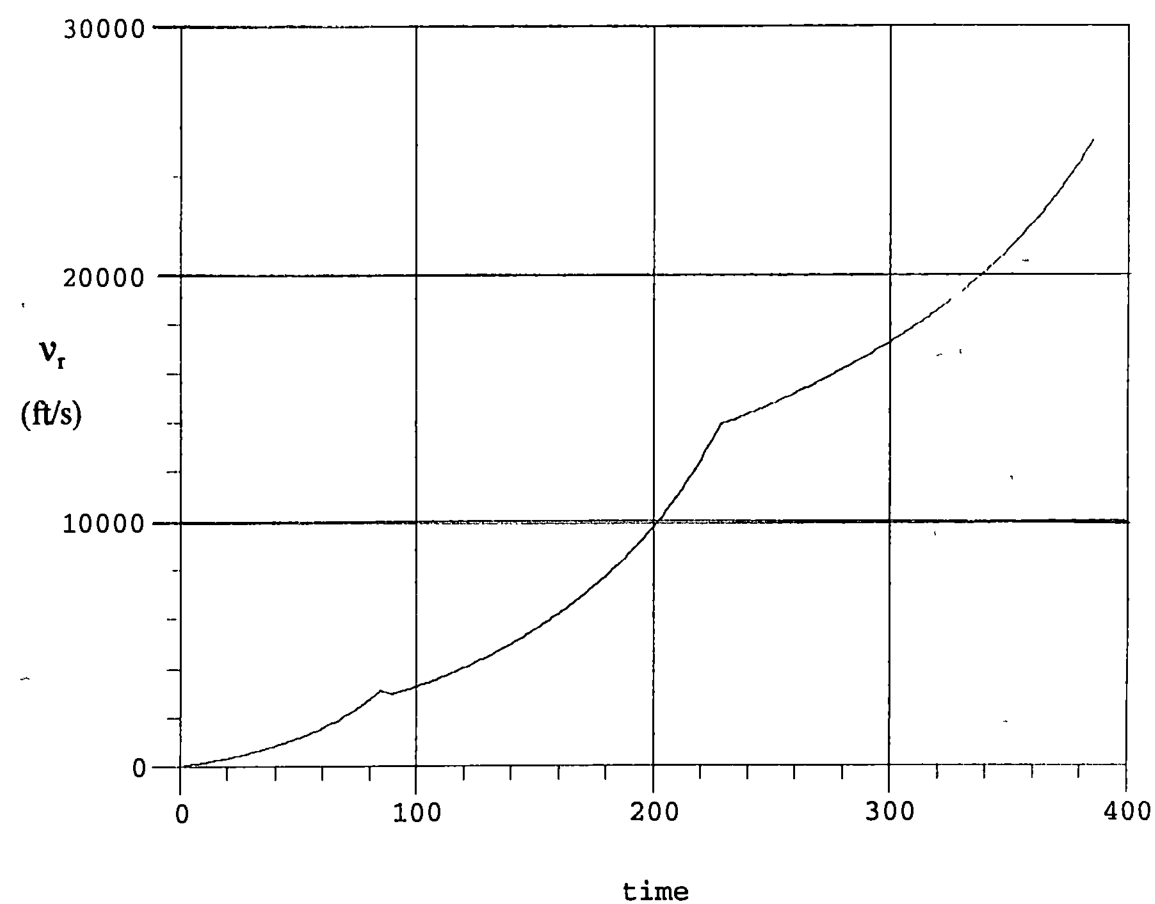

Figure 4 16 . Relative velocity profile of upright ascent

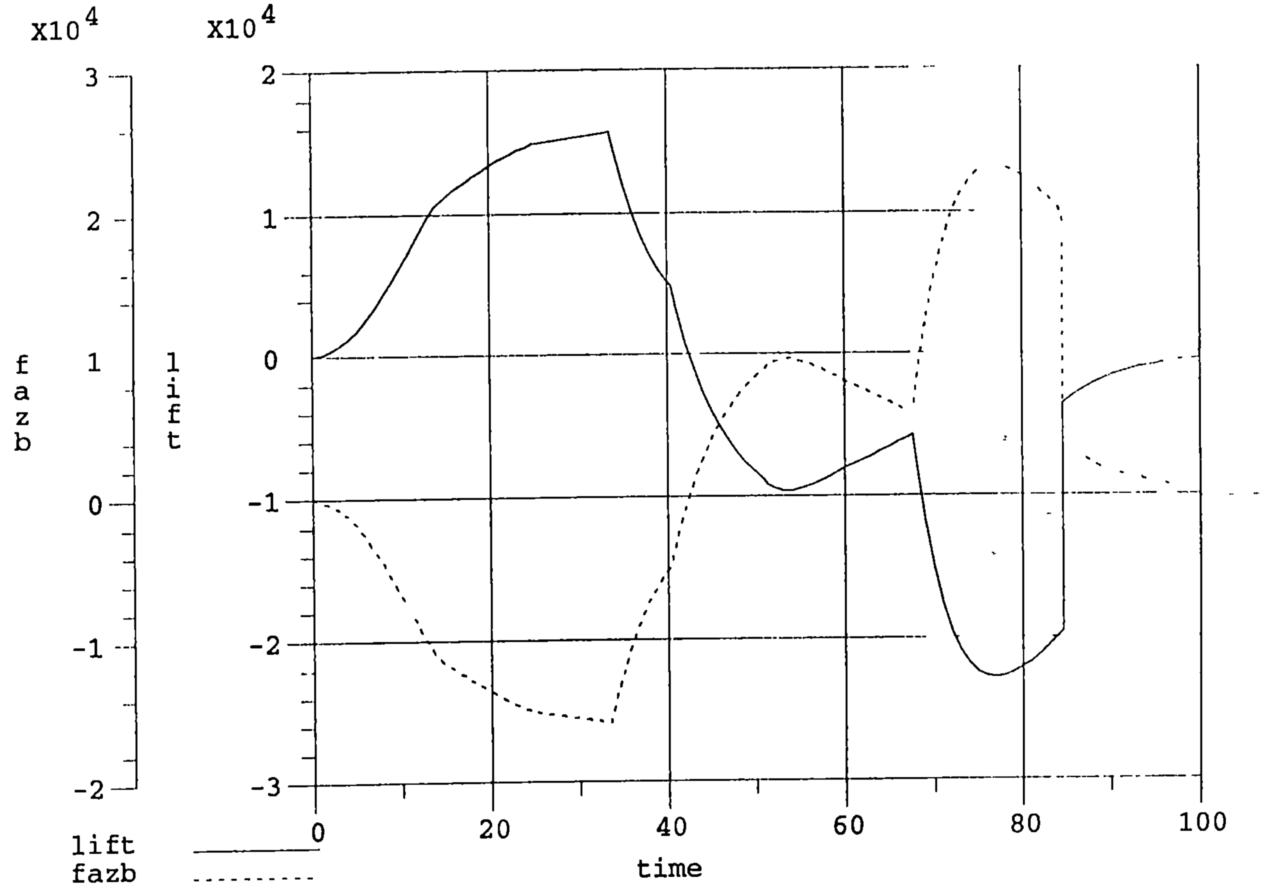

Figure 4 17 · Lift and normal force during boost phase of upright ascent

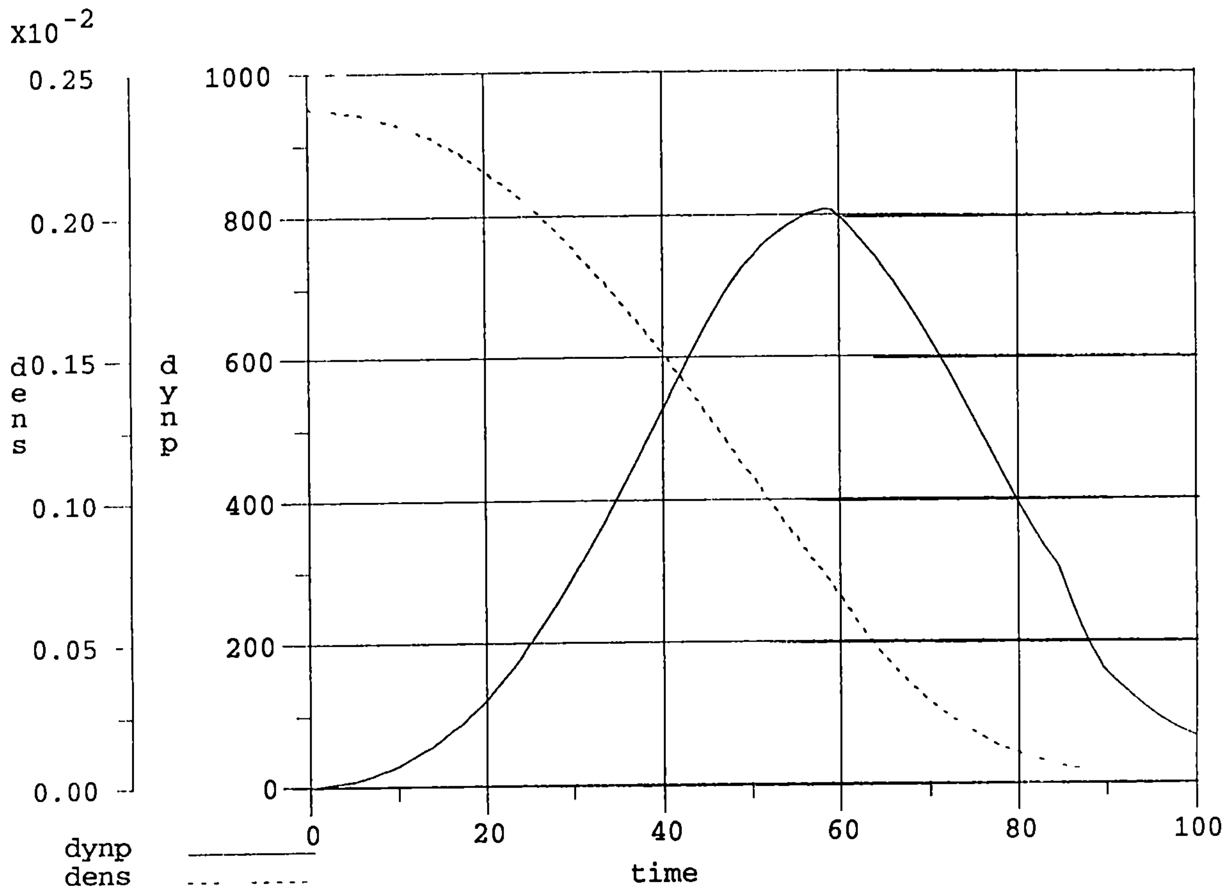

Figure 4 18 · Atmospheric density and dynamic pressure during boost phase of upright ascent

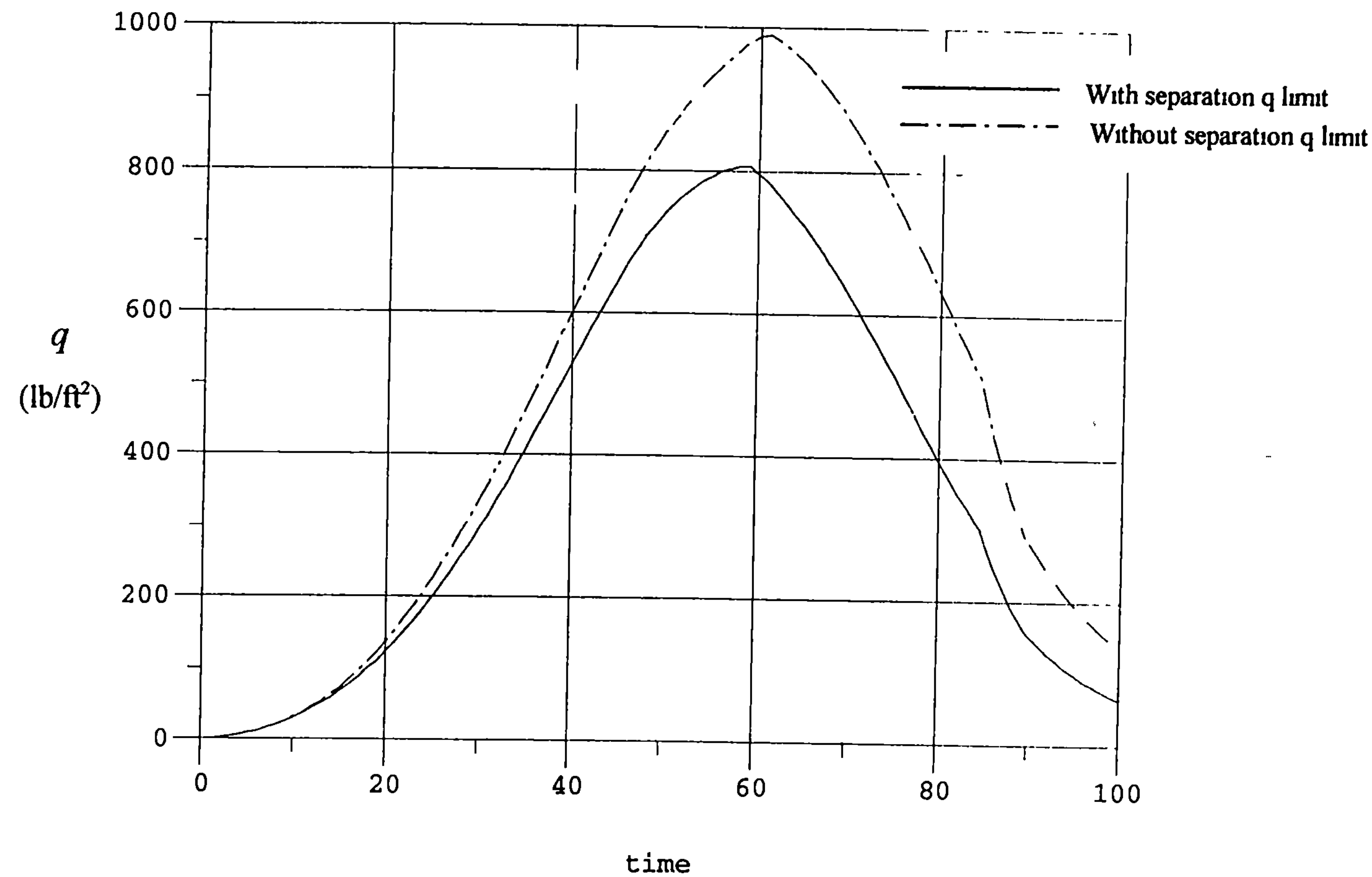

Figure 4 19 Comparison of boost phase dynamic pressure with and without dynamic pressure constraint at separation

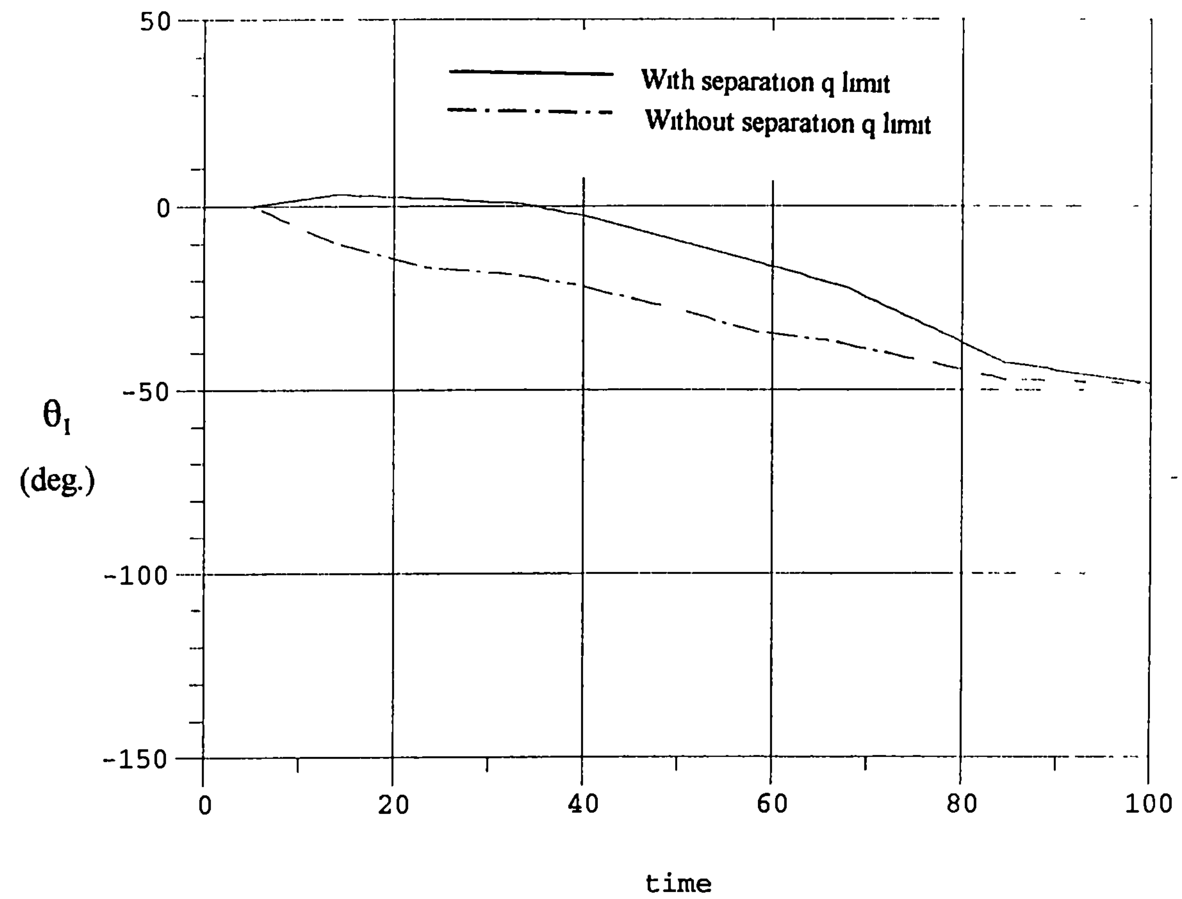

Figure 4 20 Comparison of pitch angle during boost phase of ascent with and without dynamic pressure constraint at separation

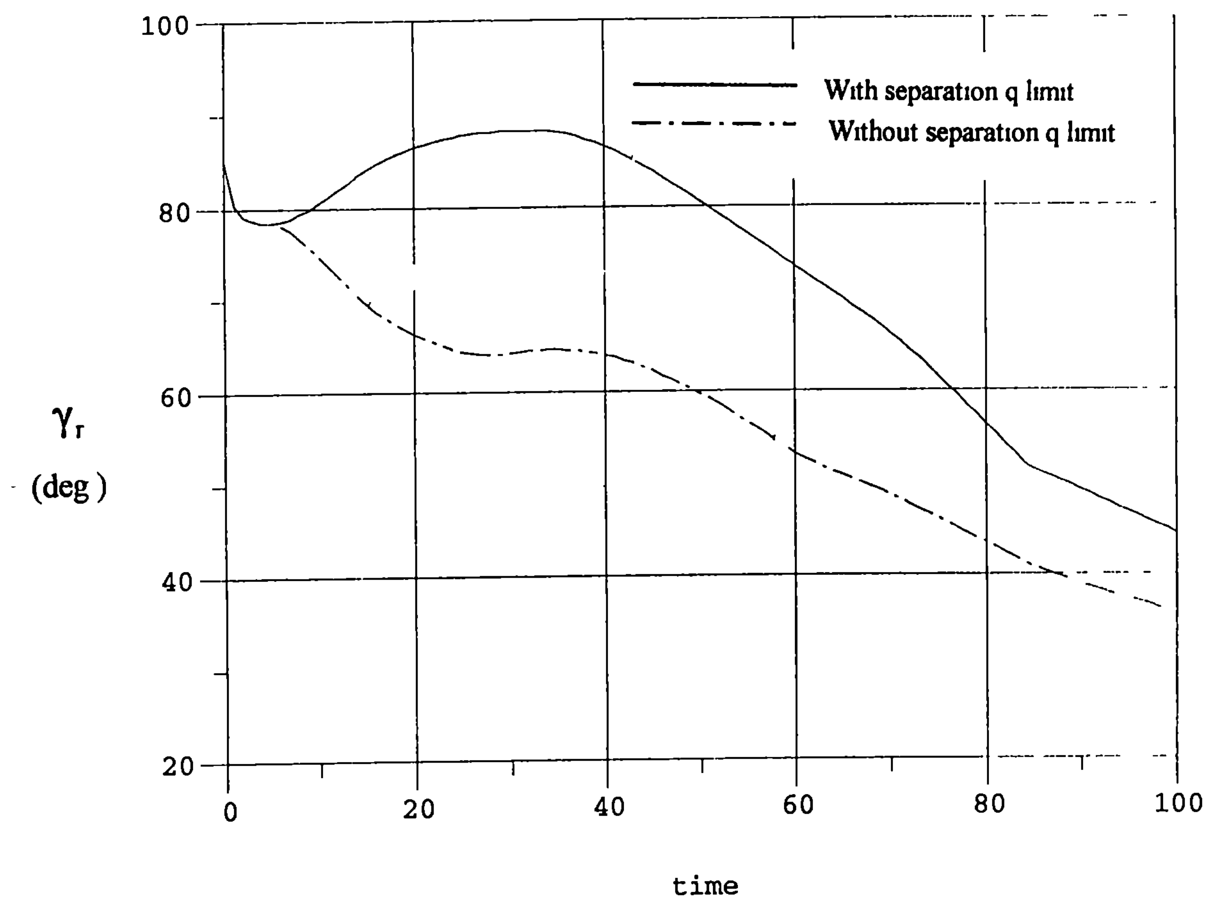

Figure 4 21 Comparison of relative flight path angle during boost phase of ascent with and without dynamic pressure constraint at separation

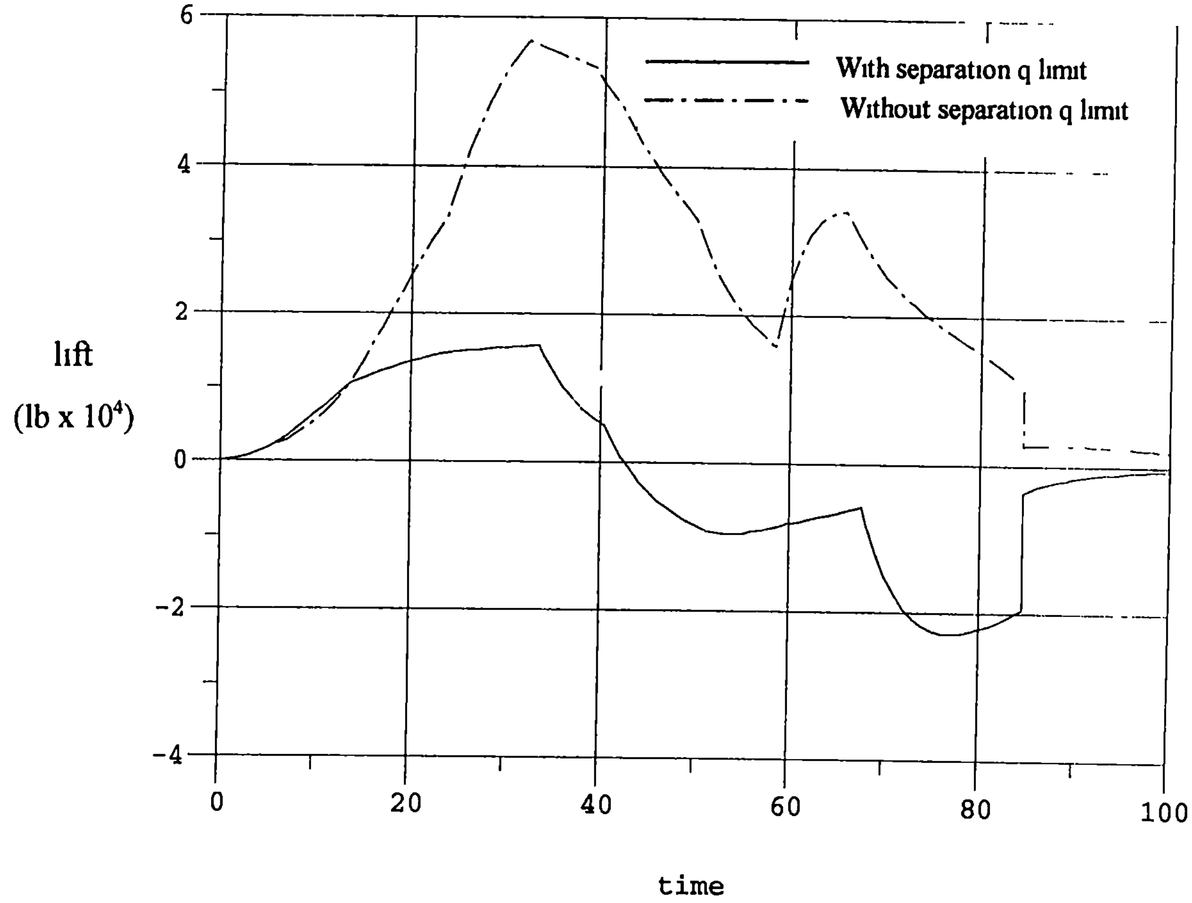

Figure 4 22 · Comparison of lift during boost phase of ascent with and without dynamic pressure constraint at separation

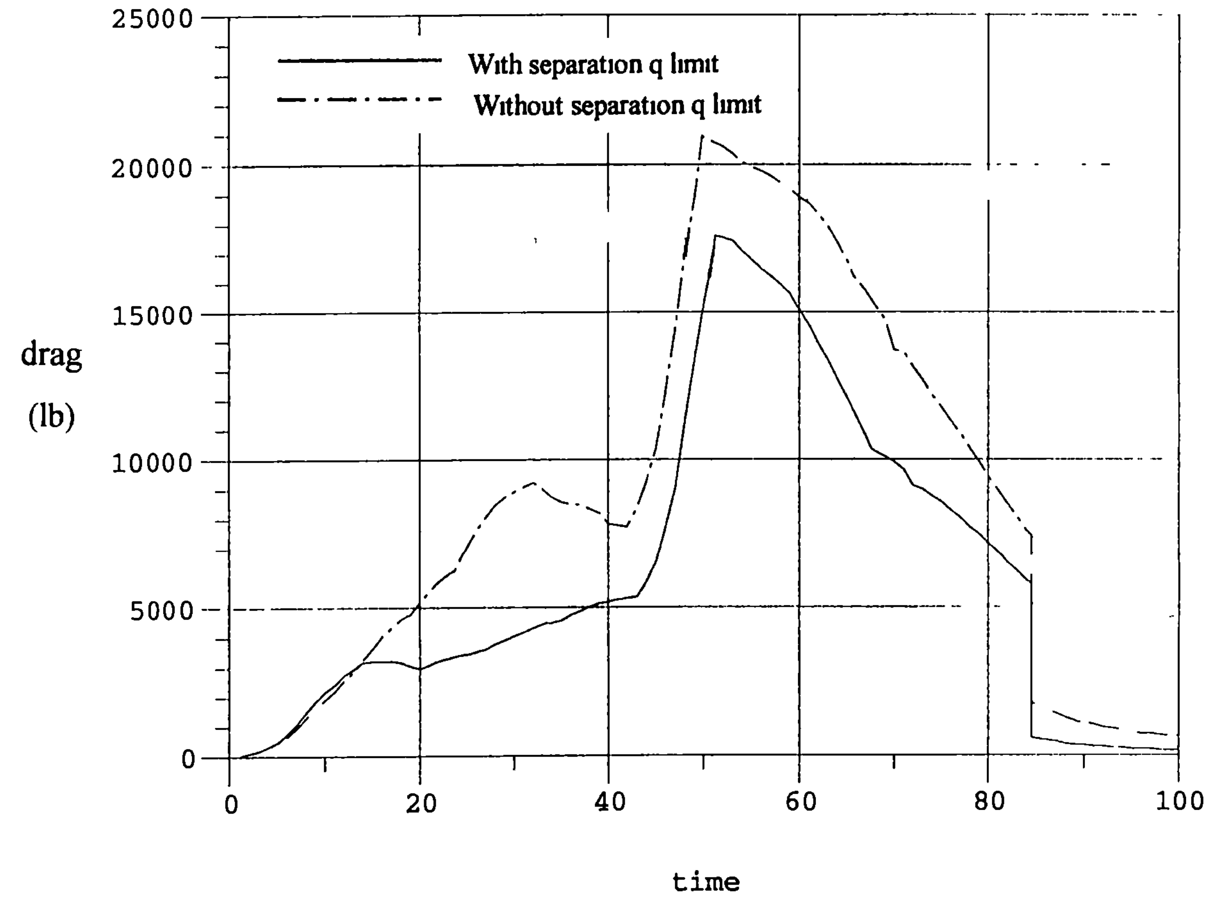

Figure 4 23 Comparison of drag during boost phase of ascent with and without dynamic pressure constraint at separation

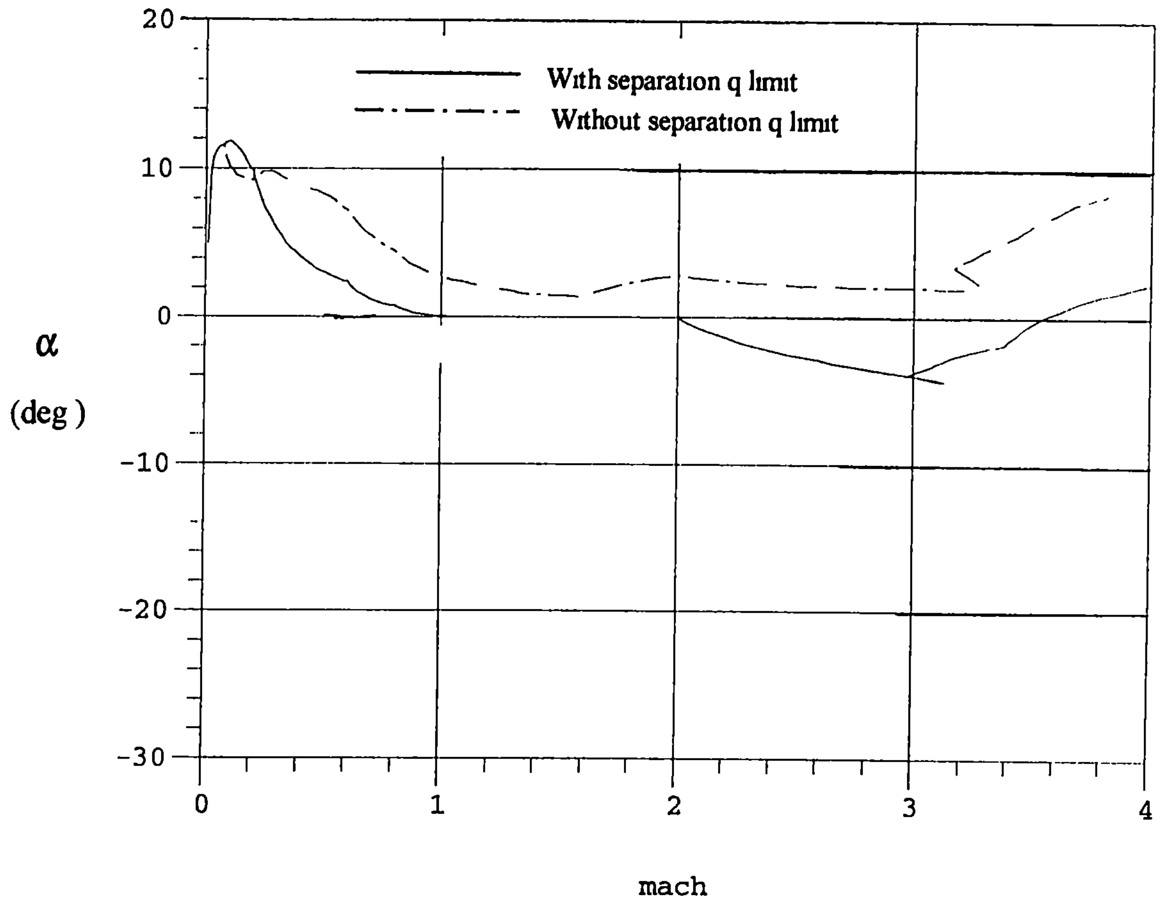

Figure 4 24 Upright ascent boost phase angle of attack as a function of Mach number with and without dynamic pressure constraint at separation

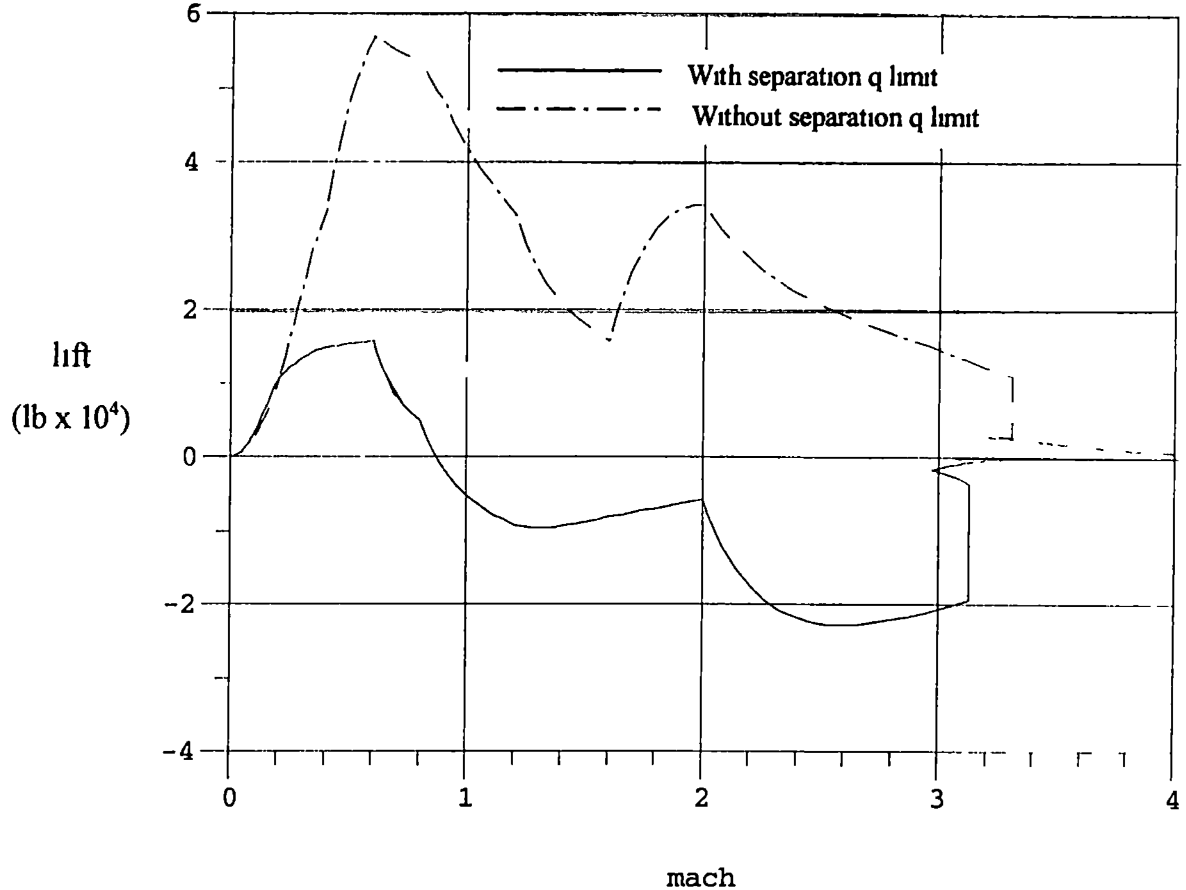

Figure 4 25 : Upright ascent boost phase lift as a function of Mach number with and without dynamic pressure constraint at separation

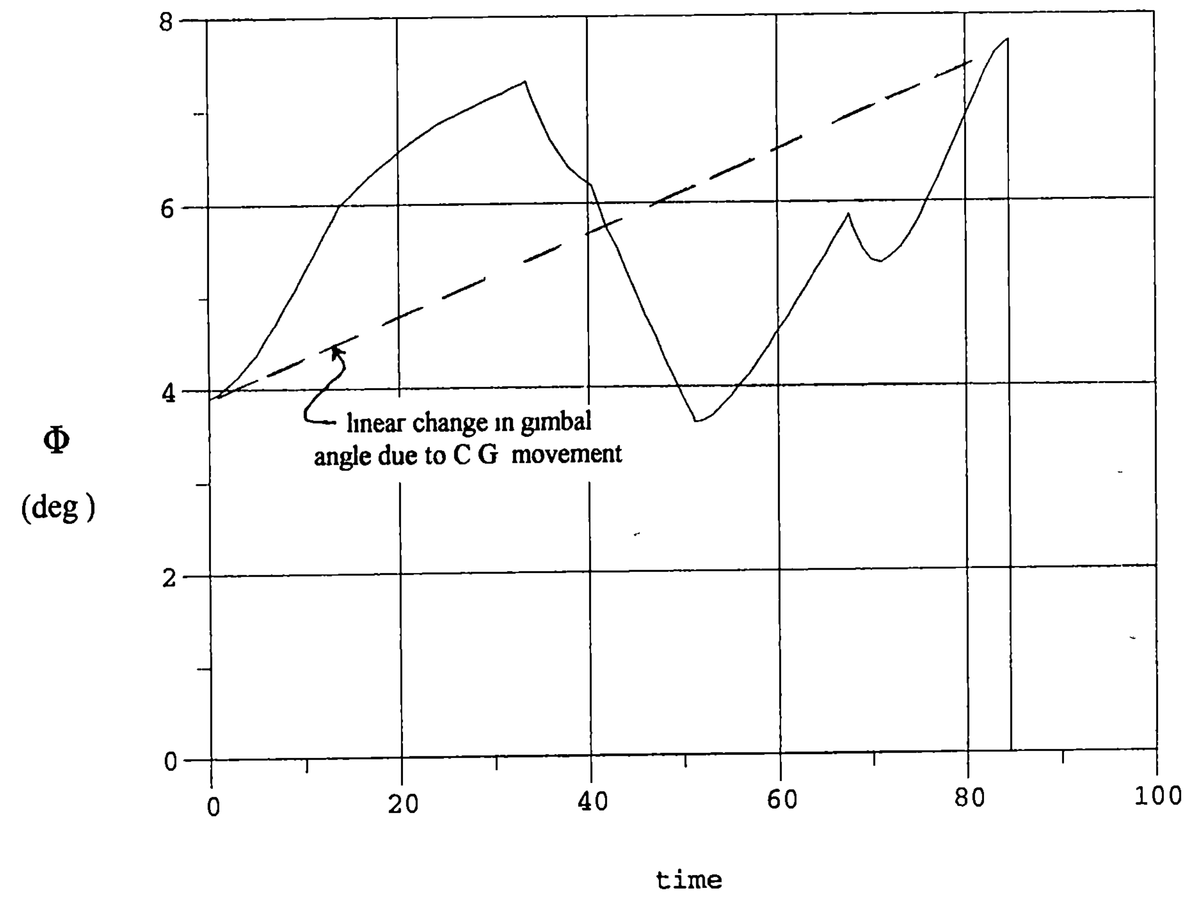

Figure 4 26 Gimbal angle required to maintain static trim during boost phase of upright ascent

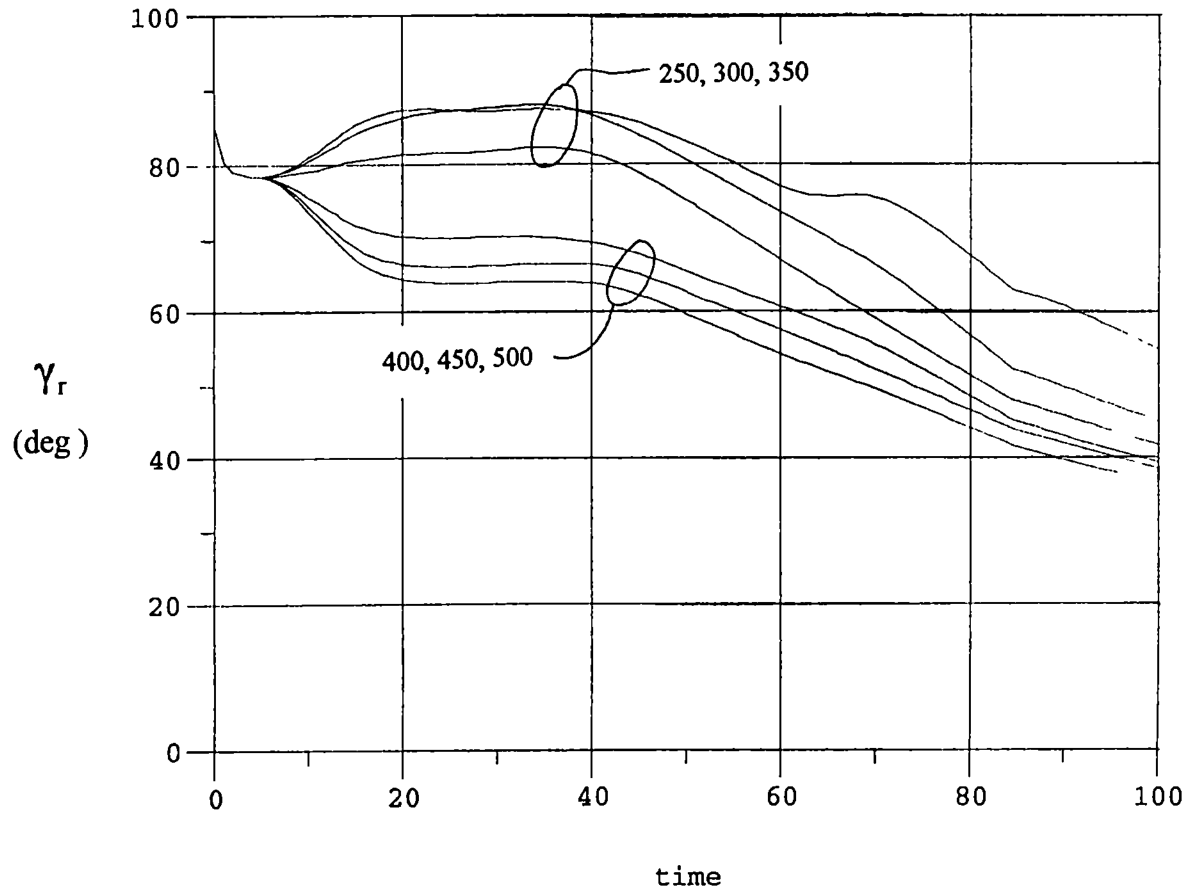

Figure 4.27 : Effect of dynamic pressure at separation constraint on flight path angle up to separation

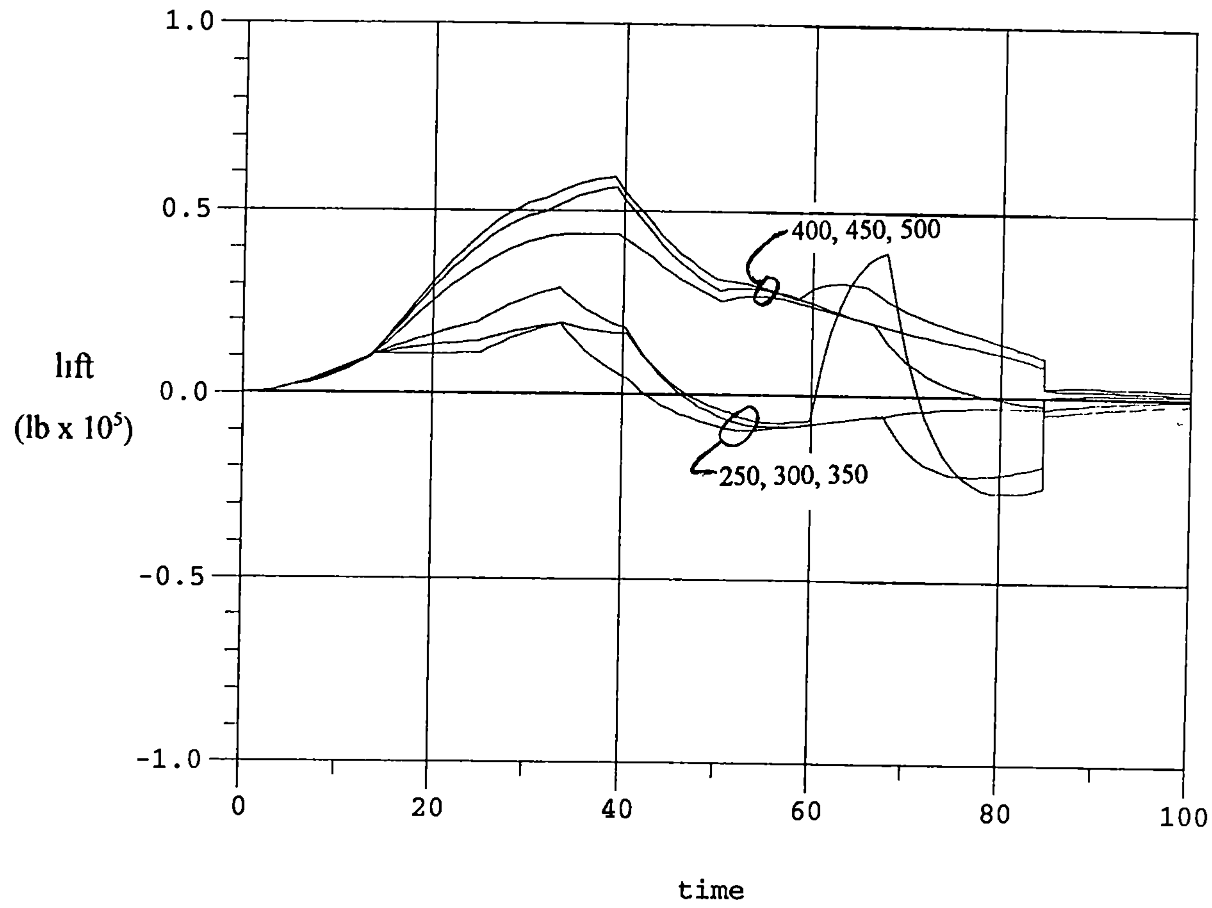

Figure 4.28 : Effect of dynamic pressure at separation constraint on lift generation up to separation

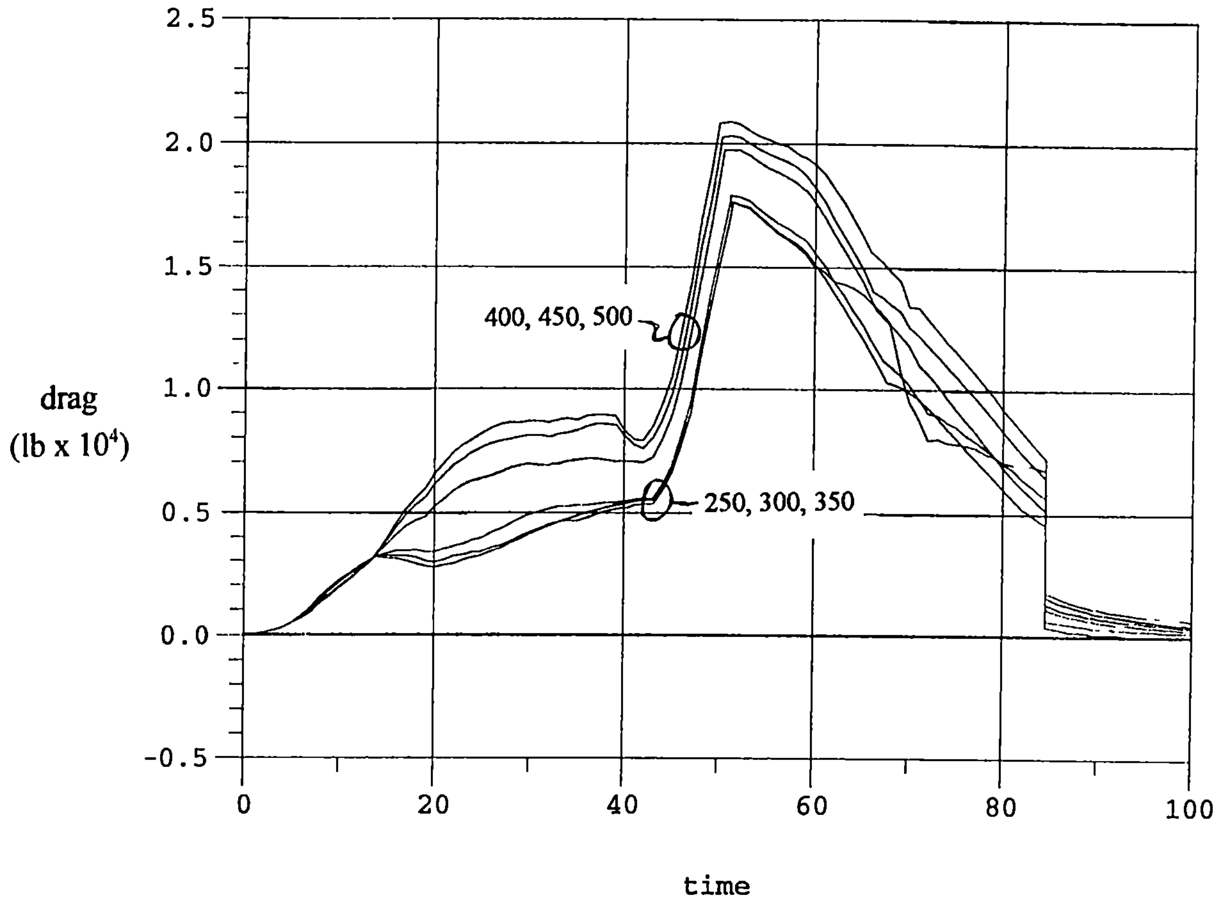

Figure 4 29 · Effect of separation dynamic pressure on boost phase drag

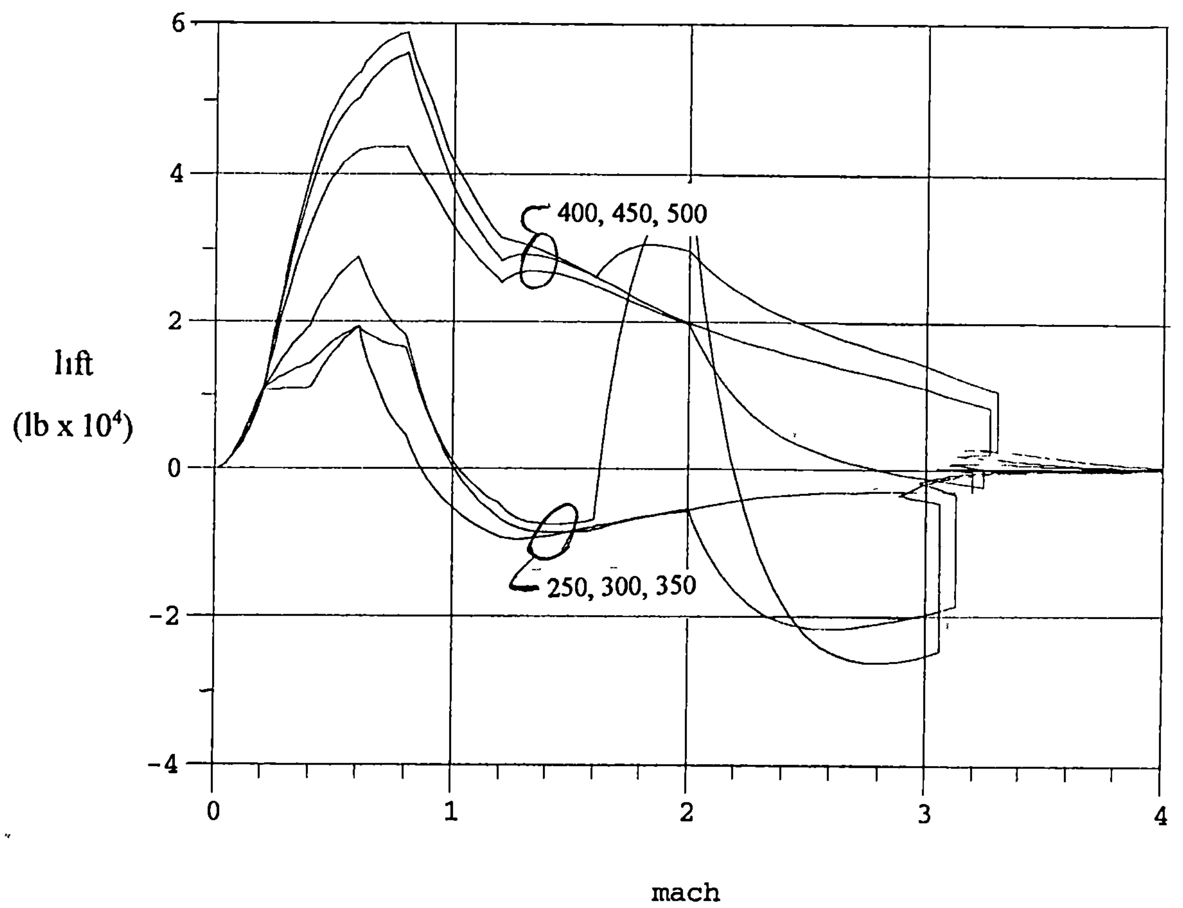

Figure 4 30 . Upright ascent boost phase lift as a function of Mach number

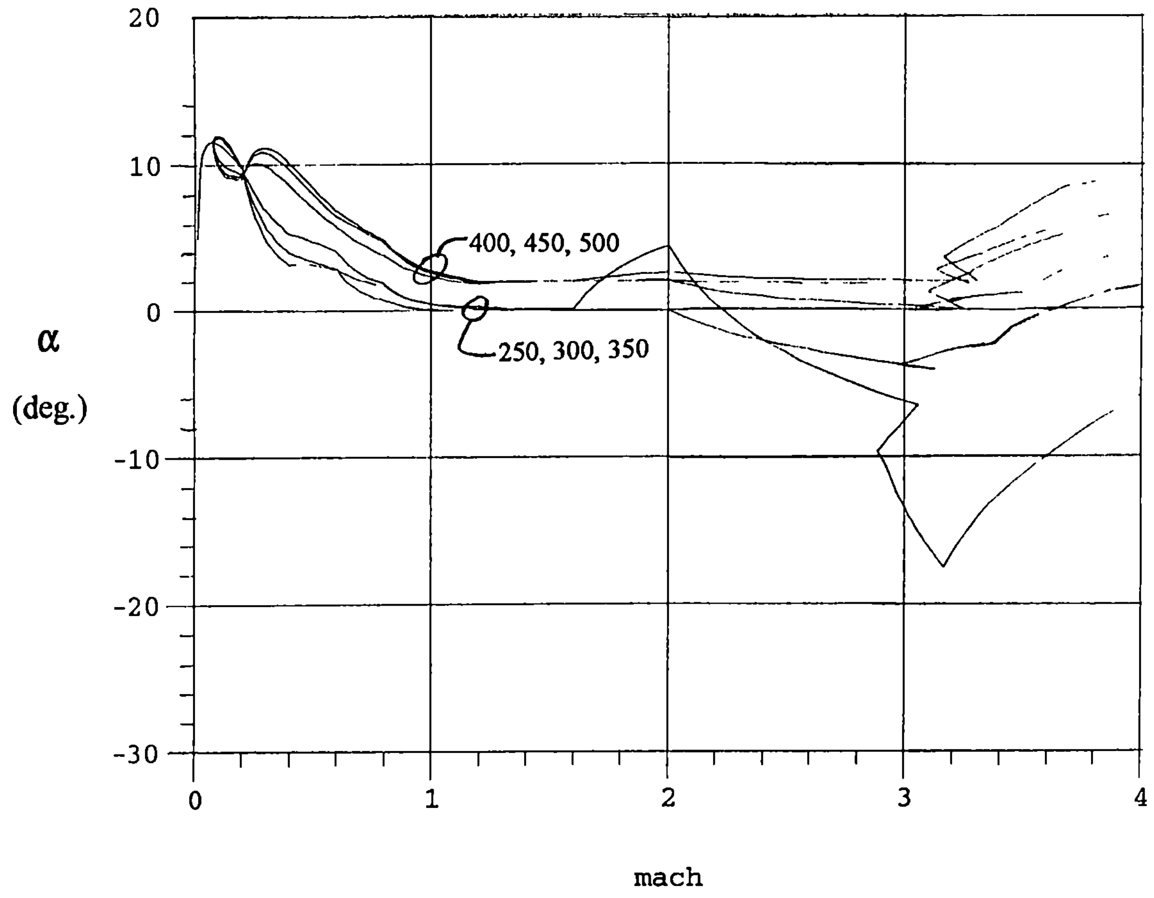

Figure 4 31 Upright ascent boost phase angle of attack as a function of Mach number

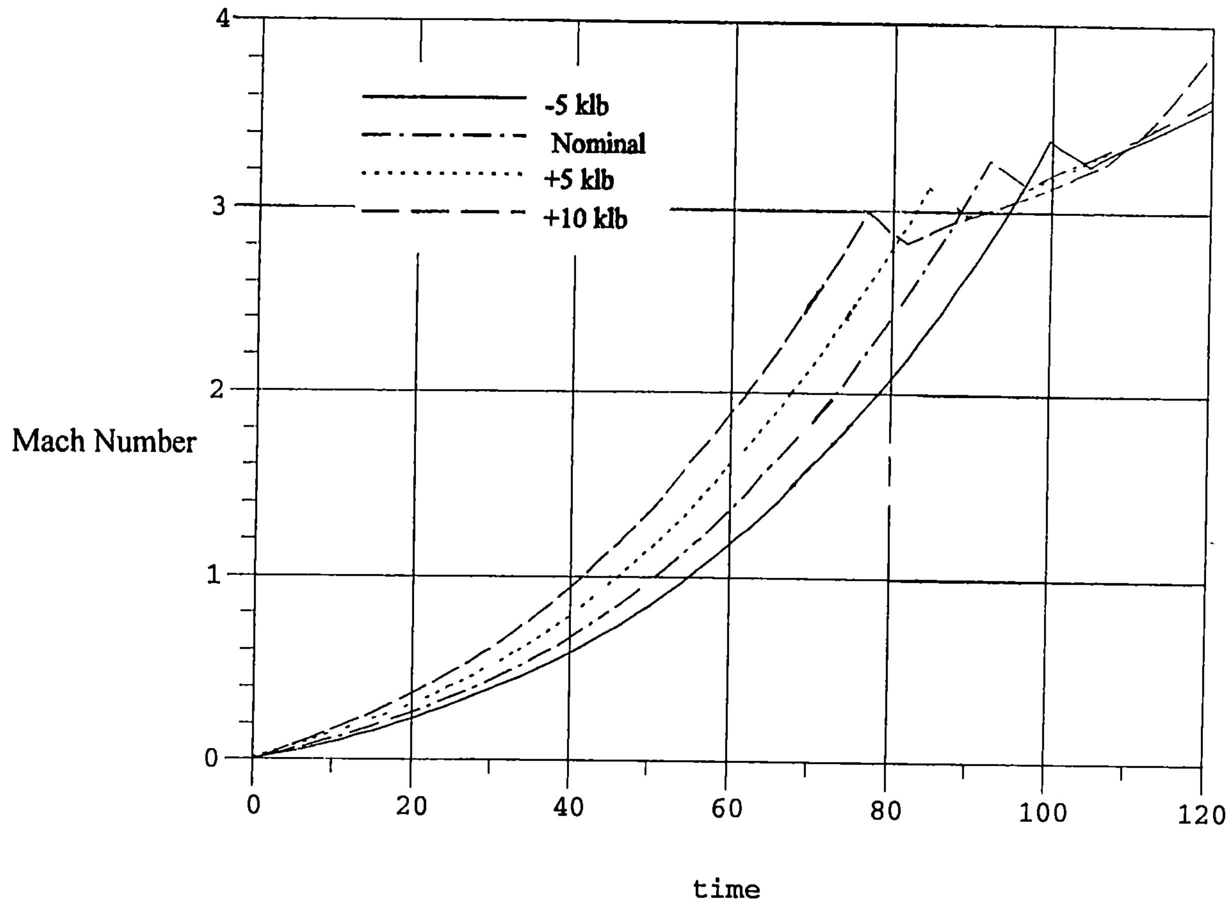

Figure 4.32 : Effect of booster scaling on separation Mach number

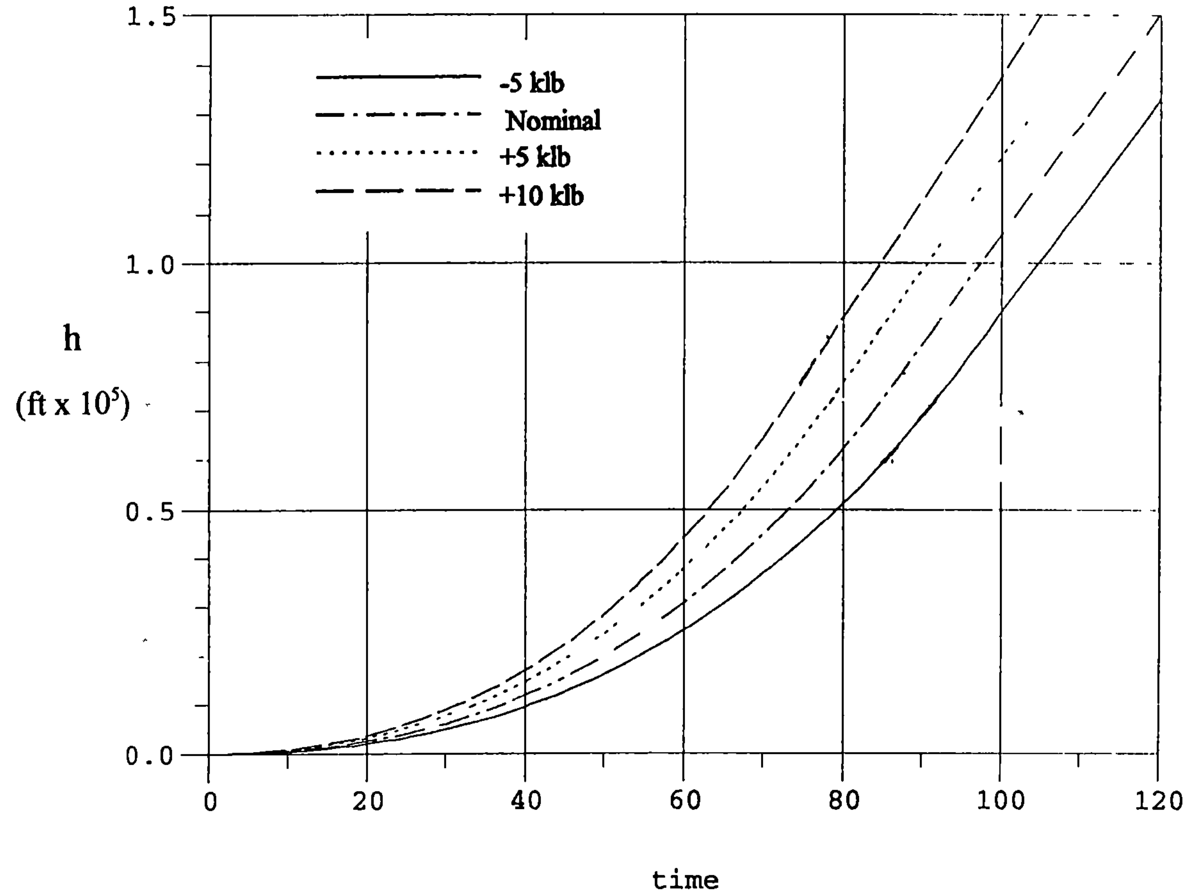

Figure 4.33 : Effect of booster scaling on altitude during boost phase

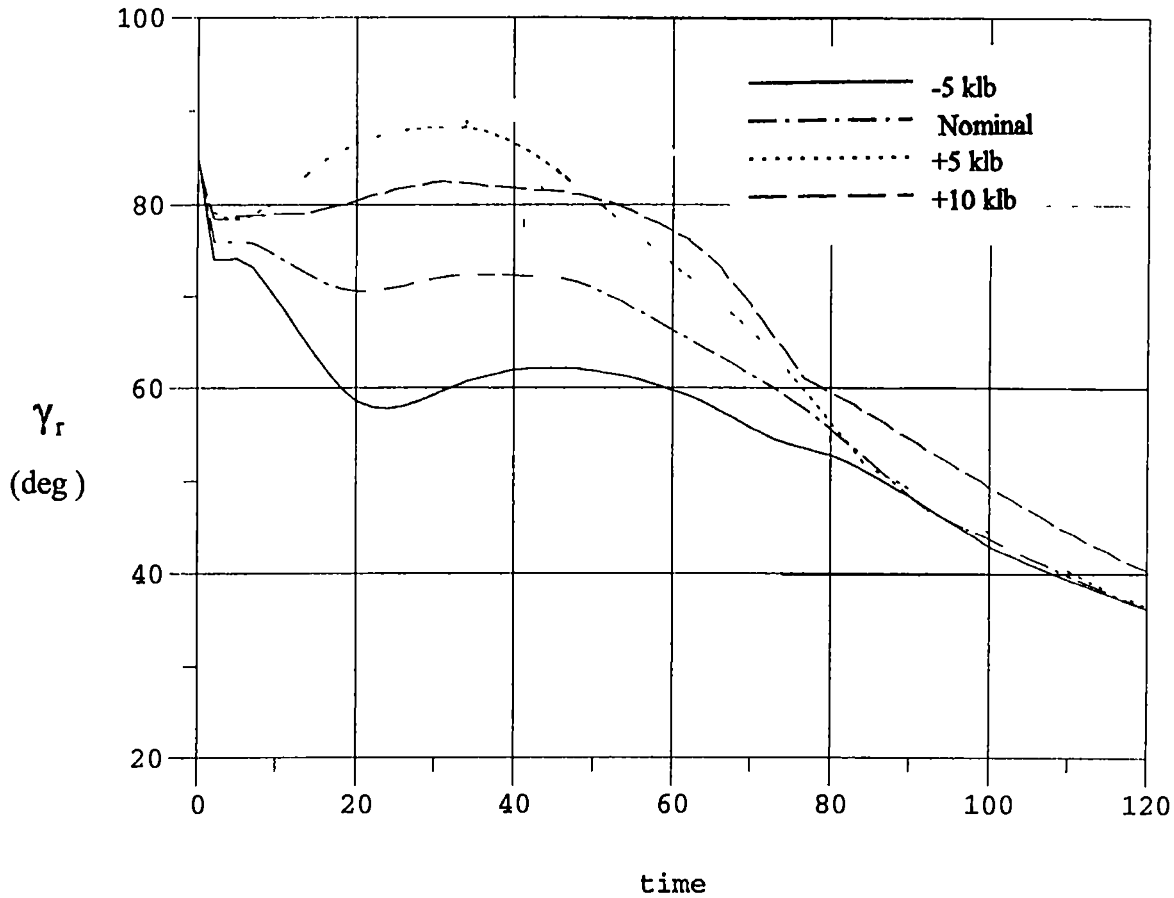

Figure 4.34 : Effect of booster scaling on flight path angle during boost phase

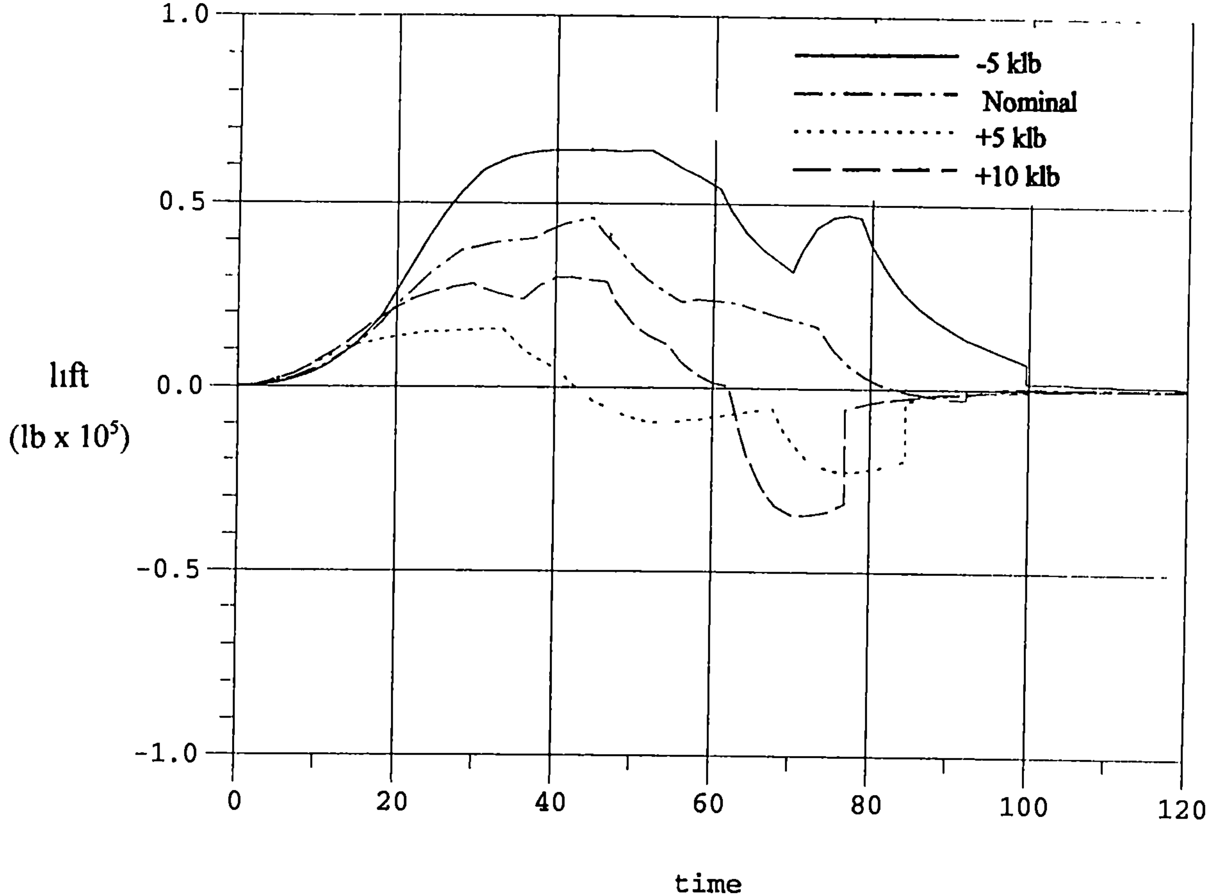

Figure 4.35 : Effect of booster scaling on lift generated during boost phase

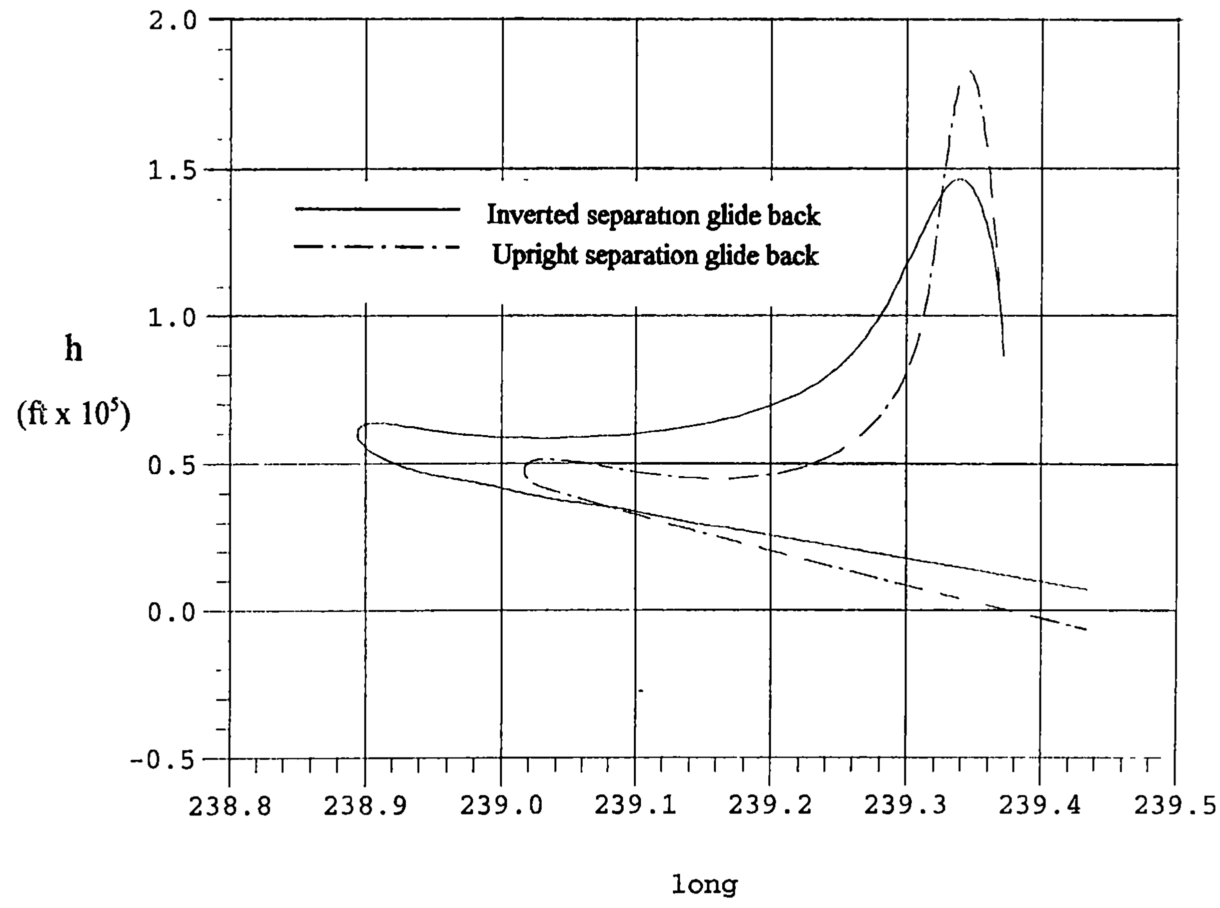

Figure 4 36 . Comparison of upright and inverted separation glide back altitude as a function of longitude

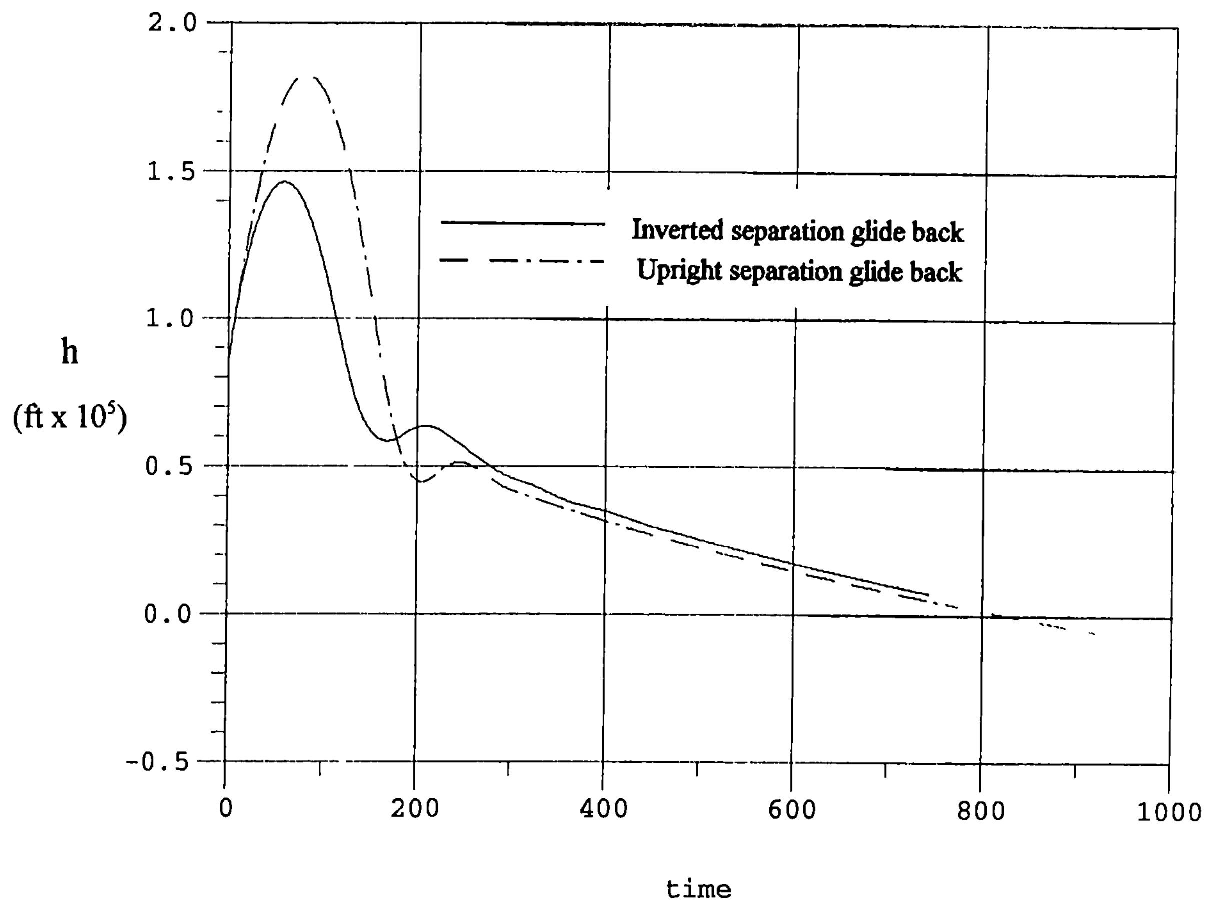

Figure 4 37 : Comparison of upright and inverted separation glide back altitude as a function of time

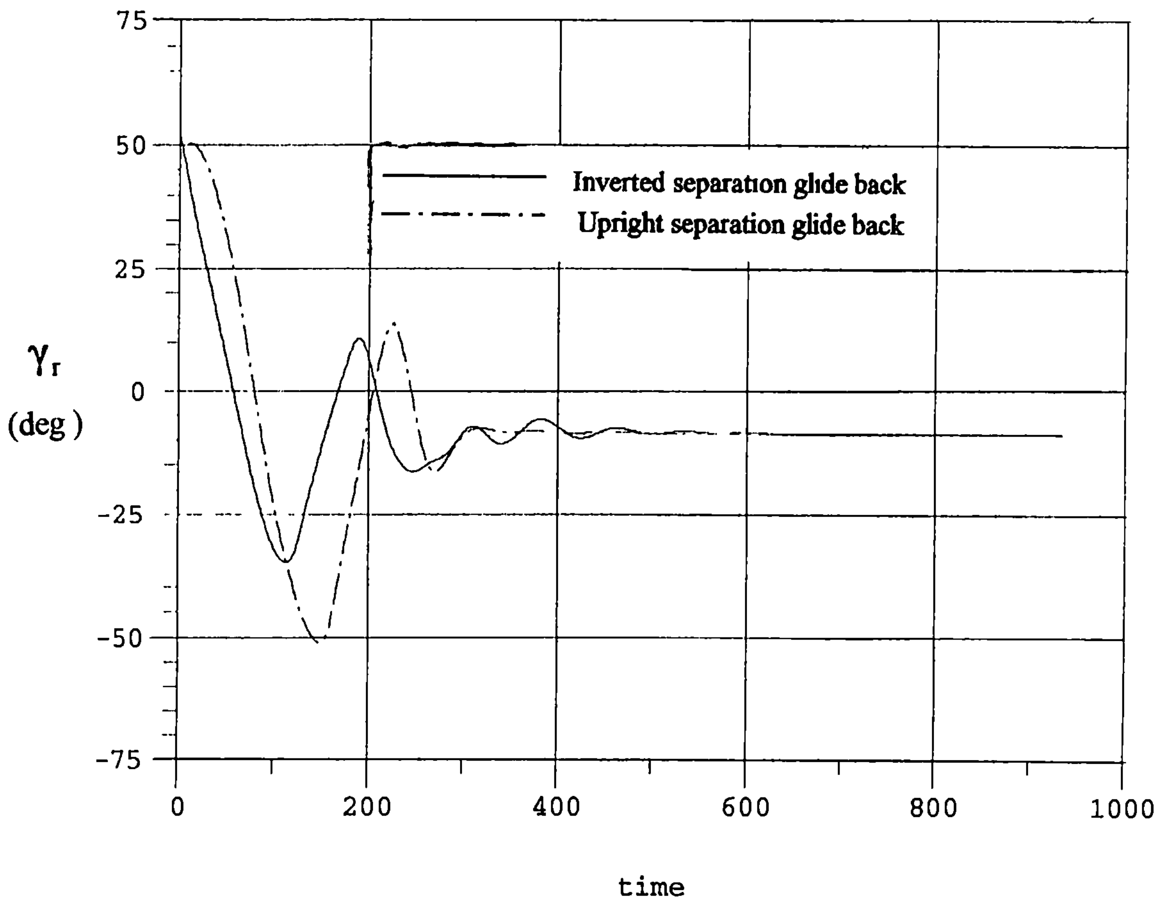

Figure 4 38 Comparison of upright and inverted separation glide back relative flight path angle

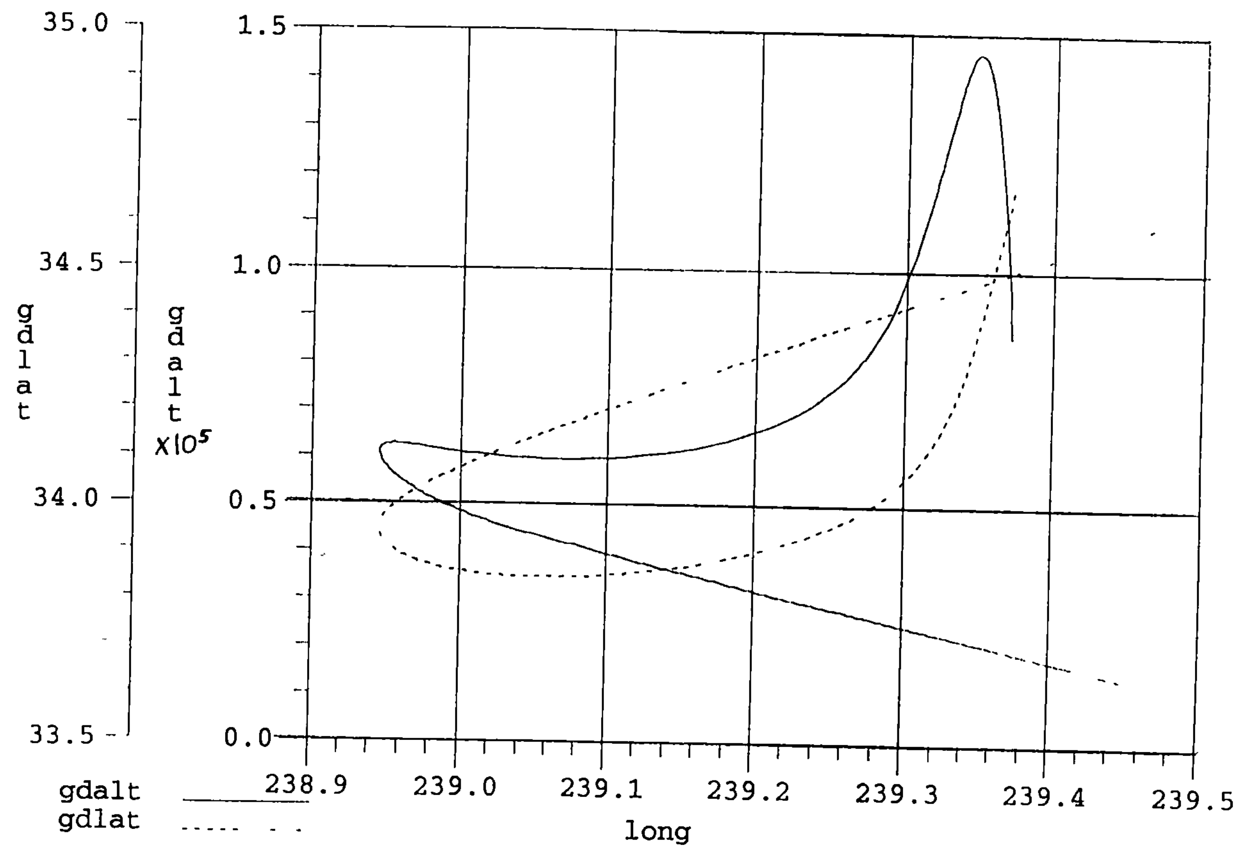

Figure 4 39 · Inverted separation glide back altitude and latitude

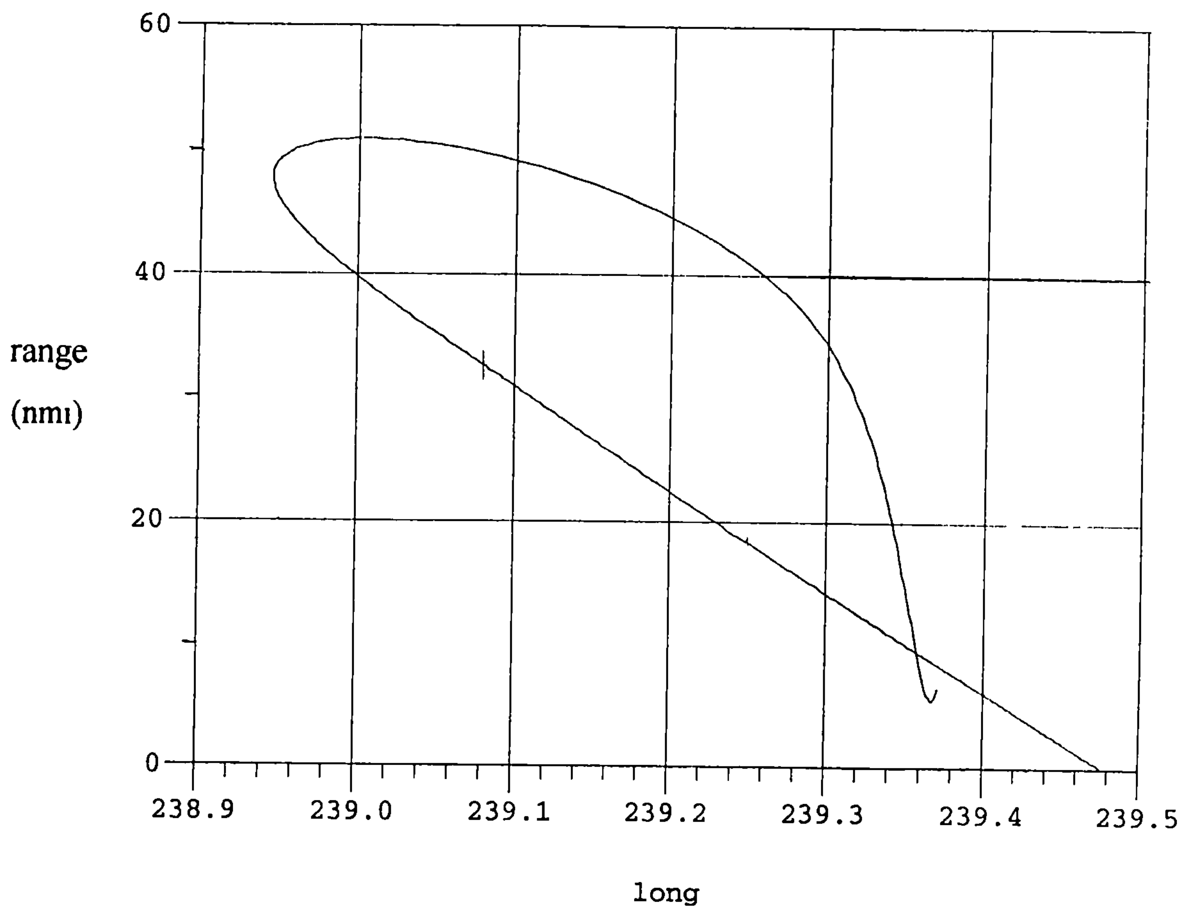

Figure 4 40 Inverted separation glide back range from heading alignment cylinder

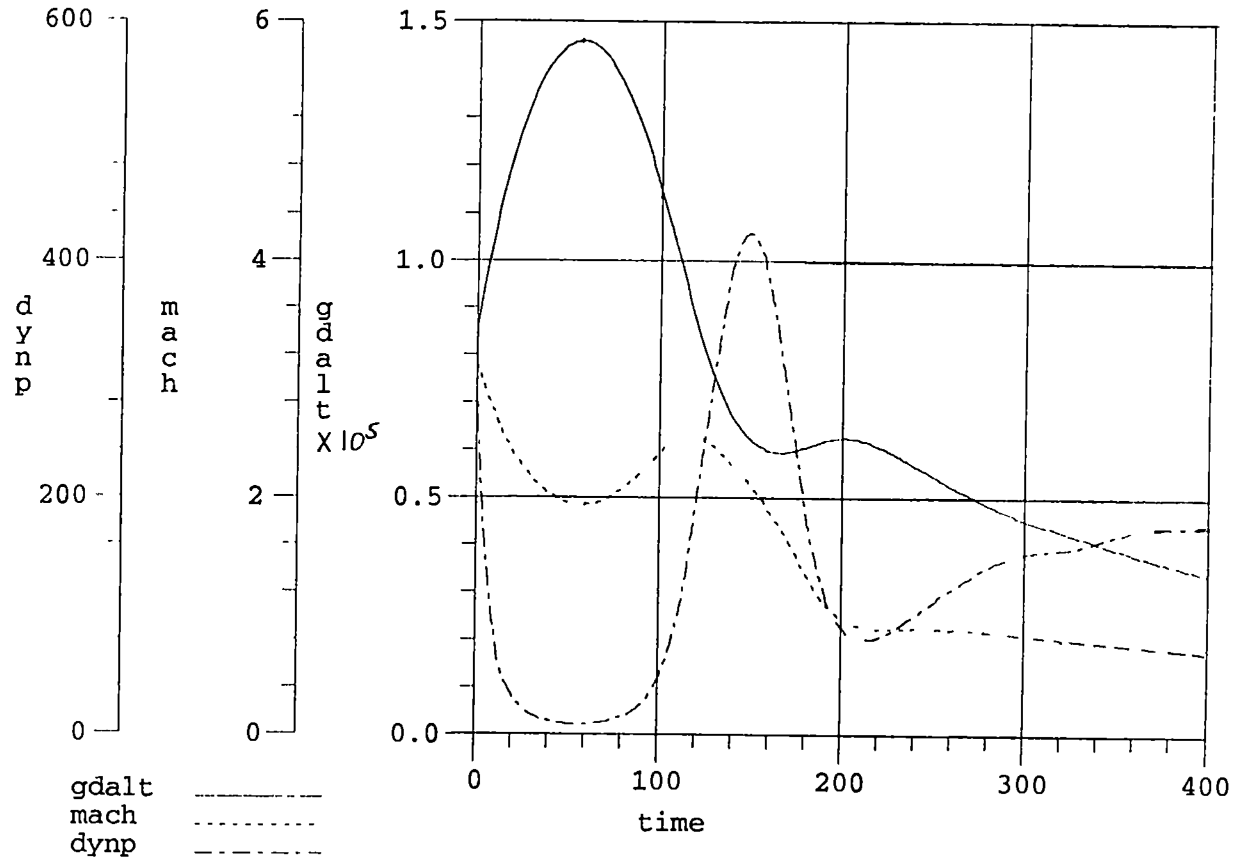

Figure 4.41 Inverted separation glide back altitude, Mach number and dynamic pressure from separation to obtaining heading to HAC

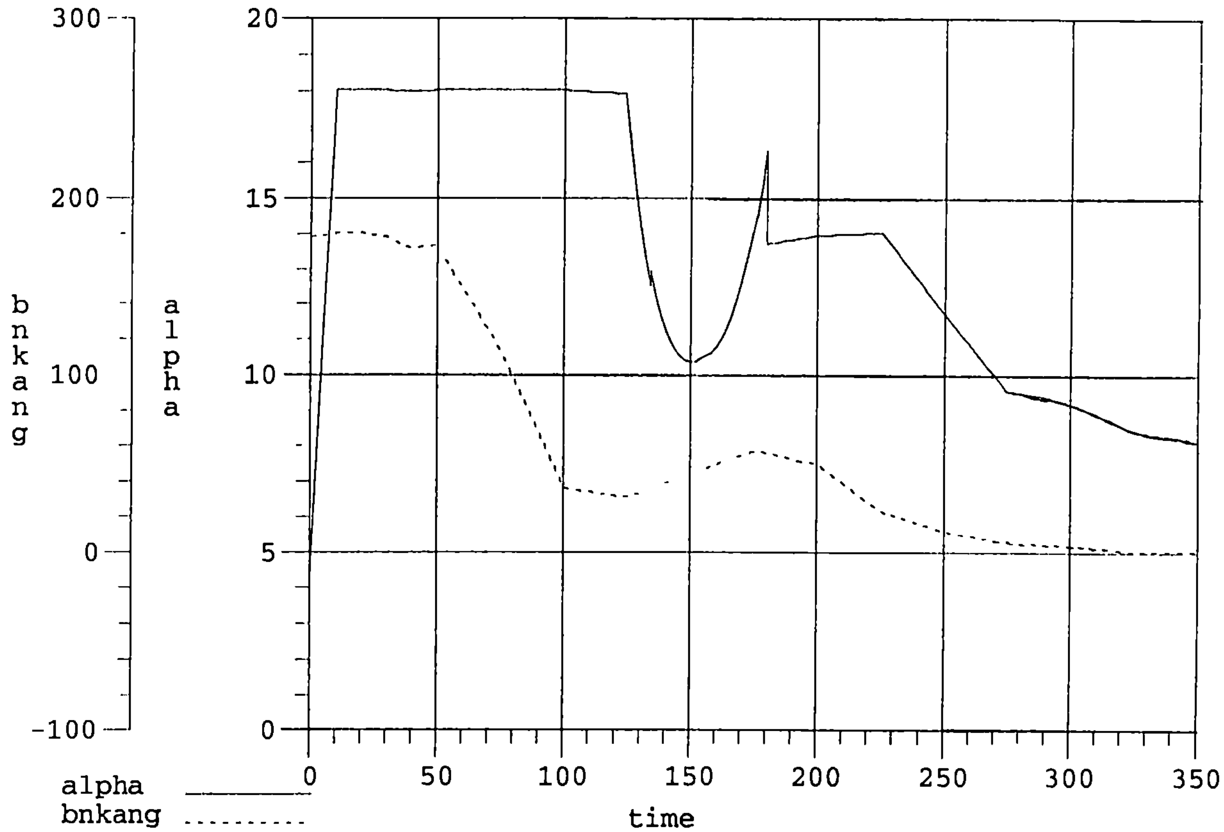

Figure 4.42 : Booster angle of attack and bank angle from separation until attaining a heading to the heading alignment cylinder for the altitude limiting trajectory.

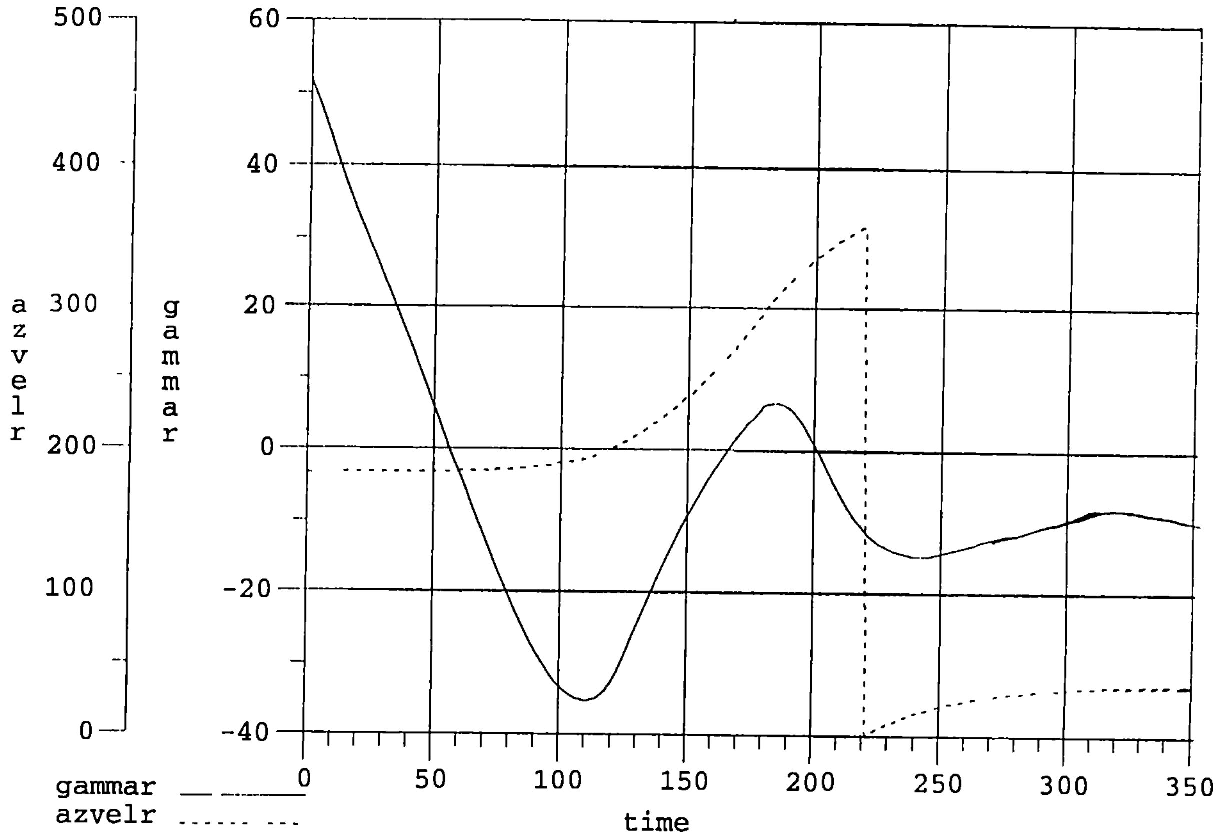

Figure 4 43 Inverted separation glide back relative flight path angel and relative velocity azimuth from separation to obtaining heading to HAC

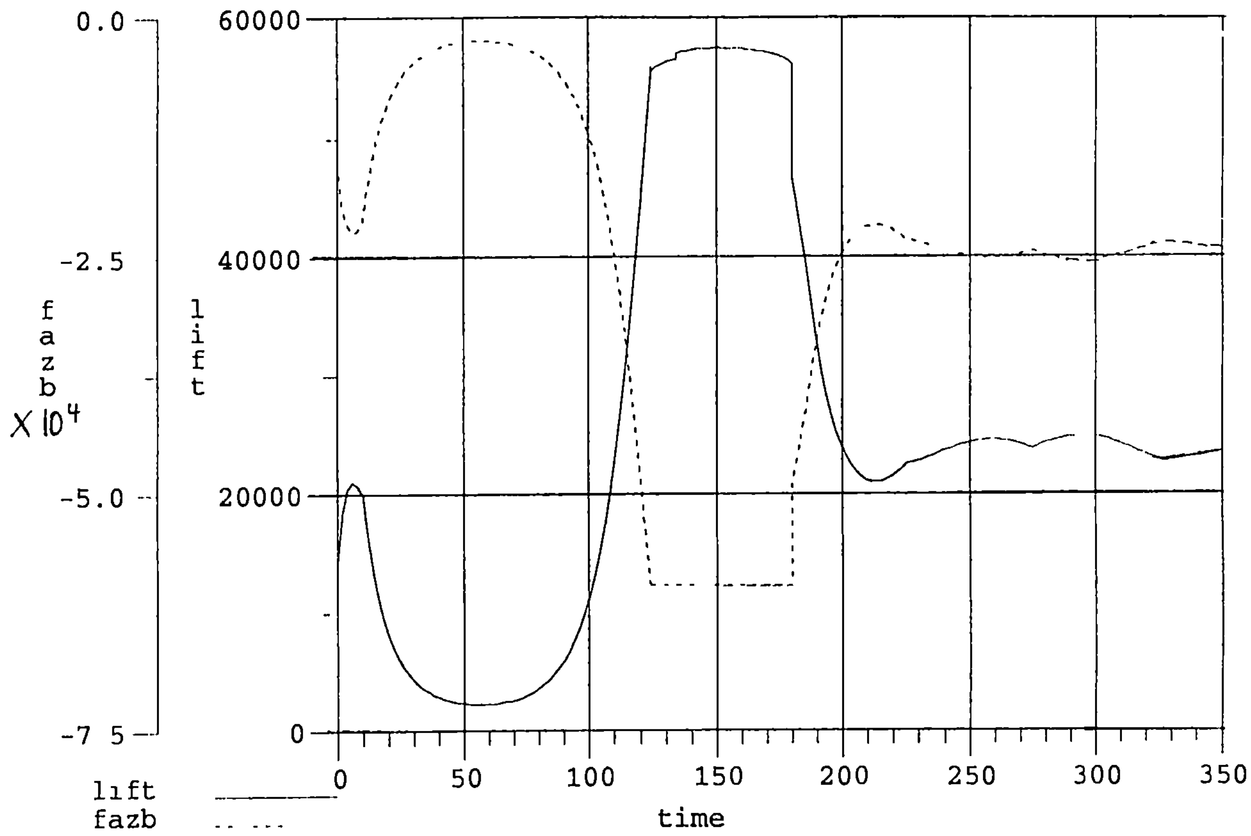

Figure 4.44 · Inverted separation glide back lift and normal force from separation to obtaining heading to HAC

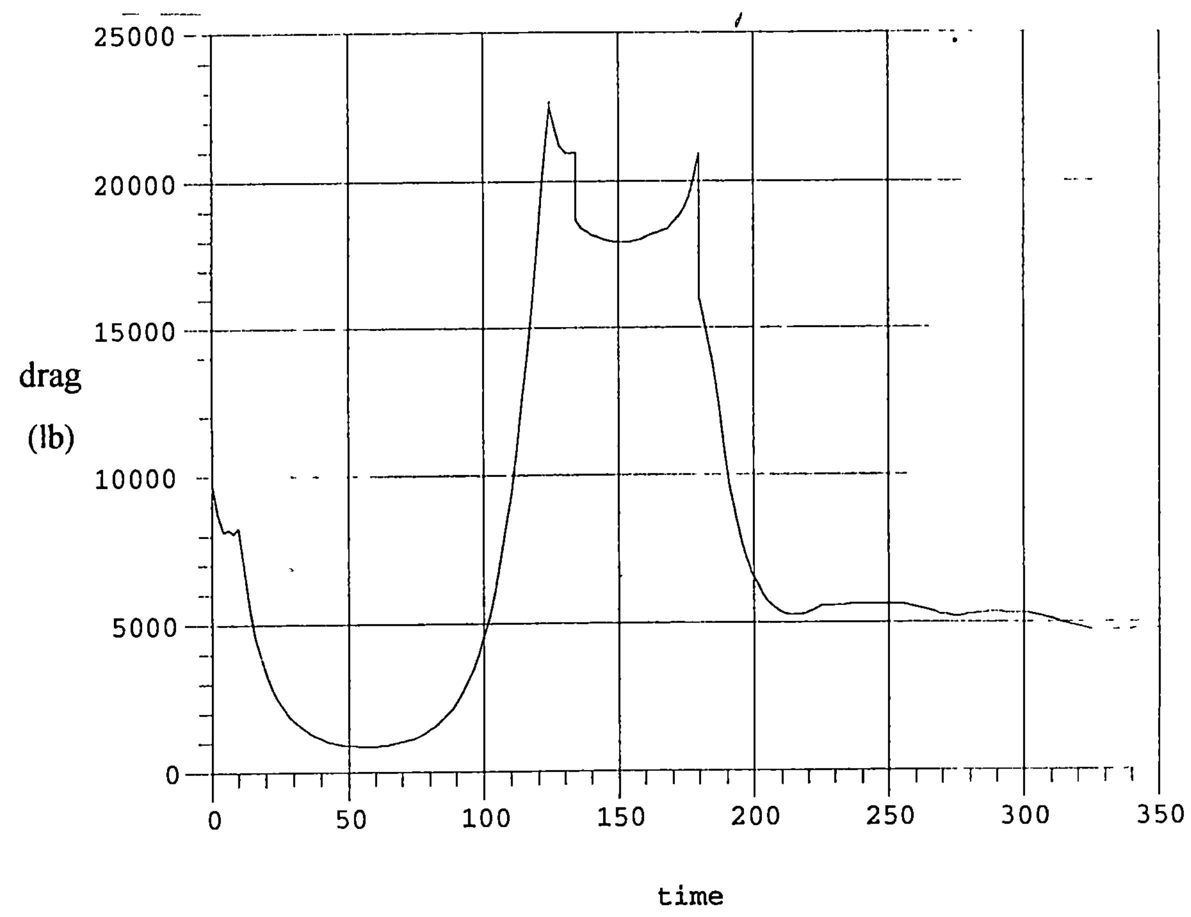

Figure 4.45 : Inverted separation glide back drag force from separation to obtaining heading to HAC

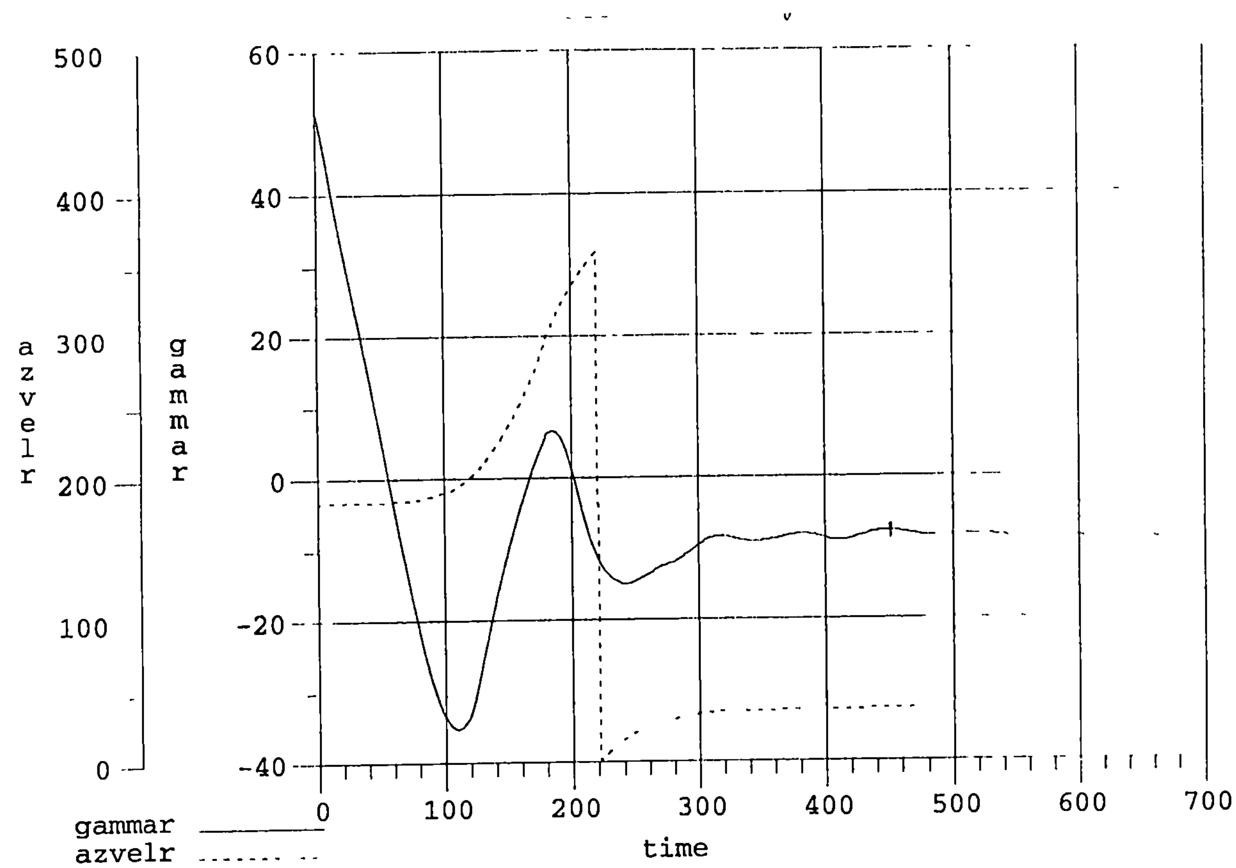

Figure 4 46 Inverted separation glide back relative flight path angle and relative velocity azimuth throughout entire glide back

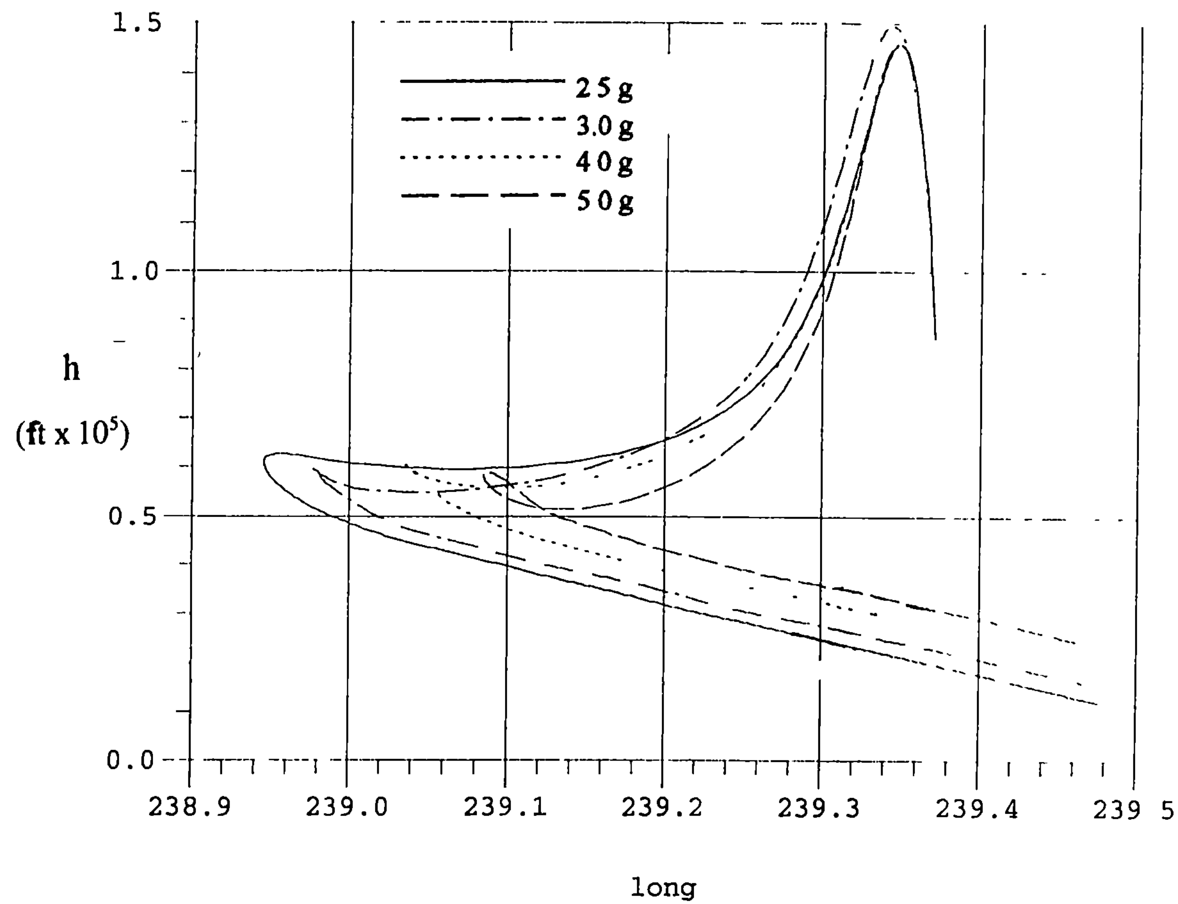

Figure 4.47 : Effect of increasing normal force limit on booster glide back altitude

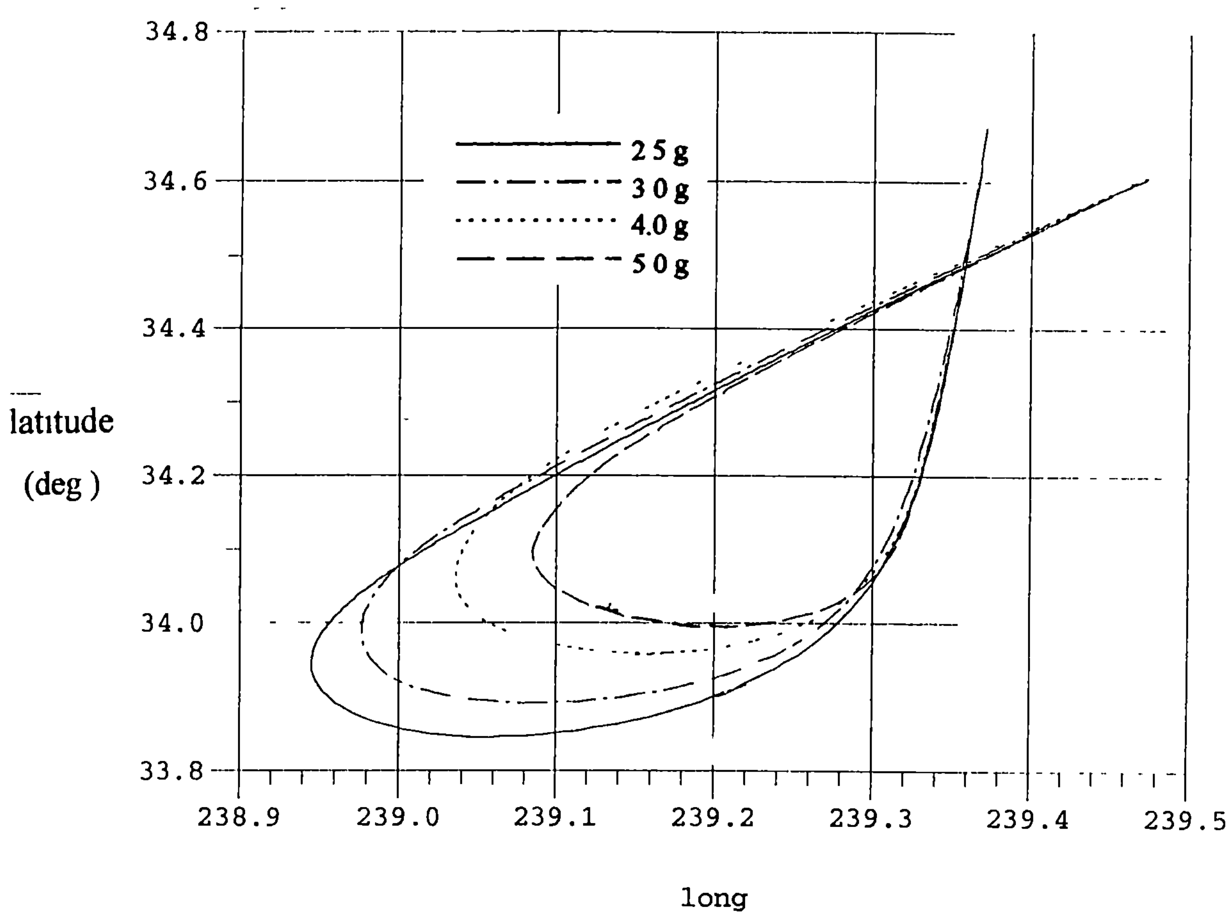

Figure 4.48 : Effect of increasing normal force limit on booster glide back ground track

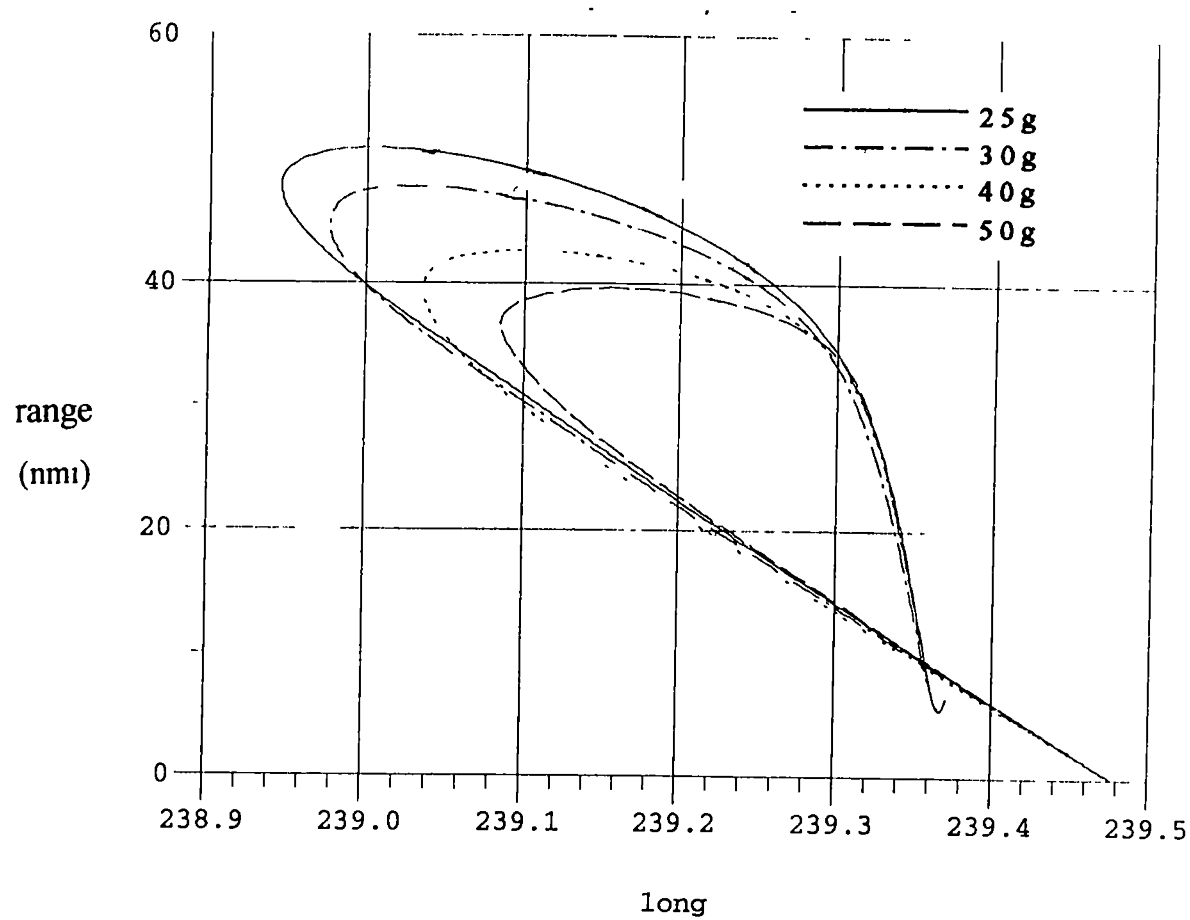

Figure 4.49 : Effect of increasing normal force limit on booster range from heading alignment cylinder during glide back

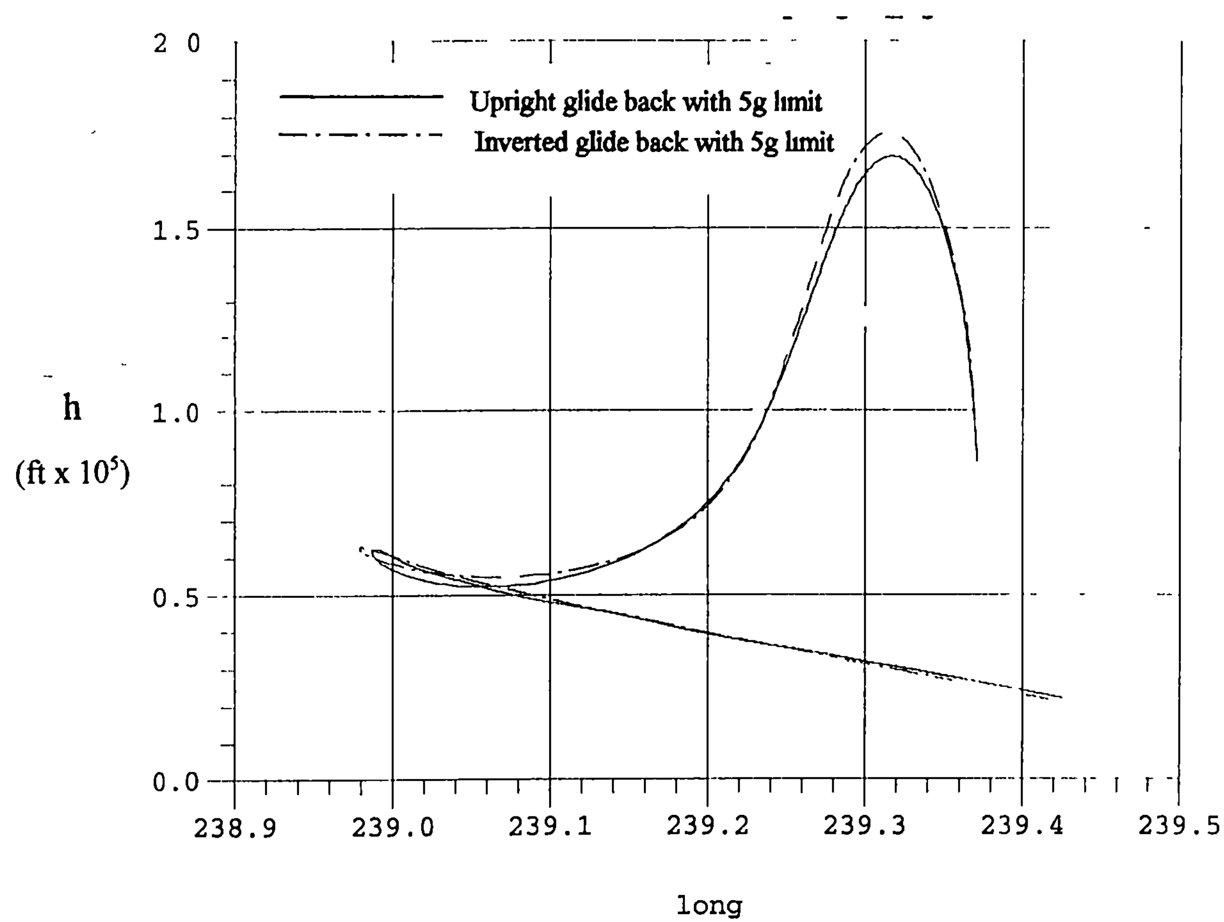

Figure 4.51 Comparison of upright and inverted glide back with 5g normal force limit

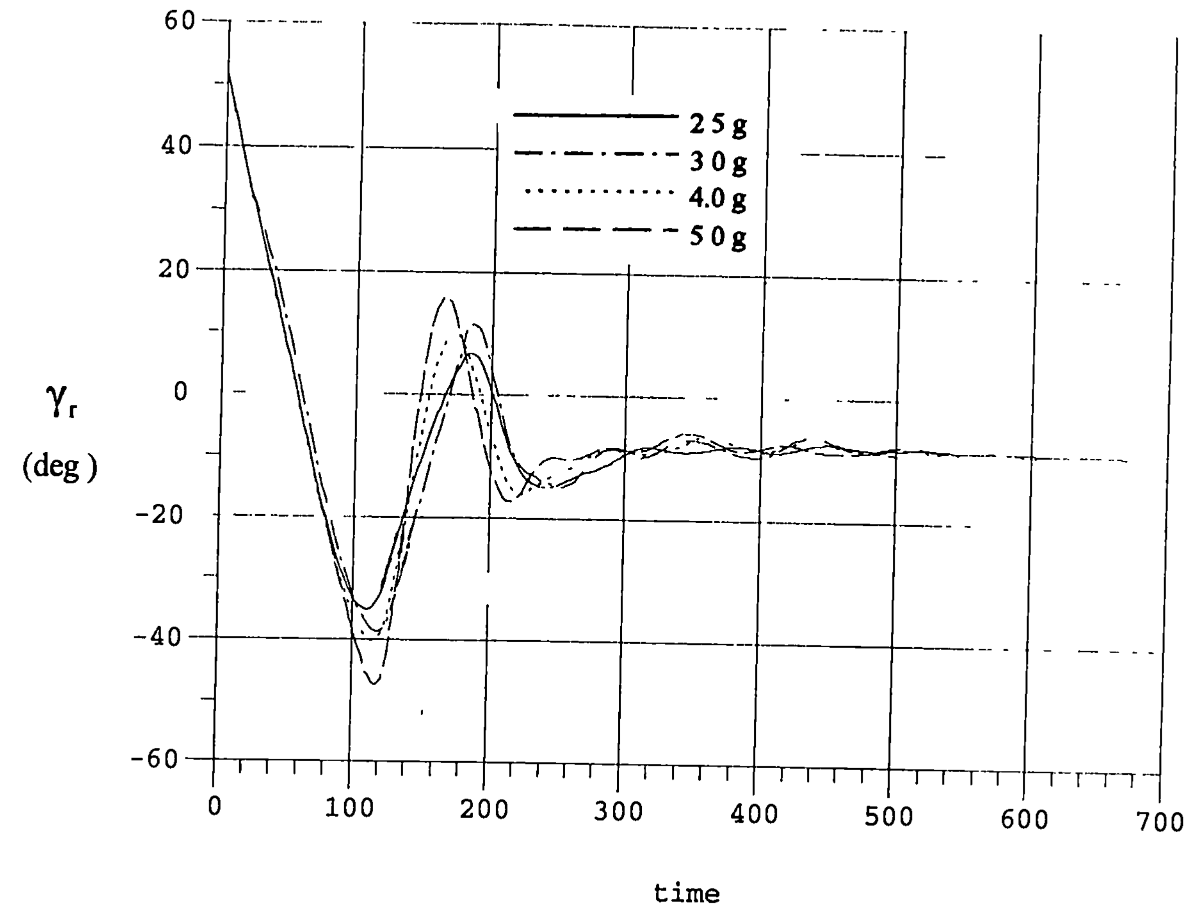

Figure 4.50 : Effect of increasing normal force limit on booster flight path angle during glide back

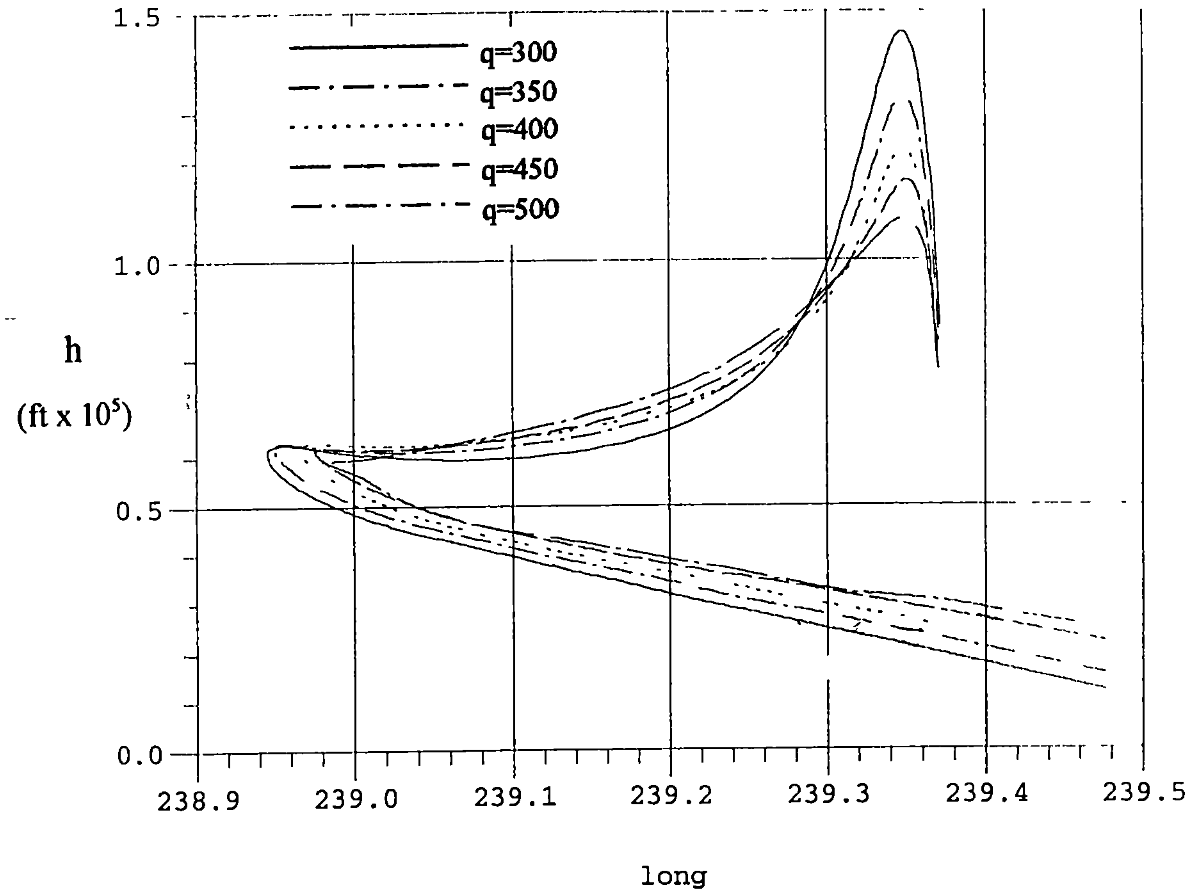

Figure 4.52 : Effect of increasing dynamic pressure at separation on booster altitude during glide back

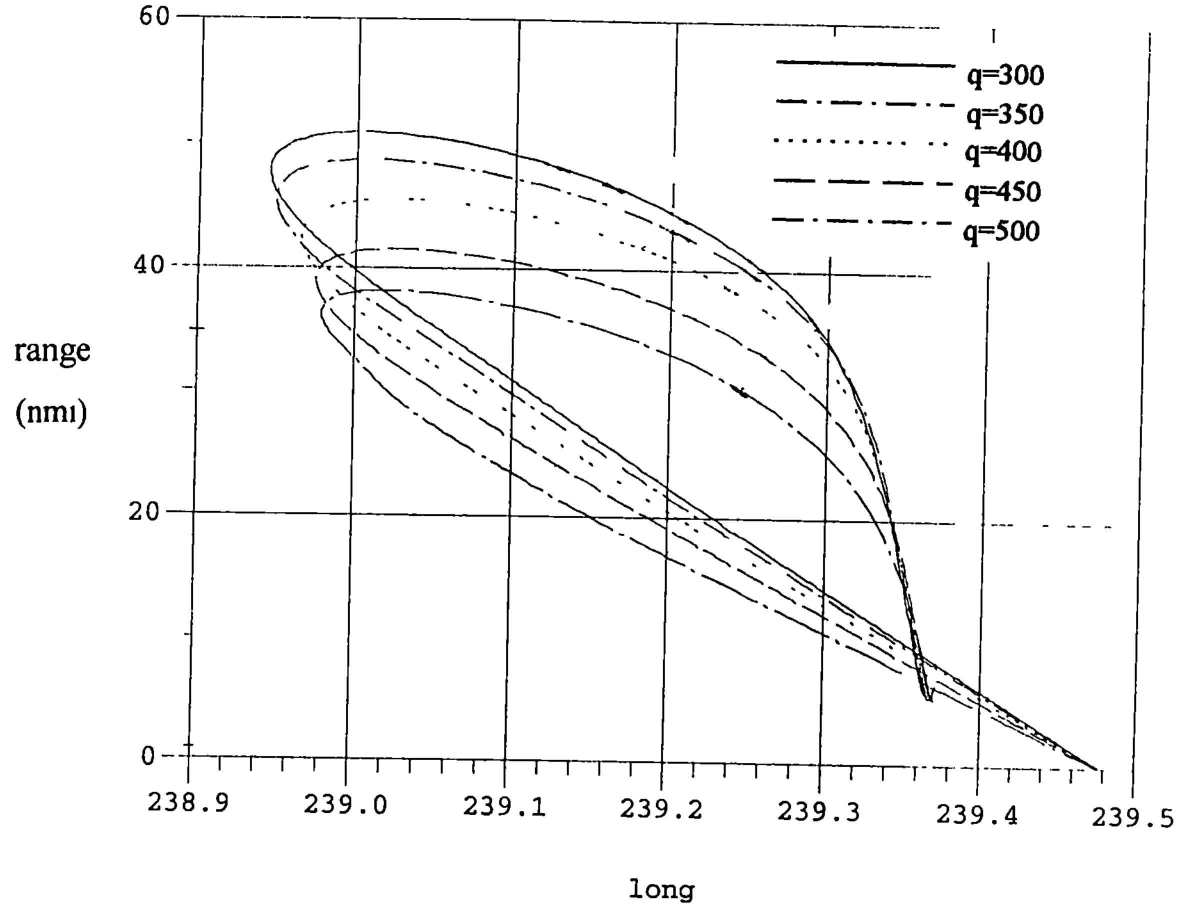

Figure 4.53 : Dynamic pressure at separation influence on booster range from heading alignment cylinder during glide back

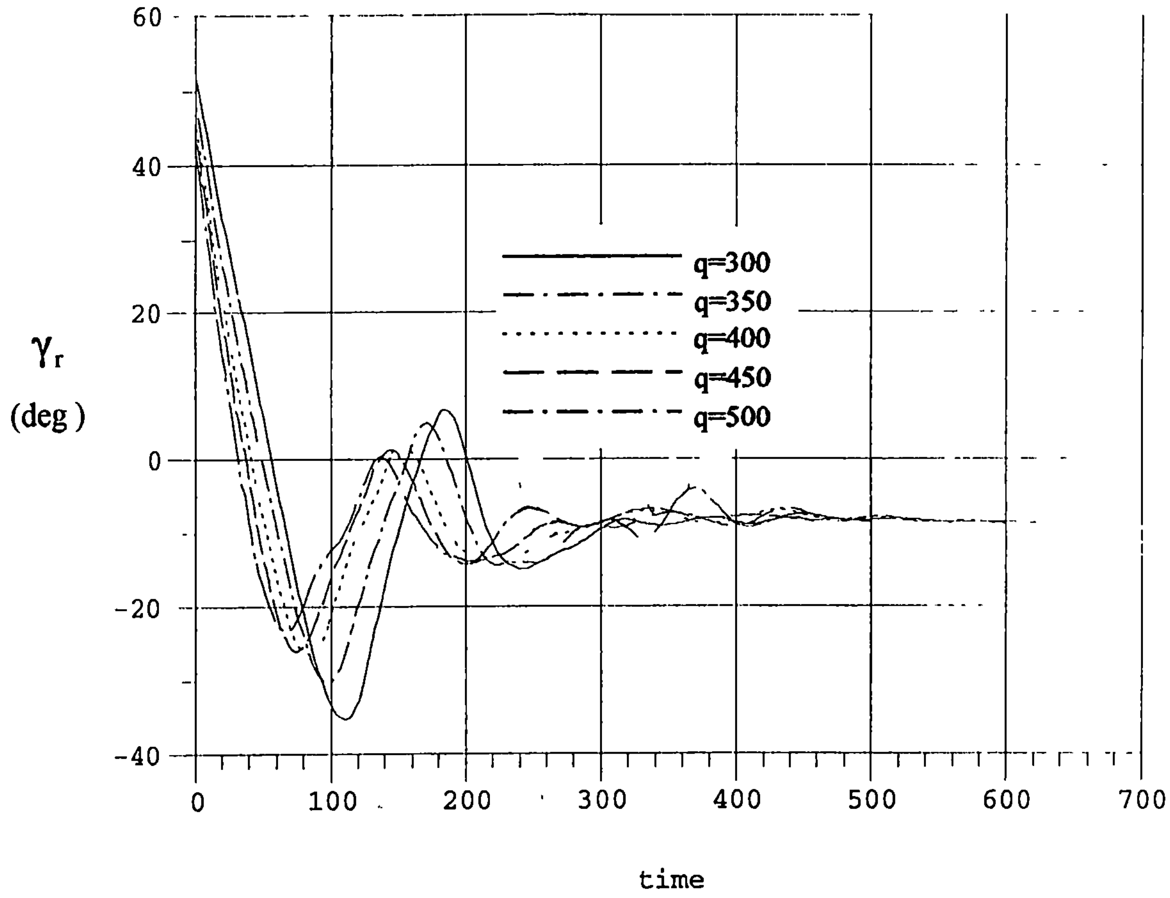

Figure 4.54 : Effect of increasing dynamic pressure at separation on booster flight path angle during glide back

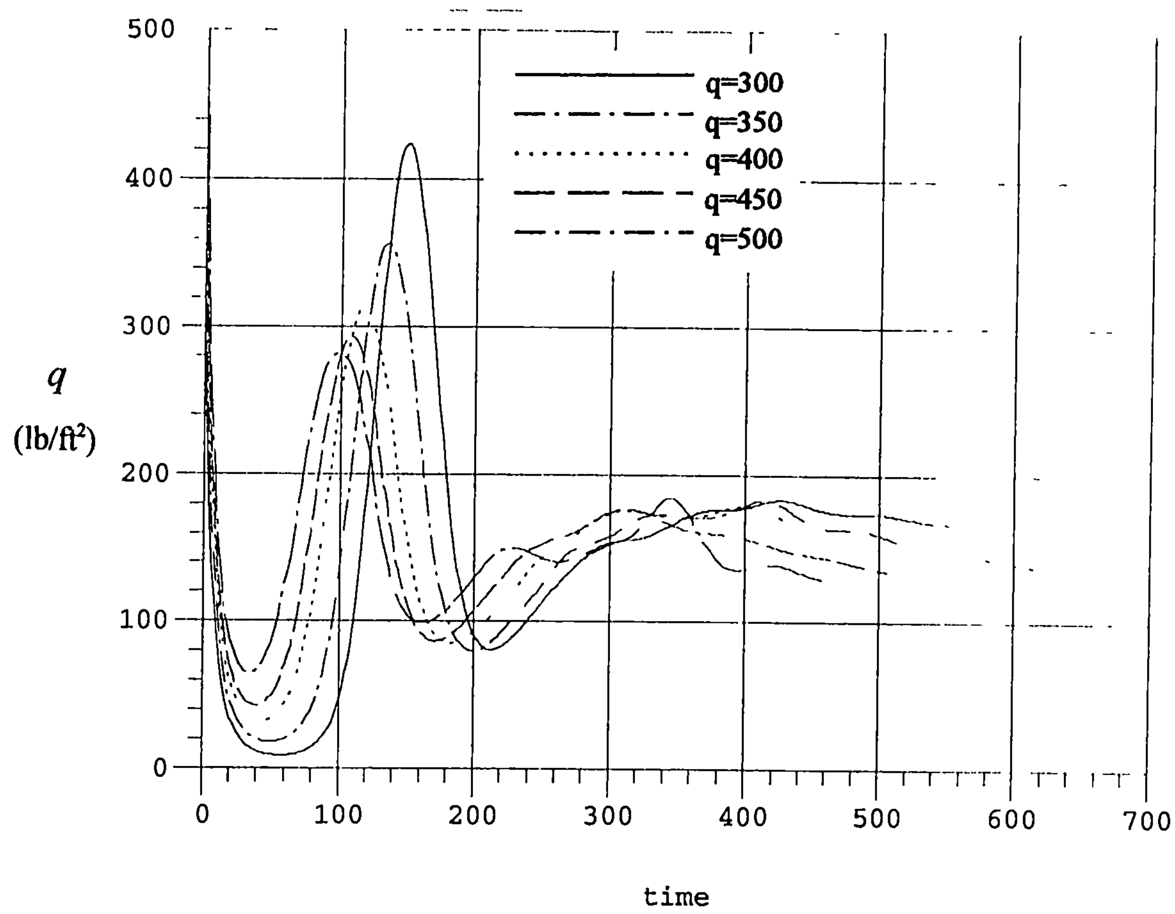

Figure 4.55 : Effect of increasing dynamic pressure at separation on dynamic pressure throughout booster glide back

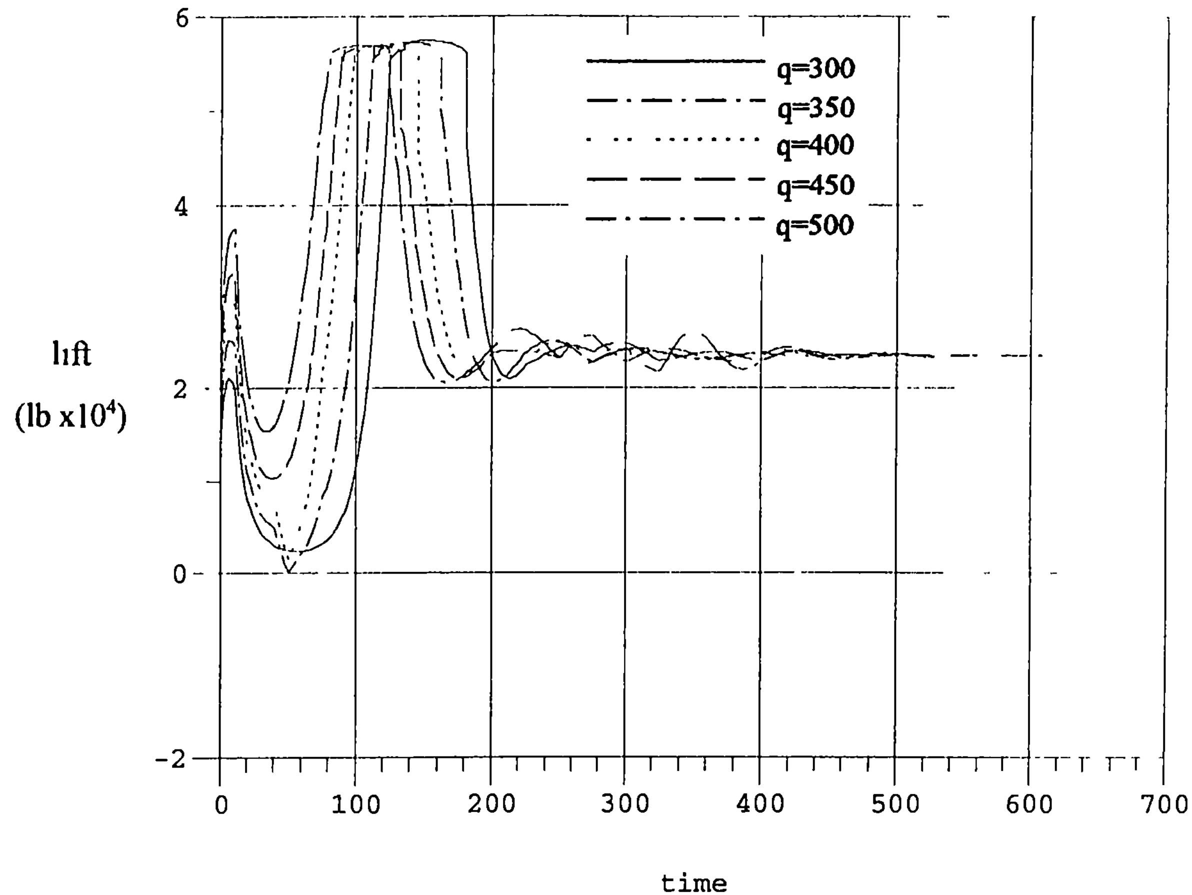

Figure 4 56 . Effect of separation dynamic pressure on lift generated for inverted separation glide back

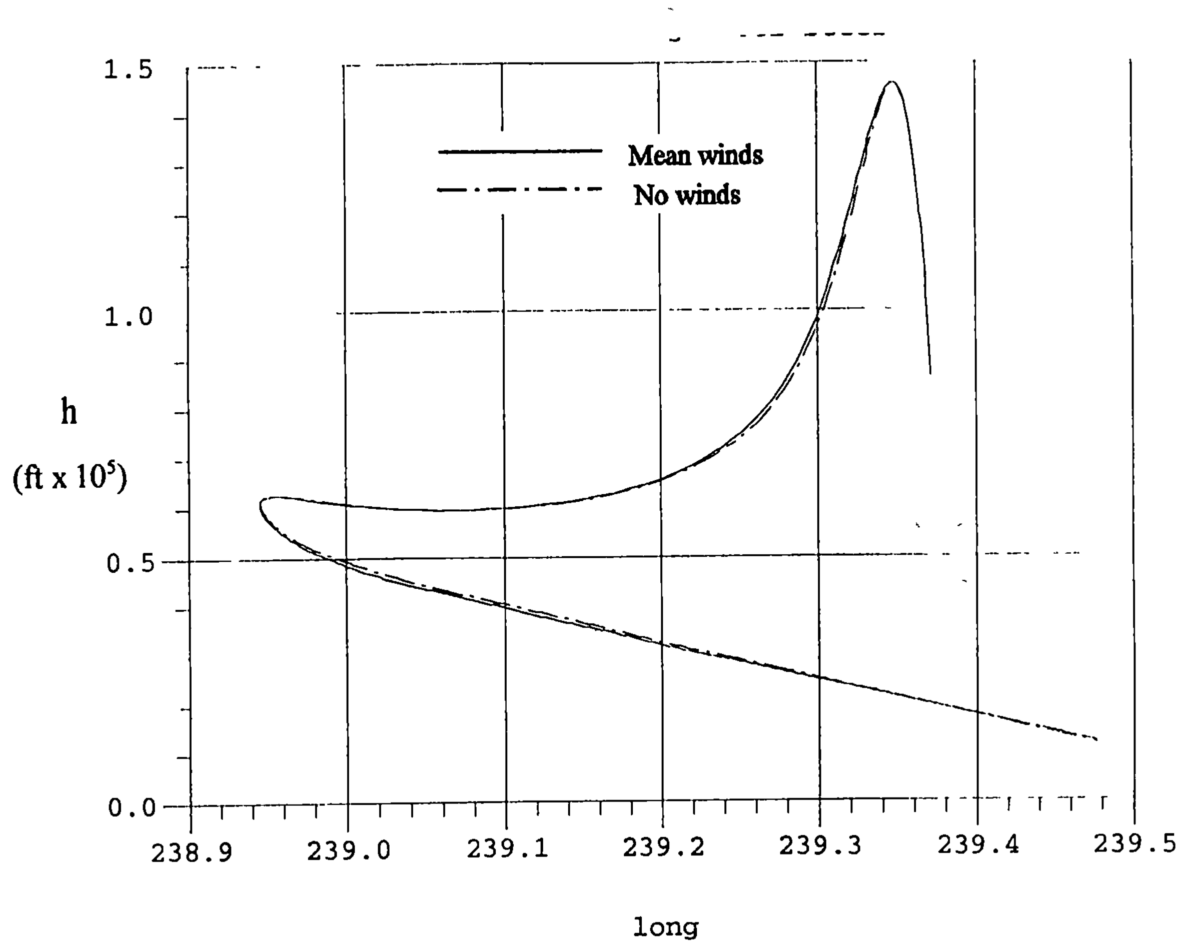

Figure 4 57 . Effect of mean wind on inverted separation glide back altitude

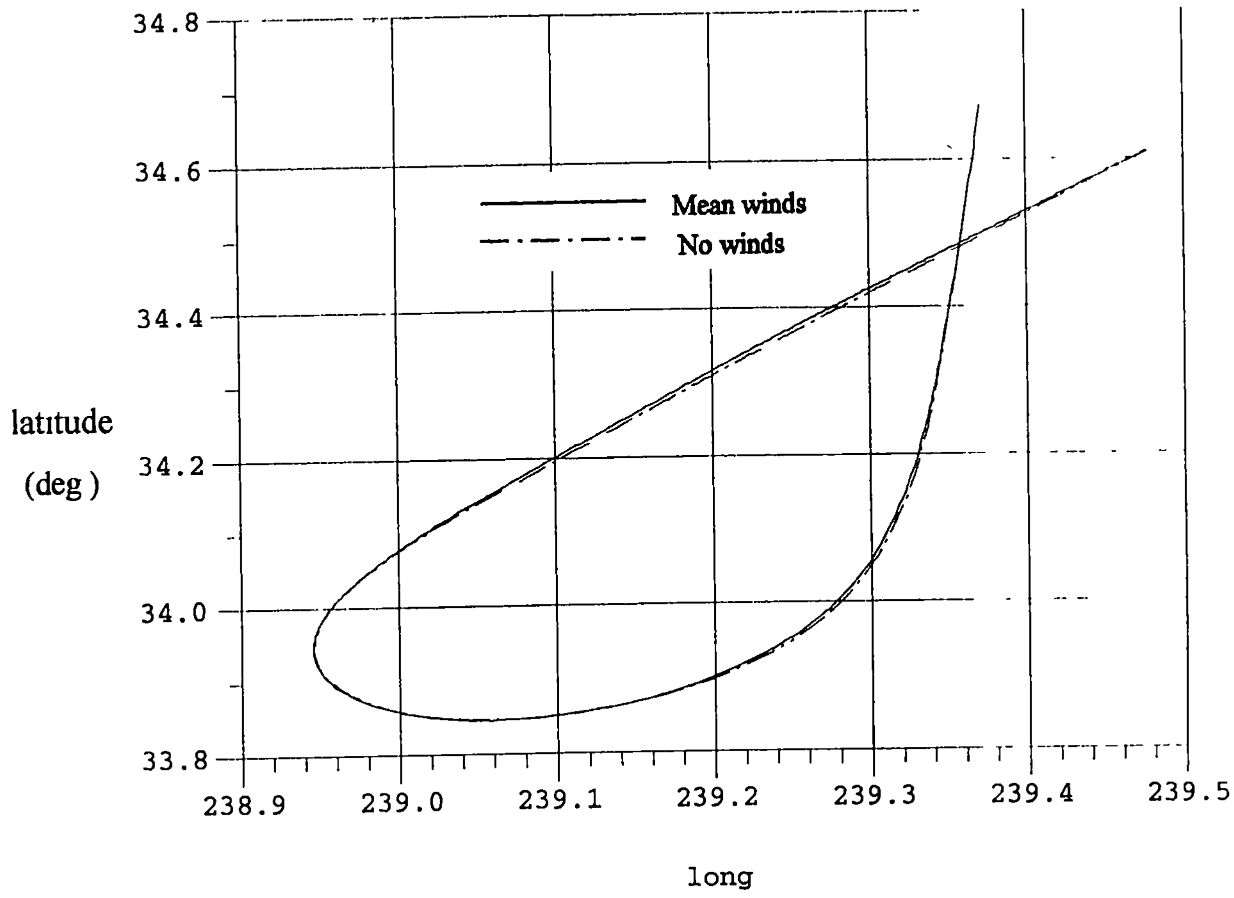

Figure 4 58 Effect of mean wind on inverted separation glide back ground track

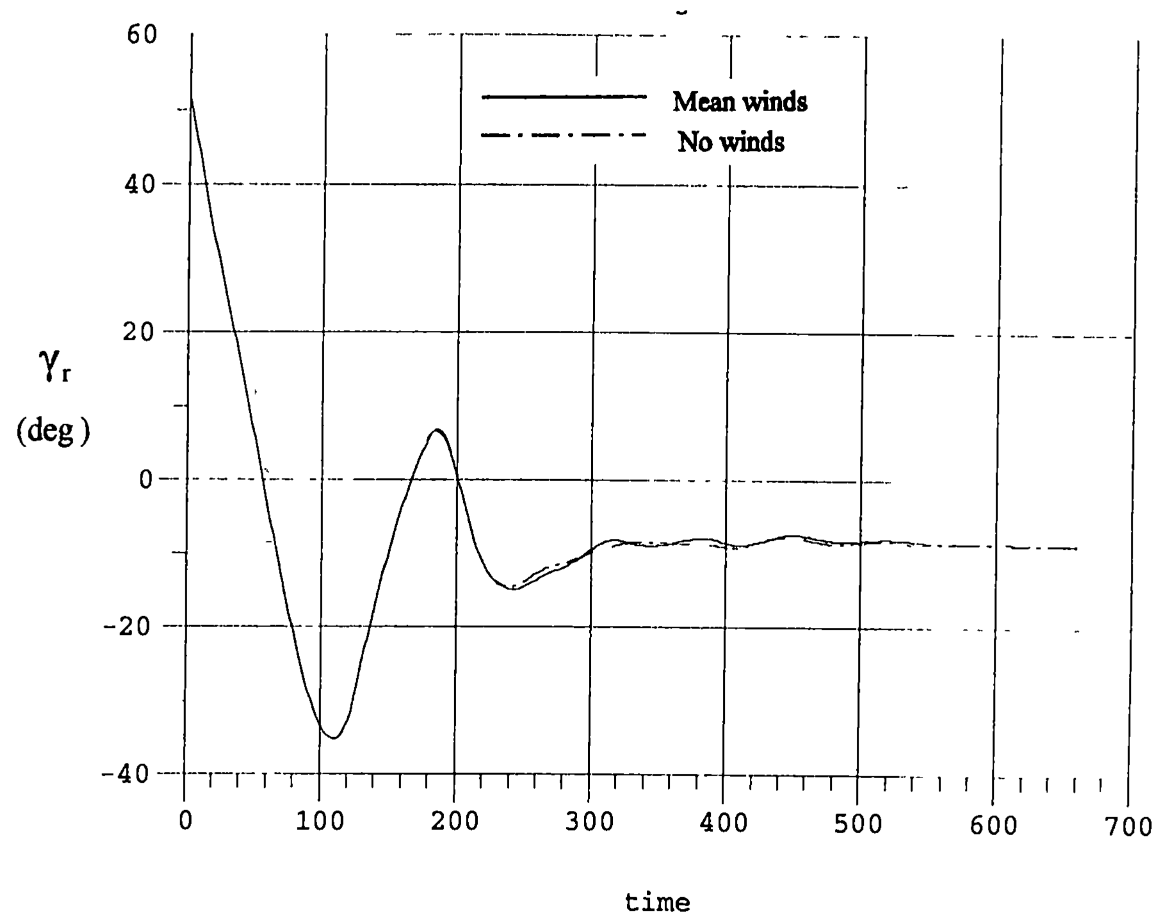

Figure 4.59 Effect of mean wind on inverted separation glide back relative flight path angle

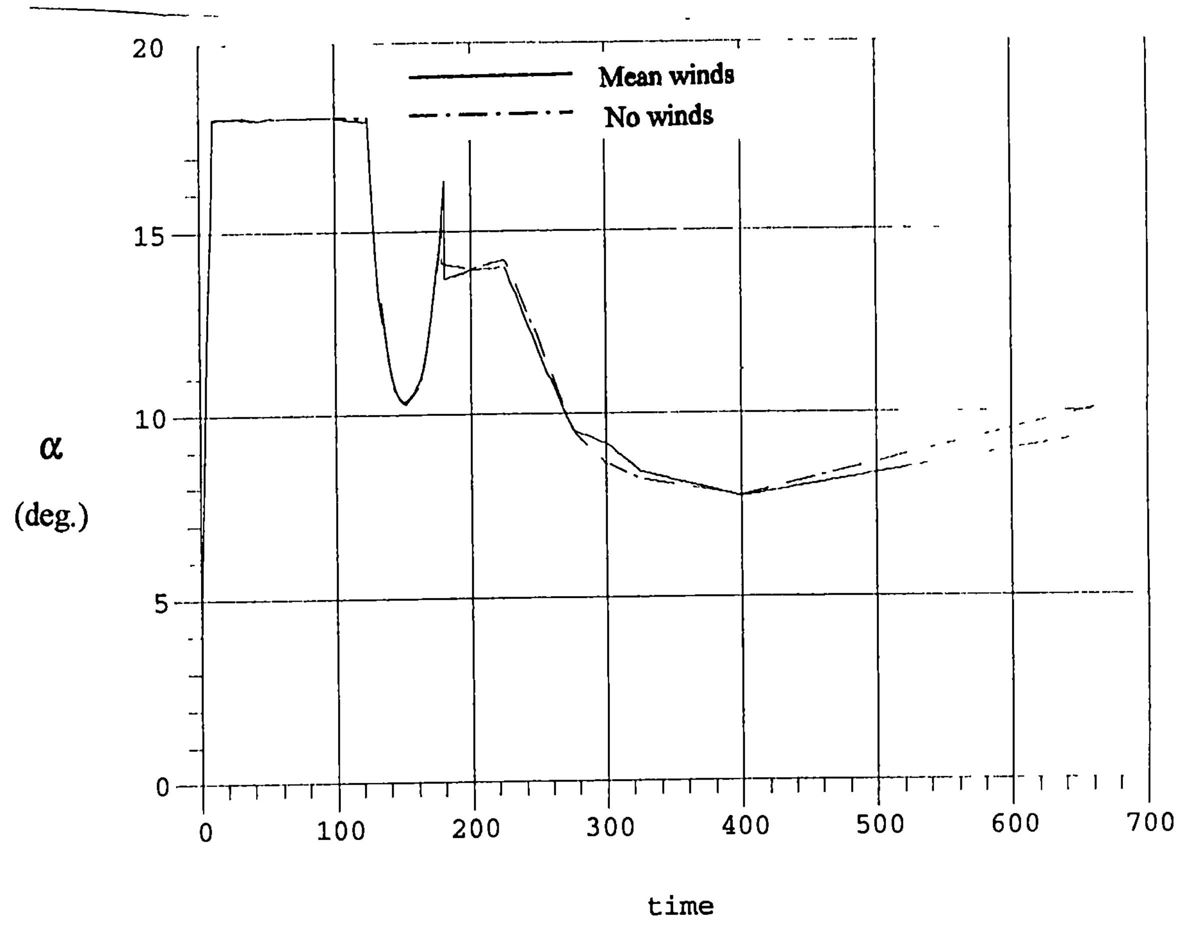

Figure 4 60 · Effect of mean wind on inverted separation glide back angel of attack

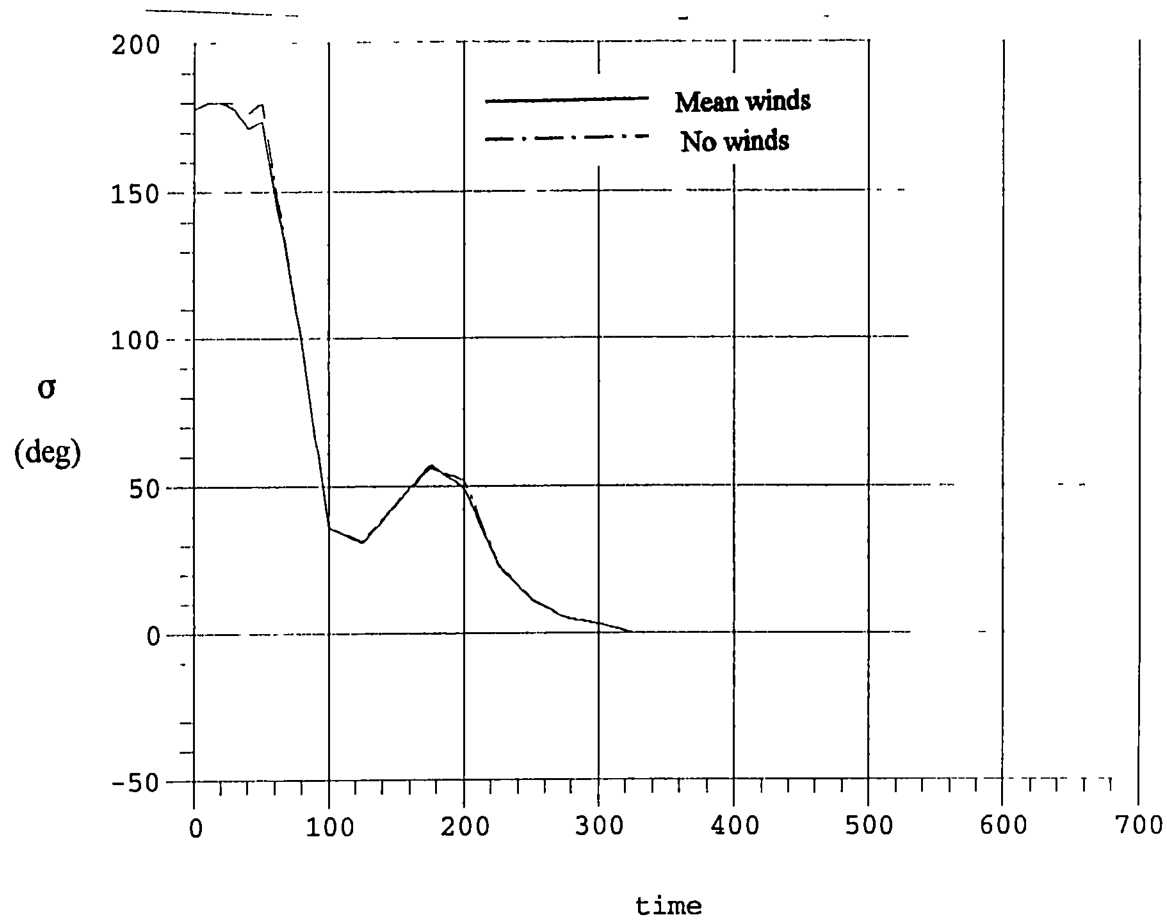

Figure 4 61 . Effect of mean wind on inverted separation glide back bank angle

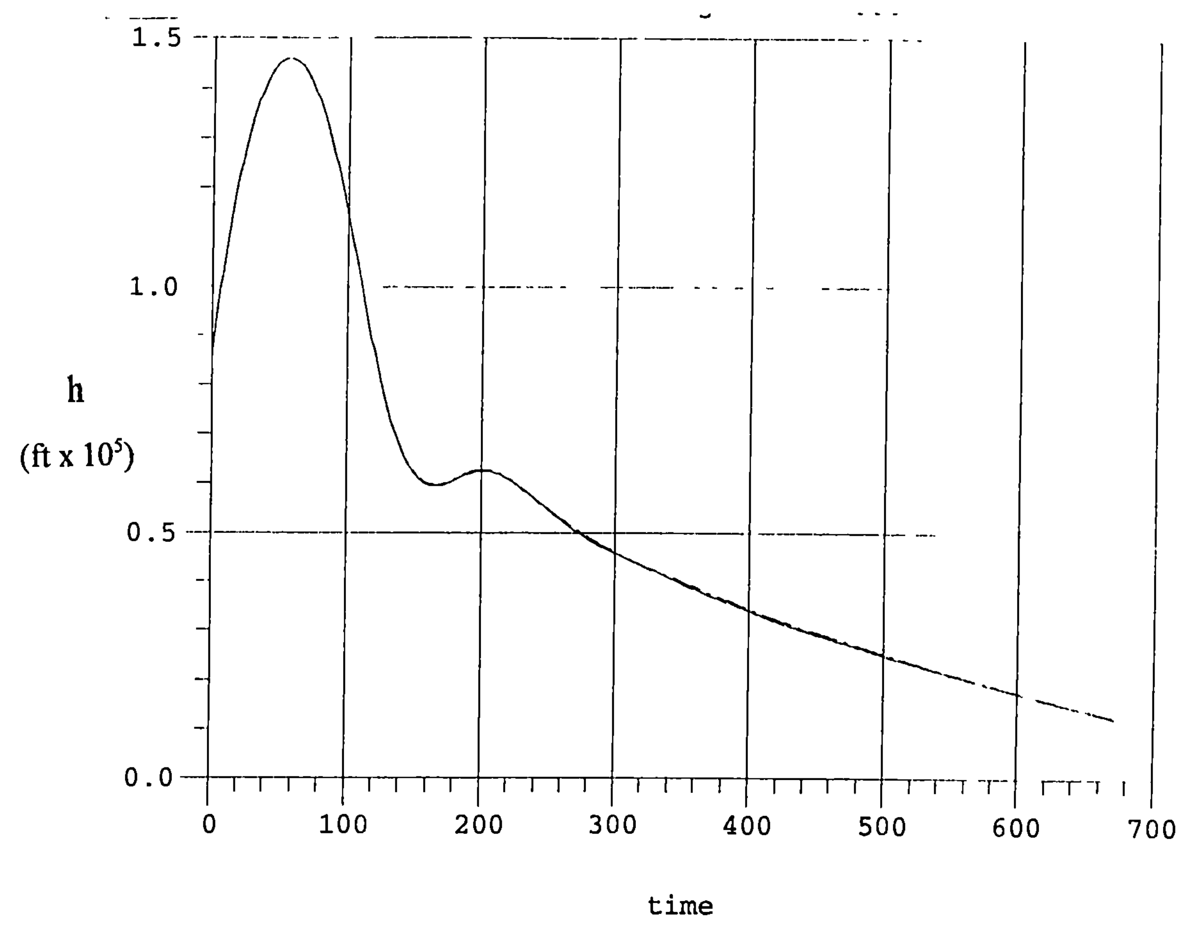

Figure 4 62 Inverted separation altitude as a function of time

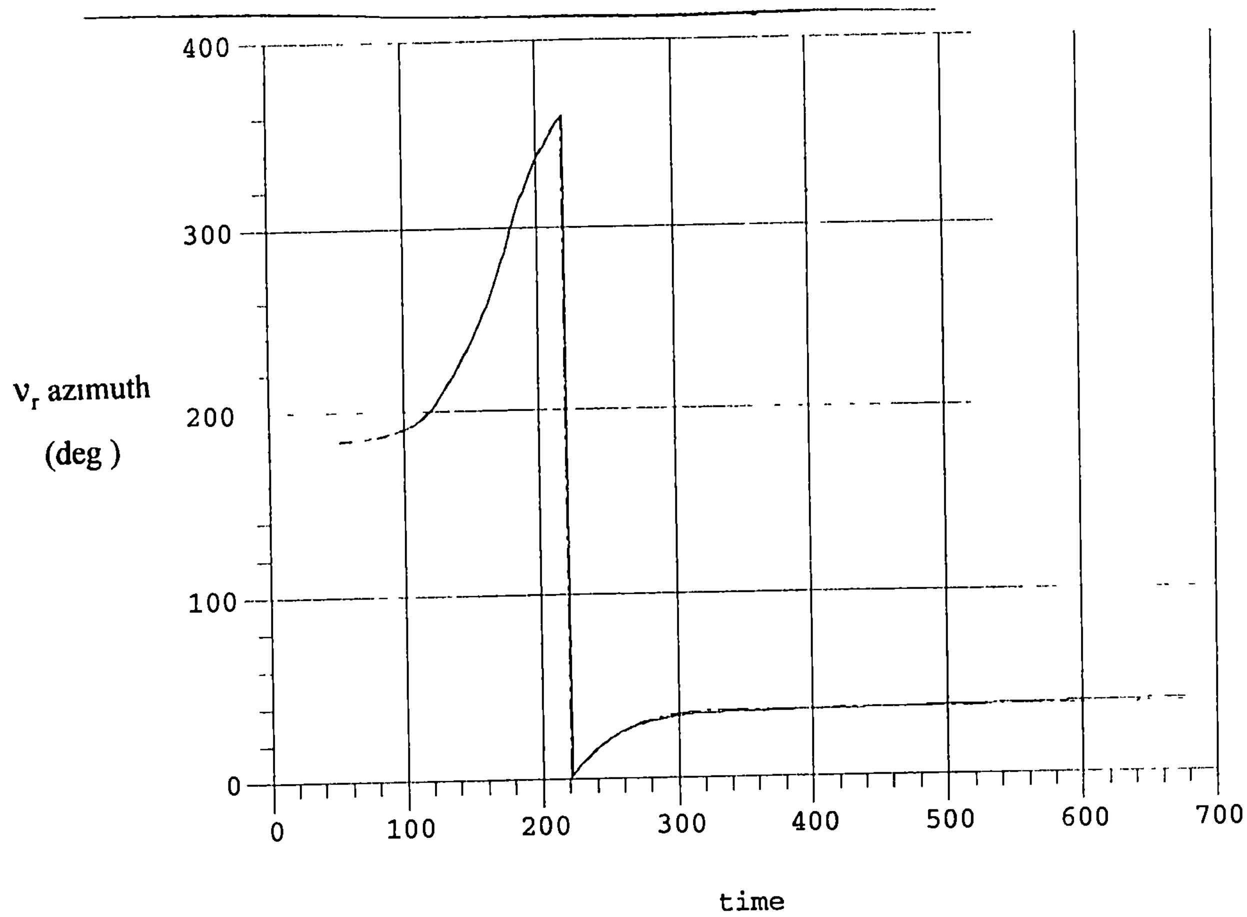

Figure 4 63 . Inverted separation relative velocity azimuth as a function of time

VITA

Brett Starr was born in Greensboro, North Carolina on January 30, 1961 He attended schools in the public school system of Guilford County, North Carolina, where he graduated from Southeast Guilford High School in June, 1979. He entered North Carolina State University at Raleigh in August of 1979 In May of 1984, he received a Bachelor of Science degree in Mechanical Engineering. He worked in industry with Volvo-GM Heavy Truck Corporation in Greensboro, North Carolina until January of 1997 when becoming a full-time student in the Master's Program at the University of Tennessee Space Institute with a NASA Space Grant While at the University of Tennessee Space Institute he completed double Master's degrees in Engineering Science and Aerospace Engineering